The Astrophysical Journal, 946:48 (32pp), 2023 March 20 https://doi.org/10.3847/1538-4357/acb93b
© 2023. The Author(s). Published by the American Astronomical Society.
OPEN ACCESS

Finding *r*-II Sibling Stars in the Milky Way with the Greedy Optimistic Clustering Algorithm

Kohei Hattori[1,2,3], Akifumi Okuno[2,4], and Ian U. Roederer[3,5]
[1] National Astronomical Observatory of Japan, 2-21-1 Osawa, Mitaka, Tokyo 181-8588, Japan
[2] The Institute of Statistical Mathematics, 10-3 Midoricho, Tachikawa, Tokyo 190-8562, Japan
[3] Department of Astronomy, University of Michigan, 1085 S. University Avenue, Ann Arbor, MI 48109, USA
[4] RIKEN Center for Advanced Intelligence Project, 1-4-1 Nihonbashi, Chuo-ku, Tokyo, 103-0027, Japan
[5] Joint Institute for Nuclear Astrophysics–Center for the Evolution of the Elements (JINA-CEE), 640 S. Shaw Lane, East Lansing, MI 48824 USA
Received 2022 July 8; revised 2023 February 3; accepted 2023 February 3; published 2023 March 28

Abstract

R-process enhanced stars with [Eu/Fe] $\geqslant +0.7$ (so-called *r*-II stars) are believed to have formed in an extremely neutron-rich environment in which a rare astrophysical event (e.g., a neutron-star merger) occurred. This scenario is supported by the existence of an ultra-faint dwarf galaxy, Reticulum II, where most of the stars are highly enhanced in *r*-process elements. In this scenario, some small fraction of dwarf galaxies around the Milky Way were *r* enhanced. When each r-enhanced dwarf galaxy accreted to the Milky Way, it deposited many *r*-II stars in the Galactic halo with similar orbital actions. To search for the remnants of the *r*-enhanced systems, we analyzed the distribution of the orbital actions of $N = 161$ *r*-II stars in the solar neighborhood by using Gaia EDR3 data. Since the observational uncertainty is not negligible, we applied a newly developed greedy optimistic clustering method to the orbital actions of our sample stars. We found six clusters of *r*-II stars that have similar orbits and chemistry, one of which is a new discovery. Given the apparent phase-mixed orbits of the member stars, we interpret that these clusters are good candidates for remnants of completely disrupted *r*-enhanced dwarf galaxies that merged with the ancient Milky Way.

Unified Astronomy Thesaurus concepts: Milky Way dynamics (1051); Galactic archaeology (2178); Milky Way stellar halo (1060); Astroinformatics (78); R-process (1324); Clustering (1908); Stellar dynamics (1596)

Supporting material: machine-readable tables

1. Introduction

1.1. Reconstructing the Galactic Merger History

In the standard paradigm of galaxy formation, it is believed that the stellar halo of the Milky Way was formed through numerous mergers with smaller stellar systems, such as dwarf galaxies (White & Rees 1978; Blumenthal et al. 1984). Identifying and recovering the past merger events in the Milky Way from the stellar position $\boldsymbol{x}$, velocity $\boldsymbol{v}$, chemistry, and age is one of the ultimate goals in Galactic astronomy.

Except for the surviving dwarf galaxies that are currently moving around the Milky Way at large Galactocentric radii, most of the dwarf galaxies that merged with the Milky Way are tidally disrupted. On the one hand, recently accreted dwarf galaxies are being disrupted to form stellar streams. These stellar streams have a spatially coherent structure, and they are extensively searched for by large photometric and astrometric surveys (Belokurov et al. 2006; Malhan et al. 2018; Shipp et al. 2018; Ibata et al. 2021; Martin et al. 2022). To date, nearly 100 stellar streams have been found (Mateu 2023), and many of these streams are thought to be associated with large merger events (Bonaca et al. 2021; Malhan et al. 2022). On the other hand, dwarf galaxies that merged with the ancient Milky Way have been completely disrupted (Bullock & Johnston 2005; Brauer et al. 2022; Wu et al. 2022). The stars that originated in these disrupted dwarf galaxies show a spatially smooth distribution due to the phase mixing of the orbits. The lack of spatial coherence makes it hard to identify the remnants of the disrupted dwarf galaxies. To unravel the ancient merger history of the Milky Way, it is crucial to find the remnants of the completely disrupted dwarf galaxies from the *field* halo stars.

Because the stars stripped from the progenitor dwarf galaxy move on orbits that are similar to the progenitor's orbit, the remnants of the disrupted dwarf galaxies show a clumped distribution in the phase space spanned by the conserved orbital properties, such as the orbital action $\boldsymbol{J}(\boldsymbol{x}, \boldsymbol{v}) = (J_r, J_\phi, J_z)$, angular momentum $\boldsymbol{L} = \boldsymbol{x} \times \boldsymbol{v}$, or orbital energy E (Helmi et al. 1999; Gómez et al. 2010). Thus, the most promising way to find these remnants is to find substructure in the dynamical phase space by using clustering methods (Myeong et al. 2018, 2019; Roederer et al. 2018a; Koppelman et al. 2019; Li et al. 2019; Matsuno et al. 2019; Yuan et al. 2020; Brauer et al. 2022; Buder et al. 2022; Shank et al. 2022; Lövdal et al. 2022).

1.2. r-II Stars as Tracers of Ancient Merger History

Spectroscopic observations of old stars in the Milky Way have revealed that a few percent of nearby field halo stars are highly enhanced in *r*-process elements, such as europium (Eu, $Z = 63$) (Beers & Christlieb 2005). Currently, more than 160 stars are known to have [Eu/Fe] $> +0.7$ (and [Eu/Ba] > 0) and are classified as *r*-II stars (Holmbeck et al. 2020). Their extremely enhanced Eu abundances and their old ages imply that each *r*-II star was born in a system that was polluted by Eu-rich ejecta from one *r*-process event, such as a neutron-star merger (Hotokezaka et al. 2015).

The birthplace of the field *r*-II stars has been a mystery for decades. Recently, Ji et al. (2016) and Roederer et al. (2016) discovered that the ultra-faint dwarf galaxy (UFD), Reticulum II, contains seven *r*-II stars among nine spectroscopically observed

Original content from this work may be used under the terms of the Creative Commons Attribution 4.0 licence. Any further distribution of this work must maintain attribution to the author(s) and the title of the work, journal citation and DOI.

stars in this galaxy. The discovery of this *r*-enhanced UFD favors a scenario wherein the majority of *r*-II stars in the halo were originally born in UFDs similar to Reticulum II, in which very rare *r*-process events, such as a neutron-star merger, occurred (Tsujimoto & Shigeyama 2014a, 2014b). In this scenario, *r*-II stars were later deposited to the Galactic halo when the progenitor system was disrupted (Brauer et al. 2022).

This view is supported by the distribution of the orbital action $\boldsymbol{J}$ of field *r*-II stars. Roederer et al. (2018a) performed a clustering analysis for $N = 35$ *r*-II stars in the solar neighborhood and found several clusters of stars with similar $\boldsymbol{J}$. Although metallicity information was not used in the clustering analysis, the discovered clusters turned out to have a tight distribution in [Fe/H]. These clusters of stars have similar orbits and chemistry, and at least some of the clusters may be the remnants of dwarf galaxies that were completely disrupted long ago.

1.3. Structure of This Paper

One of the limitations in previous studies of the clustering analysis of halo stars is that the clustering of stars in the orbital action $\boldsymbol{J}(\boldsymbol{x}, \boldsymbol{v})$ is blurred when the observational uncertainty in $(\boldsymbol{x}, \boldsymbol{v})$ is not negligible. For example, a modest distance uncertainty of $\Delta d/d = 0.2$ of solar-neighbor halo stars would result in an uncertainty in the action of $\Delta J \sim 400\,\mathrm{kpc\,km\,s^{-1}}$. This blurring effect is a serious problem when we aim to find dynamically cold substructure of halo stars. Indeed, the remnants of disrupted low-mass dwarf galaxies (with stellar mass $M_* < 10^6\,M_\odot$)—including UFDs—are expected to have a small internal dispersion of $\sigma_J \sim 100\,\mathrm{kpc\,km\,s^{-1}}$ in galaxy formation simulations (e.g., Bullock & Johnston 2005). Therefore, if we are to use conventional clustering methods to find dynamically cold substructure, we need to use a sample of halo stars with very good distance estimates. In fact, Roederer et al. (2018a) discarded 58% of the stars from their original catalog of *r*-II stars because their stellar distances were associated with more than 12.5% uncertainty. In general, the requirement of using very accurate data implies that we need to discard a large fraction of data available, which reduces the scientific impact of surveys. Therefore, it is crucial to invent a new clustering algorithm that allows data sets with large uncertainty.

The originality of this paper is the introduction of a new method, the *greedy optimistic clustering* method, designed to be used for finding clusters from noisy data sets. This method simultaneously estimates both the centroid of each cluster and the denoised (*true*) value for each data point. A general mathematical formulation of this method is described in the accompanying paper (Okuno & Hattori 2022). As demonstrated in Okuno & Hattori (2022), this new technique can successfully find the remnants of the completely disrupted dwarf galaxies from the realistic kinematical data of field halo stars with a Gaia EDR3-like astrometric error. In this paper, we apply one flavor of the greedy optimistic clustering method, a greedy optimistic clustering method using the Gaussian mixture model (GMM) (or greedy optimistic GMM), to $N = 161$ *r*-II halo stars to find the remnants of completely disrupted dwarf galaxies. This sample is an extended version of the *r*-II star catalog presented in Roederer et al. (2018a), including most of the *r*-II stars published before the end of 2020. We emphasize that, with our new technique, we do not need to discard the sample stars even if the distance uncertainty is large.

In this paper, we begin by describing our catalog of *r*-II stars in Section 2. In Section 3, we explain that some of our sample stars have a large uncertainty in $\boldsymbol{J}$ because of the observational uncertainty. This is why we use the greedy optimistic clustering method instead of the conventional clustering methods. In Section 4, we explain the concept of the *uncertainty set* and describe how we generate it. This procedure is a preprocessing of the data that is required for our clustering method. The detailed implementation of our method is presented in Section 5. (An intuitive illustration of our method is presented in Appendix A.) Section 6 describes how we perform the clustering analysis and presents the fiducial results. We find that the results in Roederer et al. (2018a) are recovered in our analysis. In Section 7, we discuss the implications of our results. In particular, we validate our clustering results by using the chemistry data in Section 7.1. We find six clusters with a tight distribution in chemical abundances that played no role in the clustering process or the initial selection for inclusion in our sample, which we interpret as revealing the remnants of completely disrupted dwarf galaxies (Section 7.2.1). We further analyze the connection of our results to the Galactic merger history (Sections 7.3 and 7.4). In Section 8, we summarize our paper.

2. Observational Data

We extend the sample in Roederer et al. (2018a) and construct a catalog of *r*-II stars for which reliable measurements of chemical abundances and the line-of-sight velocity $v_{\rm los}$ are available from high-resolution spectra. In constructing the catalog, we select $N = 161$ stars from the literature (published before the end of 2020) that satisfy the following criteria:[6]

1. [Eu/Fe] $\geqslant +0.7$ and [Eu/Ba]>0;
2. small $v_{\rm los}$ variability (no hint of binarity); and
3. not being a member of known dwarf galaxies or globular clusters.

When observational uncertainties overlap with the boundaries defined by criterion (i), we apply our best judgment to assess inclusion in the catalog, based on spectral quality, other heavy-element abundance ratios, and—when available—confirmation by independent studies. The distribution of [Fe/H] and [Eu/Fe] of our sample stars is shown in Figure 1. We combine the literature data on ([Fe/H], [Eu/Fe], [Eu/H], $v_{\rm los}$) and the astrometric data from Gaia EDR3 (Gaia Collaboration et al. 2021) to construct the catalog analyzed in this paper.

For those stars reported in Roederer et al. (2018a), we adopt the uncertainty $\sigma_{\rm vlos}$ in the line-of-sight velocity as in Roederer et al. (2018a). For the rest of the stars, we use either the literature value or assign some reasonable value. In any case, the value of $\sigma_{\rm vlos}$ is small for all of our sample stars and thus the detailed value of $\sigma_{\rm vlos}$ does not affect our results.

For all of these stars, Gaia EDR3 provides reliable measurements of the five-dimensional astrometric quantities, $(\alpha, \delta, \varpi, \mu_{\alpha*}, \mu_\delta)$, as well as their associated uncertainties. In this paper, $\widehat{X}$ and σ_X denote the point estimate and the one-dimensional uncertainty for the quantity X, respectively. We assume that the uncertainties associated with the R.A. and decl. (α, δ) are negligible, and thus we assume $(\alpha, \delta) = (\widehat{\alpha}, \widehat{\delta})$. For

[6] Our criteria on [Eu/Fe] is stricter than that used in Gudin et al. (2021) ([Eu/Fe]$> +0.3$) because the formation sites of mildly *r*-enhanced stars (so-called *r*-I stars) may not be UFDs (Wanajo et al. 2021; Hirai et al. 2022).

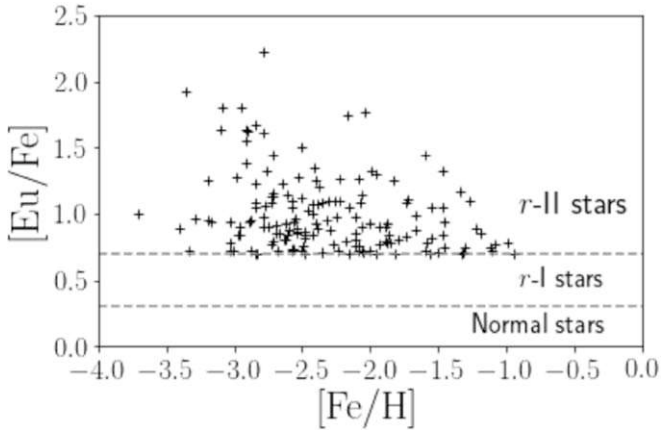

Figure 1. The chemistry of our sample of $N = 161$ stars is with [Eu/Fe] $\geqslant +0.7$, which we classify as *r*-II stars. Our sample is an extended version of the *r*-II star sample in Roederer et al. (2018a).

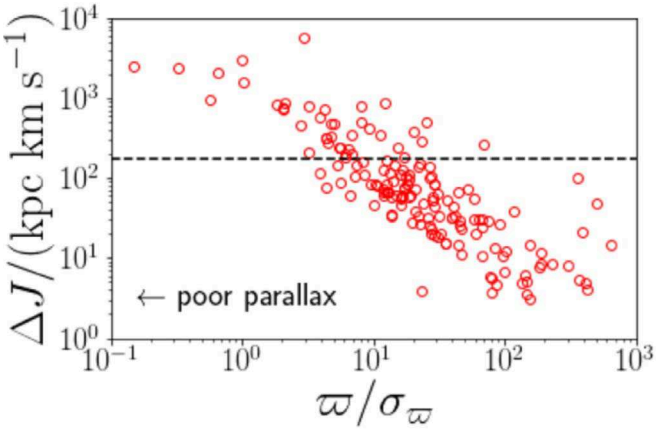

Figure 2. Observed uncertainty in parallax measured by ϖ/σ_ϖ and the resultant uncertainty in action ΔJ for our sample stars. We can see that stars with $\varpi/\sigma_\varpi \lesssim 10$ result in $\Delta J > \sqrt{3}\ \sigma_J$ (horizontal dashed line), where we set $\sigma_J = 100$ kpc km s^{-1}. Those stars with $\Delta J > \sqrt{3}\ \sigma_J$ cannot be adequately handled with a conventional GMM comprising K Gaussian distributions with internal dispersion σ_J. To handle this noisy data set, we created the greedy optimistic clustering method.

the parallax, we have the (zero-point corrected[7]) point estimate $\widehat{\varpi}$ and its uncertainty σ_ϖ. For the proper motion, we have the point estimate $(\widehat{\mu_{\alpha*}}, \widehat{\mu_\delta})$, their one-dimensional uncertainties $(\sigma_{\mu\alpha*}, \sigma_{\mu\delta})$, and the Pearson's correlation coefficient in these uncertainties $\rho_{\rm corr}$.

The names of the *r*-II stars and their chemical abundances are listed in Appendix D. We note that our catalog based on Gaia EDR3 supersedes the catalog in Roederer et al. (2018a), which is based on Gaia DR2 (Gaia Collaboration et al. 2016, 2018).

3. Why the Greedy Optimistic Clustering is Needed

Before we perform a clustering analysis, we explain the difficulty of using the conventional clustering methods for our data set. We note that this section is independent of the main analysis of this paper.

Let us compute the uncertainty in the orbital action given the error distribution of the observables in Section 2. For each star in our *r*-II star catalog, we randomly draw $(\alpha, \delta, \varpi, \mu_{\alpha*}, \mu_\delta, v_{\rm los})$ from the associated error distribution. After drawing a large enough number of instances (realizations), we discard instances with negative parallax and select 200 instances with $\varpi > 0$. By converting these observed quantities,[8] we obtain 200 instances of the orbital action, $\boldsymbol{J} = (J_r, J_z, J_\phi)$. For each star, we denote the standard deviation in each dimension as $(\Delta J_r, \Delta J_z, \Delta J_\phi)$. The uncertainty in the orbital action for each star is given by $\Delta J = \sqrt{(\Delta J_r)^2 + (\Delta J_z)^2 + (\Delta J_\phi)^2}$.

The uncertainty ΔJ is dominated by the uncertainty in parallax (or equivalently, distance). This is because the parallax uncertainty propagates to both the three-dimensional position and the two-dimensional tangential velocity. Figure 2 shows ΔJ as a function of the signal-to-noise ratio of the parallax, ϖ/σ_ϖ. On average, ΔJ increases if the parallax measurement becomes poorer. This trend partially justifies previous studies in which sample stars are selected based on a threshold of ϖ/σ_ϖ (Roederer et al. 2018a). However, using such a threshold means that we end up discarding some fraction of the original data, which is not desired.

As we will describe in Section 5, in this paper, we want to find clusters that typically have an intrinsic dispersion of $\sigma_J \sim 100$ kpc km s^{-1} in each dimension in $\boldsymbol{J}$ space. Thus, if a star's orbital action is associated with an uncertainty of $\Delta J \gtrsim \sqrt{3} \times 100$ kpc km s^{-1}, conventional clustering methods may fail to assign the star to the correct cluster. In this regard, about a quarter of our sample have $\Delta J \gtrsim \sqrt{3} \times 100$ kpc km s^{-1} (see Figure 2) and therefore they are not suited for conventional clustering analyses.

4. Preprocessing of the Data: Generation of the Uncertainty Set

An important difference between this paper and that of Roederer et al. (2018a) is that we use the greedy optimistic clustering method, which allows a clustering analysis of noisy data (Okuno & Hattori 2022). This method requires special preprocessing of the data. Namely, for each star, we generate M synthetic data points that represent the uncertainty in the data. We call these synthetic data points the *uncertainty set*.[9,10]

In this section, we describe how we generate the uncertainty set. In Section 4.1, we describe the uncertainty set of the observed quantities, $D_i^{\rm obs}$, for the ith star in the catalog. In Section 4.2, we convert $D_i^{\rm obs}$ to obtain the uncertainty set of the orbital action of the ith star, $D_i^{\rm action}$. We note that $D_i^{\rm action}$ will be used in our analysis.

4.1. Uncertainty Set of the Observed Quantities

As mentioned in Section 2, the six-dimensional observables for the ith star $(\alpha, \delta, \varpi, \mu_{\alpha*}, \mu_\delta, v_{\rm los})_i$ are associated with observational uncertainties. To represent these uncertainties, we generate

[7] We corrected for the zero-point offset in the parallax by using the prescription in Lindegren et al. (2021).

[8] The detailed procedure to compute the orbital action is the same as that described in Section 4.

[9] In Okuno & Hattori (2022), we used the term *empirical uncertainty set*, but we omit *empirical* for brevity in this paper.

[10] The uncertainty set is not restricted to a Monte Carlo realization of the error distribution. An uncertainty set typically aims to approximate a confidence region, but not approximate the distribution itself. For example, in the main analysis of this paper, the parallax in the uncertainty set is drawn uniformly from a user-specified region.

$M = 101$ six-dimensional observable vectors, which we call the uncertainty set. To be specific, the uncertainty set of the observed quantities of the ith star is expressed as

$$D_i^{\rm obs} = \{(\alpha,\ \delta,\ \varpi,\ \mu_{\alpha*},\ \mu_\delta,\ v_{\rm los})_{i,j} | -50 \leqslant j \leqslant 50\}. \quad (1)$$

In the following, we describe the procedure to generate the jth instance of the uncertainty set of the ith star, $(\alpha,\ \delta,\ \varpi,\ \mu_{\alpha*},\ \mu_\delta,\ v_{\rm los})_{i,j}$.

First, we set the $j = 0$th instance of the uncertainty set to be the same as the point estimate of the observables

$$(\alpha,\ \delta,\ \varpi,\ \mu_{\alpha*},\ \mu_\delta,\ v_{\rm los})_{i,0} = (\widehat{\alpha},\ \widehat{\delta},\ \widehat{\varpi},\ \widehat{\mu_{\alpha*}},\ \widehat{\mu_\delta},\ \widehat{v_{\rm los}})_i. \quad (2)$$

Second, for $j \neq 0$, we neglect the tiny observational errors in the sky position $(\alpha,\ \delta)$, and we set

$$\alpha_{i,j} = \widehat{\alpha}_i, \quad (3)$$

$$\delta_{i,j} = \widehat{\delta}_i. \quad (4)$$

Third, for $j \neq 0$, we draw the line-of-sight velocity and proper motion from the corresponding error distribution:

$$v_{{\rm los},i,j} \sim \mathcal{N}(\widehat{v_{\rm los}}_{,i};\ \sigma^2_{{\rm vlos},i}), \quad (5)$$

$$\begin{bmatrix} \mu_{\alpha*} \\ \mu_\delta \end{bmatrix}_{i,j} \sim \mathcal{N}\left(\begin{bmatrix} \widehat{\mu_{\alpha*}} \\ \widehat{\mu_\delta} \end{bmatrix}_i ; \begin{bmatrix} \sigma^2_{\mu\alpha*}, & \rho_{\rm corr}\sigma_{\mu\alpha*}\sigma_{\mu\delta} \\ \rho_{\rm corr}\sigma_{\mu\alpha*}\sigma_{\mu\delta}, & \sigma^2_{\mu\delta} \end{bmatrix}_i \right). \quad (6)$$

Here, $A \sim B$ indicates that A is drawn from a distribution B, and $\mathcal{N}(\boldsymbol{m};\ S)$ corresponds to a Gaussian distribution with mean $\boldsymbol{m}$ and covariance matrix S.

Lastly, for $j \neq 0$, we draw the parallax from a uniform distribution within a range of 2 standard deviations, $\widehat{\varpi}_i - 2\sigma_{\varpi,i} \leqslant \varpi_{i,j} \leqslant \widehat{\varpi}_i + 2\sigma_{\varpi,i}$. For computational simplicity, the parallax of the jth instance of $D_i^{\rm obs}$ is determined as

$$\varpi_{i,j} = \widehat{\varpi}_i + \sigma_{\varpi,i} \times \frac{j}{25}. \quad (7)$$

With this setting, the parallaxes of the $j = -50$th, 0th, and 50th instances of $D_i^{\rm obs}$ is $\widehat{\varpi}_i - 2\sigma_{\varpi,i}$, $\widehat{\varpi}_i$, and $\widehat{\varpi}_i + 2\sigma_{\varpi,i}$, respectively.[11,12]

Up to this step, we have generated the uncertainty set $D_i^{\rm obs}$ without taking care of their physical meanings. For example, if the parallax uncertainty $\sigma_{\varpi,i}$ is large for star i, the uncertainty set for this star may include an instance with negative parallax. To properly handle negative parallax (which is unphysical) and to compensate for the effect of observational uncertainty, we introduce a penalty function[13,14]

$$\text{penalty}(i,\ j,\ \lambda) = \begin{cases} \frac{1}{2}\lambda\left(\frac{j}{25}\right)^2 & (\text{if } \varpi_{i,j} > 0) \\ 10^{10}(1+\lambda) & (\text{if } \varpi_{i,j} \leqslant 0). \end{cases} \quad (8)$$

The hyperparameter $\lambda \geqslant 0$ is designed to tune the strength of the penalty (see also Equation (14)). In the fiducial analysis of this paper, we set $\lambda = 0$, and therefore the detailed implementation of the penalty function is not important in our fiducial analysis.

We repeat the same procedure for all j and generate the uncertainty set $D_i^{\rm obs}$ consisting of $M = 101$ instances of observable vectors. Then, we repeat the same procedure for all the stars, $i = 1, \cdots, N$.

4.2. Uncertainty Set of the Orbital Action

To perform a clustering analysis in the orbital action space, we need the uncertainty set of the orbital action. Here, we describe the procedure to map $D_i^{\rm obs}$ (Equation (1)) to the uncertainty set of the orbital action of the ith star

$$D_i^{\rm action} = \{\boldsymbol{J}_{i,j} | -50 \leqslant j \leqslant 50\}. \quad (9)$$

For each (i,j), we first convert the observables $(\alpha,\ \delta,\ \varpi,\ \mu_{\alpha*},\ \mu_\delta,\ v_{\rm los})_{i,j}$ into the position and velocity $(\boldsymbol{x},\ \boldsymbol{v})_{i,j}$ in the Galactocentric Cartesian coordinate. In this step, we assume the position and velocity of the Sun as described in Hattori et al. (2021). Then we map $(\boldsymbol{x},\ \boldsymbol{v})_{i,j}$ to the orbital action $\boldsymbol{J}_{i,j} = \boldsymbol{J}(\boldsymbol{x}_{i,j},\ \boldsymbol{v}_{i,j}) = (J_r,\ J_\phi,\ J_z)_{i,j}$. In computing the orbital action, we assume the gravitational potential of the Milky Way as in McMillan (2017) and we use the AGAMA package (Vasiliev 2019).

In the top row in Figure 3, the gray dots show the distribution of $D_i^{\rm action}$ for our entire sample. We can see that the uncertainty set for each star typically shows a banana-like shape, reflecting the fact that the parallax uncertainty dominates the uncertainty in $\boldsymbol{J}$.

5. Greedy Optimistic GMM

5.1. GMM in Action Space

In this paper, we assume that the GMM describes the intrinsic distribution of $\boldsymbol{J}$, which consists of K isotropic Gaussian distributions with an identical one-dimensional dispersion of σ_J^2. Under this assumption,[15] the probability distribution of a randomly chosen star is expressed as

$$P(\boldsymbol{J}|\theta) = \sum_{k=1}^{K} \pi_k \mathcal{N}(\boldsymbol{J}|\langle\boldsymbol{J}\rangle_k,\ \sigma_J^2\boldsymbol{I}). \quad (10)$$

Here, $\boldsymbol{I}$ denotes the identity matrix, $k = 1, \cdots, K$ is the index for the normal distributions representing clusters, with the model parameters $\theta = \{(\pi_k,\ \langle\boldsymbol{J}\rangle_k)|k = 1,\cdots,K;\ \pi_k \geqslant 0;\ \sum_{k=1}^{K}\pi_k = 1\}$ to be estimated. In the GMM clustering shown below, $\langle\boldsymbol{J}\rangle_k \equiv (\langle J_r\rangle_k,\ \langle J_\phi\rangle_k,\ \langle J_z\rangle_k)$ corresponds to the centroid of the kth cluster.

5.2. Conventional GMM

Let us first consider a case where we use the point estimate of action $\widehat{\boldsymbol{J}}_i$ for each star i to perform a clustering analysis. This case corresponds to an ideal case where we have no observational uncertainties.

In this case, the logarithmic likelihood of the data $D = \{\widehat{\boldsymbol{J}}_i | i = 1,\cdots,N\}$ given the model parameters $\theta = \{(\pi_k,$

[11] In generating the instances of the parallax, we do not use a Gaussian distribution. We note that using a Gaussian distribution (truncated within the range of 2 standard deviations) would not change the result significantly, as long as the instances of the parallax are densely distributed (e.g., $M \gtrsim 100$).

[12] We neglect the covariance between the proper motion and parallax. We have confirmed that the inclusion of the covariance hardly affects our results.

[13] Suppose that a star has $\varpi_{i,j} > 0$ for all j. Then, the penalty is 0 if $j = 0$ (if $\varpi_{i,j} = \widehat{\varpi}_i$). Also, the penalty is 2λif $j = \pm 50$ ($\varpi_{i,j} = \widehat{\varpi}_i \pm 2\sigma_{\varpi,i}$).

[14] Among $N = 161$ stars in our sample, there is no star whose observed parallax is negative, and there are only seven stars with `parallax_over_error` <2. This means that only seven stars satisfy ($\varpi - 2\sigma_\varpi < 0$). Thus, the treatment of rejecting negative parallax is relevant for these seven stars only.

[15] We discuss the implication of this assumption in Section 7.6.2.

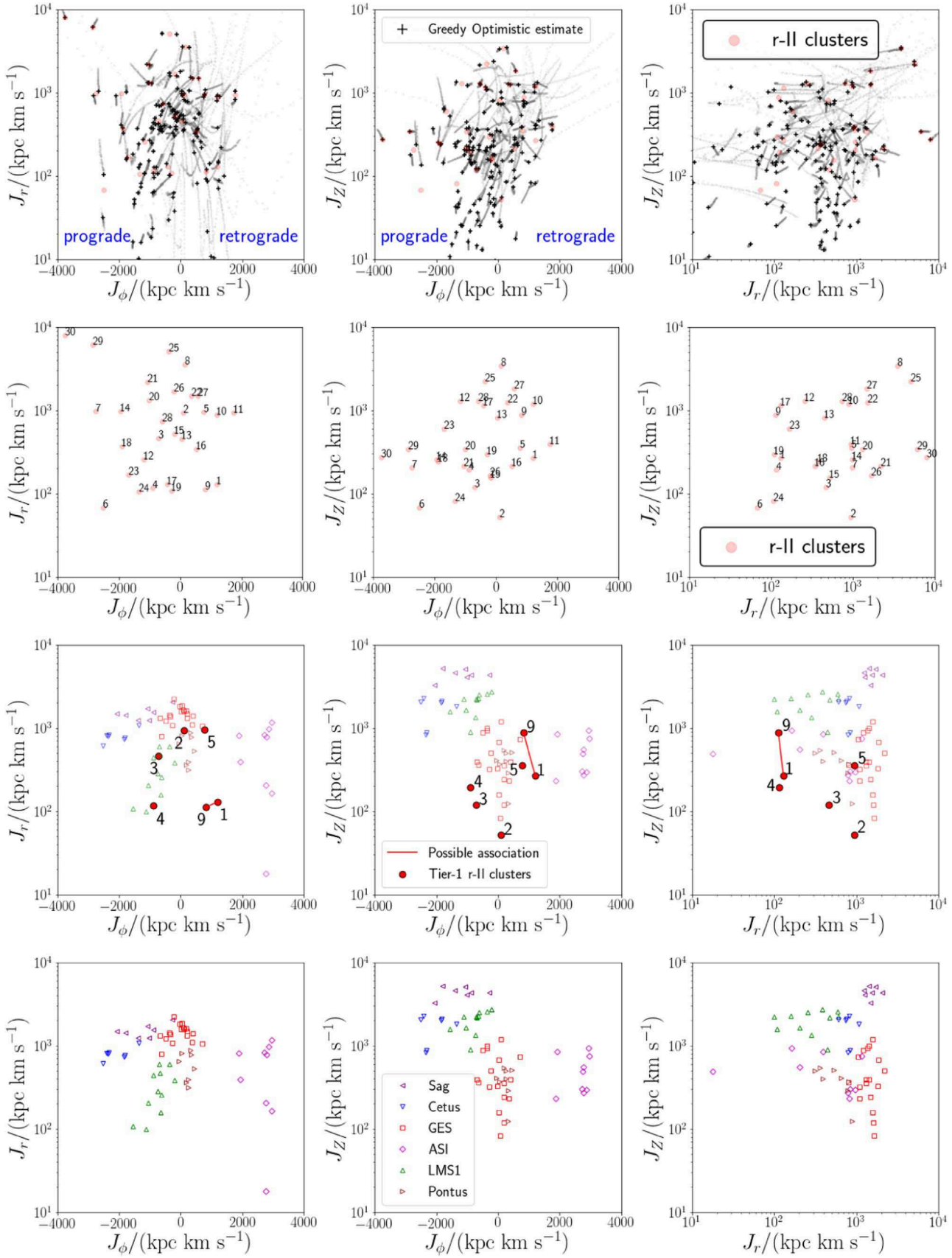

Figure 3. (Top row) Distribution of $N = 161$ *r*-II stars in the orbital action space. The gray dots represent the uncertainty set, which typically has a banana-like shape. The black cross represents the greedy optimistic estimate of the orbital action in our fiducial analysis. (Second row) Distribution of our *r*-II clusters in our fiducial analysis. The number indicates *k* of the *r*-II cluster H22:DTC-*k* ($1 \leqslant k \leqslant 30$). (Third row) Distribution of Tier 1 clusters (i.e., most confident clusters). Two *r*-II clusters H22:DTC-1 and nine are possibly associated (see Section 7.4). (Bottom row) Orbital actions of the stellar streams and globular clusters associated with the six merger groups (the data are based on Malhan et al. 2022 and Vasiliev & Baumgardt 2021).

$\langle \boldsymbol{J} \rangle_k) | k = 1, \cdots, K\}$ is given by

$$\ln L(D|\theta) = \sum_{i=1}^{N} \ln \left\{ \sum_{k=1}^{K} \pi_k \mathcal{N}(\widehat{\boldsymbol{J}}_i | \langle \boldsymbol{J} \rangle_k, \sigma_J^2 \boldsymbol{I}) \right\}. \tag{11}$$

The expectation-maximization (EM) algorithm tries to find the best parameters by iteratively improving them with the following steps (Dempster et al. 1977; Neal & Hinton 1998; Bishop 2006):

1. (E step) For a given set of $(\{\pi_k, \langle \boldsymbol{J} \rangle_k | k = 1, \cdots, K)$, compute γ_{ik} and N_k given by

$$\begin{cases} \gamma_{ik} = \dfrac{\pi_k \mathcal{N}(\widehat{\boldsymbol{J}}_i | \langle \boldsymbol{J} \rangle_k, \sigma_J^2 \boldsymbol{I})}{\sum_{\ell=1}^{K} \pi_\ell \mathcal{N}(\widehat{\boldsymbol{J}}_i | \langle \boldsymbol{J} \rangle_\ell, \sigma_J^2 \boldsymbol{I})} \\ N_k = \sum_{i=1}^{N} \gamma_{ik}. \end{cases} \tag{12}$$

2. (M step) Update $(\{\pi_k, \langle \boldsymbol{J} \rangle_k | k = 1, \cdots, K)$ with the following expressions:

$$\begin{aligned} \langle \boldsymbol{J} \rangle_k &\leftarrow \frac{1}{N_k} \sum_{i=1}^{N} \gamma_{ik} \widehat{\boldsymbol{J}}_i, \\ \pi_k &\leftarrow \frac{N_k}{N}. \end{aligned} \tag{13}$$

We note that γ_{ik} is called responsibility, which quantifies the contribution of the ith star to the kth cluster. The quantity N_k represents the effective size of the kth cluster. The EM algorithm iteratively updates γ_{ik} and the parameters such that the likelihood function is monotonically improved until convergence.

5.3. Greedy Optimistic GMM

The abovementioned conventional GMM does not take into account the uncertainty in the data. Therefore, the conventional GMM does not work when $\boldsymbol{J}$ is associated with large uncertainties. This is why we introduce a new flavor of clustering method, the greedy optimistic clustering method (Okuno & Hattori 2022). An intuitive illustration of this method is given in Appendix A.

The key ideas of our method are as follows:

1. We make an *optimistic* assumption that the true orbital actions of N stars $\{\boldsymbol{J}_i^{\rm true} | i = 1, \cdots, N\}$ are highly clustered in the $\boldsymbol{J}$ space.
2. Given the uncertainty set $D_i^{\rm action}$ consisting of M instances of the orbital action of the ith star $\{\boldsymbol{J}_{i,j}\}$, we assume that one of the instances $\boldsymbol{J}_{i,\beta_i}$ is *very close* to the true orbital action $\boldsymbol{J}_i^{\rm true}$. Here, β_i is the index of the *best* instance (among M instances) in the uncertainty set $D_i^{\rm action}$.
3. Given the two assumptions above, we *greedily* find the best configuration $\{\boldsymbol{J}_{i,\beta_i} | i = 1, \cdots, N\}$ of N stars such that their distribution is most highly clustered in the $\boldsymbol{J}$ space. We call the best instance $\boldsymbol{J}_{i,\beta_i}$ the *greedy optimistic estimate* of the orbital action for star i.

In the greedy optimistic clustering algorithm, we simultaneously estimate the cluster parameters $\{(\pi_k, \langle \boldsymbol{J} \rangle_k) | k = 1, \cdots, K\}$ as well as the best indices $\{\beta_i | i = 1, \cdots, N\}$ such that the clustering of N points $\{\boldsymbol{J}_{i,\beta_i} | i = 1, \cdots, N\}$ is most enhanced. For this purpose, we define an object function to be maximized

$$f(D^{\rm action}|\theta) = \sum_{i=1}^{N} \ln \left\{ \sum_{k=1}^{K} \pi_k \mathcal{N}(\boldsymbol{J}_{i,\beta_i} | \langle \boldsymbol{J} \rangle_k, \sigma_J^2 \boldsymbol{I}) \right\} - \sum_{i=1}^{N} \text{penalty}(i, \beta_i, \lambda). \tag{14}$$

Here, $\lambda \geqslant 0$ is a hyperparameter that controls the strength of the penalty term. Also,

$$D^{\rm action} = \{D_i^{\rm action} | i = 1, \cdots, N\} \tag{15}$$

is the uncertainty set of the entire sample, and

$$\theta = \{\{(\pi_k, \langle \boldsymbol{J} \rangle_k) | k = 1, \cdots, K\}, \{\beta_i | i = 1, \cdots, N\}\} \tag{16}$$

are the model parameters. We note that the model parameters now include $\{\beta_i\}$.

To find the solution, we use an iteration algorithm, which we refer to as the GOEM algorithm. In the GOEM algorithm, we introduce a "GO step" (greedy optimistic step) in addition to the E and M steps:

1. (GO step) For a given set of $\{(\pi_k, \langle \boldsymbol{J} \rangle_k) | k = 1, \cdots, K\}$, update $\{\beta_i | i = 1, \cdots, N\}$ so that the object function $f(D^{\rm action}|\theta)$ is maximized.
2. (E step) For a given set of $\{(\pi_k, \langle \boldsymbol{J} \rangle_k) | k = 1, \cdots, K\}$ and $\{\beta_i | i = 1, \cdots, N\}$, compute γ_{ik} and N_k given by

$$\begin{cases} \gamma_{ik} = \dfrac{\pi_k \mathcal{N}(\boldsymbol{J}_{i,\beta_i} | \langle \boldsymbol{J} \rangle_k, \sigma_J^2 \boldsymbol{I})}{\sum_{\ell=1}^{K} \pi_\ell \mathcal{N}(\boldsymbol{J}_{i,\beta_i} | \langle \boldsymbol{J} \rangle_\ell, \sigma_J^2 \boldsymbol{I})} \\ N_k = \sum_{i=1}^{N} \gamma_{ik}. \end{cases} \tag{17}$$

3. (M step) Update $\{(\pi_k, \langle \boldsymbol{J} \rangle_k) | k = 1, \cdots, K\}$ with the following expressions:

$$\begin{cases} \langle \boldsymbol{J} \rangle_k \leftarrow \dfrac{1}{N_k} \sum_{i=1}^{N} \gamma_{ik} \boldsymbol{J}_{i,\beta_i}, \\ \pi_k \leftarrow \dfrac{N_k}{N}. \end{cases} \tag{18}$$

We note that, in the GO step, we can optimize β_i separately for each i.

The GO, E, and M steps always improve the object function $f(D^{\rm action}|\theta)$. Just like the conventional EM algorithm, the GOEM algorithm converges to a local maximum, and there is no guarantee that the derived solution is the global maximum. To find a better solution, we try many initial conditions of the parameters and use the split-and-merge algorithm (Ueda et al. 1998).

5.4. Difference between the Conventional GMM and the Greedy Optimistic GMM

In the greedy optimistic GMM, for each star i, we have the freedom to choose an instance from the uncertainty set $D_i^{\rm action}$. In a sense, we can *move* the locations of the data points according to their uncertainties and can search for the best

configuration such that the N data points are most highly clustered. This characteristic is in contrast to the conventional GMM, where the data point is stuck at its point estimate. Note that the greedy optimistic GMM is distinct from extreme deconvolution (Bovy et al. 2011), which further assumes that the centroid $\langle \boldsymbol{J} \rangle_k$ of the kth cluster also follows a distribution, i.e., cluster center has uncertainty.

In the greedy optimistic GMM method, we introduce a penalty term in the object function (second term in Equation (14)). This penalty term is designed to favor the instances whose parallax is closer to the point estimate of the parallax. The strength of the penalty term is governed by the hyperparameter λ. On the one hand, in the limiting case of $\lambda \to \infty$, the optimal solution satisfies $\beta_i = \mathrm{argmin}_\beta\{\mathrm{penalty}(i, \beta, \lambda)\}$. In this limit, the greedy optimistic GMM reduces to the conventional GMM because we no longer have the freedom to choose among M instances. Thus, the greedy optimistic GMM is a generalization of the conventional GMM. On the other hand, in the limiting case of $\lambda = 0$, the greedy optimistic GMM treats all the instances equally. Interestingly, the mock data analysis in Okuno & Hattori (2022) suggests that the performance of the clustering is reasonably good when we set $\lambda = 0$. Indeed, we adopt $\lambda = 0$ in the fiducial analysis in this paper.

6. Analysis and Results

After preparing for the uncertainty set $\{D_i^{\mathrm{action}}\}$, we perform a greedy optimistic clustering analysis for our sample stars.

6.1. List of Hyperparameters

In the greedy optimistic GMM, we need to fix three hyperparameters (σ_J, λ, K), which will be described in the following.

6.1.1. Internal Dispersion of the Cluster: σ_J

The hyperparameter σ_J determines the internal dispersion of a cluster in $\boldsymbol{J}$ space. In realistic galaxy formation simulations, completely disrupted low-mass stellar systems typically have a dispersion of $\sim$(100–200) kpc km s^{-1} in $\boldsymbol{J}$ space (Bullock & Johnston 2005). Motivated by this result, we fix

$$\sigma_J = 100\ \mathrm{kpc\ km\ s^{-1}}. \tag{19}$$

This value of σ_J is also supported by the observed properties of UFDs hosting r-II stars, such as Reticulum II, which has an internal velocity dispersion of $\sigma_v \sim 3$ km s^{-1} (Koposov et al. 2015; Walker et al. 2015; Minor et al. 2019). If a stellar system with a similar velocity dispersion is disrupted in the inner part of the Milky Way ($r_{\mathrm{disruption}} \sim$ 10–30 kpc), we expect that the stars stripped from the system typically have a spread in the action of $\sigma_v \times r_{\mathrm{disruption}} \sim$ (30–90) kpc km s^{-1}.

In principle, we can make σ_J a free parameter to be fitted in the analysis. However, we fix σ_J to stabilize our analysis, following the mock data analysis in Okuno & Hattori (2022).

6.1.2. Number of Clusters: K

The number of clusters K is hard to choose, because fixing K is equivalent to fixing the typical size of a cluster, N/K, which is unknown. After some experiments, we adopt six values, $K = 10$, 20, 30, 40, 50, and 60.

6.1.3. Strength of the Penalty Term: λ

The hyperparameter λ governs the penalty term in our greedy optimistic GMM method. To see how our result is affected by λ, we adopt six values, $\lambda = 0$, 10^{-4}, 10^{-3}, 10^{-2}, 1, and 10^2. On the one hand, $\lambda = 0$ corresponds to the most optimistic case where we pay the least attention to the observed parallax. On the other hand, the case with $\lambda = 10^2$ is almost equivalent to the conventional GMM.

6.2. Fiducial Hyperparameters

As mentioned above, we try 36 sets of hyperparameters (K, λ) while fixing σ_J =100 kpc km s^{-1}. Among 36 combinations, we choose the fiducial set of hyperparameters to be (K, λ, σ_J) = (30, 0, and 100 kpc km s^{-1}) with the following procedure.

First, for each set of (K, λ), we find the best solution $\{(\pi_k, \langle \boldsymbol{J} \rangle_k) | k = 1, \cdots, K\}$ and $\{\beta_i | i = 1, \cdots, N\}$ that maximizes the object function (Equation (14)). Here, we use 400 initial conditions to efficiently explore the parameter space; and use the split-and-merge method (Ueda et al. 1998) to avoid local optimums.

After finding the best solution, we assign each star to the nearest centroid. Namely, the ith star is assigned to the c_ith cluster such that

$$c_i = \mathrm{argmin}_k ||\boldsymbol{J}_{i,\beta_i} - \langle \boldsymbol{J} \rangle_k||. \tag{20}$$

We count the number of member stars $N_{\mathrm{member},k}$ for the kth cluster.[16] We note that this stringent assignment sometimes results in clusters with no members assigned, especially when $\lambda \leqslant 10^{-2}$ and $K \geqslant 50$. This is one of the reasons why we do not explore $K > 60$ in our analysis.

If the kth cluster has $N_{\mathrm{member},k} \geqslant 2$ members, we compute the internal dispersion in (J_r, J_z, J_ϕ):

$$(\sigma_{Jr,k})^2 = \frac{1}{N_{\mathrm{member},k}} \sum_{i \in k\mathrm{thcluster}} ||(\boldsymbol{J}_{i,\beta_i} - \langle \boldsymbol{J} \rangle_k)_r||^2, \tag{21}$$

$$(\sigma_{Jz,k})^2 = \frac{1}{N_{\mathrm{member},k}} \sum_{i \in k\mathrm{thcluster}} ||(\boldsymbol{J}_{i,\beta_i} - \langle \boldsymbol{J} \rangle_k)_z||^2, \tag{22}$$

$$(\sigma_{J\phi,k})^2 = \frac{1}{N_{\mathrm{member},k}} \sum_{i \in k\mathrm{thcluster}} ||(\boldsymbol{J}_{i,\beta_i} - \langle \boldsymbol{J} \rangle_k)_\phi||^2, \tag{23}$$

and the total internal dispersion is

$$\sigma_k = \sqrt{\frac{1}{3}[(\sigma_{Jr,k})^2 + (\sigma_{Jz,k})^2 + (\sigma_{J\phi,k})^2]}. \tag{24}$$

Here, $(\boldsymbol{J}_{i,\beta_i} - \langle \boldsymbol{J} \rangle_k)_q$ corresponds to the q component of the vector $(\boldsymbol{J}_{i,\beta_i} - \langle \boldsymbol{J} \rangle_k)$, where $q = r$, z, ϕ.

For each set of hyperparameters (K, λ), we compute the median of $\{\sigma_k\}$ for clusters with $N_{\mathrm{member},k} \geqslant 2$. When λ is fixed, the median value of $\{\sigma_k\}$ is a decreasing function of K, so we choose the optimal K such that this median is closest to σ_J (= 100 kpc km s^{-1}), which is the fixed hyperparameter. As a result, we found that $K = 30$ is optimal for $\lambda \leqslant 1$, while $K = 50$ is optimal for $\lambda = 10^2$. This result indicates that we need $K = 30$ clusters to represent the action distribution for our $N = 161$ stars if we adopt the greedy optimistic clustering,

[16] We note that $N_{\mathrm{member},k} \simeq N_k (= \pi_k N)$. $N_{\mathrm{member},k}$ is an integer resulting from the stringent assignment, while N_k is a real number resulting from a lenient assignment.

almost independent of the strength of the penalty term (unless the penalty term is too strong). Thus, we choose $K = 30$ as the fiducial value. With $K = 30$, we have the freedom to choose $0 \leqslant \lambda \leqslant 1$. For simplicity, we choose $\lambda = 0$ as the fiducial value, motivated by the mock analysis in Okuno & Hattori (2022).

6.3. Fiducial Result

Here, we focus on the result obtained for the fiducial set of hyperparameters, (K, λ, and σ_J) = (30, 0, and 100 kpc km s^{-1}). We refer to the clusters of r-II stars in our fiducial result as r-II clusters. Also, following recent convention (Yuan et al. 2020; Gudin et al. 2021), we label the kth r-II cluster as H22:DTC-k, where DTC stands for dynamically tagged cluster.[17]

Since we are most interested in the orbital properties of the r-II stars and r-II clusters, we visualize their distribution in the $\boldsymbol{J}$ space. The top row in Figure 3 shows the distribution of the greedy optimistic estimate $\boldsymbol{J}_{i,\beta_i}$ (black cross) for $N = 161$ r-II stars, along with their uncertainty set $D_i^{\rm action}$ (gray dots).[18] The second row in Figure 3 shows the distribution of centroids of the orbital action, $\langle \boldsymbol{J} \rangle_k$, for $K = 30$ clusters.

Table 1 summarizes the properties of r-II clusters, including the cluster size $N_{{\rm member},k}$, orbital action of the centroid $\langle \boldsymbol{J} \rangle_k$, the total internal dispersion of the orbital action σ_k, and the chemical properties. As seen in Table 1, σ_k is approximately 100 kpc km s^{-1}, which is a natural consequence of the way we choose our hyperparameter K. We note that the chemical information is not used in our clustering analysis, but will be used to validate our clustering results (see Section 7.1).

Tables 2 and 3 present the detailed chemical and dynamical information of individual r-II stars analyzed in this paper. Due to their length, we put them in Appendix D.

Table 2 lists the chemical and kinematical properties of the member stars for each cluster. For an easy comparison of the results in Roederer et al. (2018a) with ours, we add column R18 in Table 2, which indicates those stars that are included in groups A–H in Roederer et al. (2018a). We will comment on this comparison in Section 6.4. Table 2 also lists the reference for the chemical data. The orbital action listed in Table 2 is the greedy optimistic estimate $\boldsymbol{J}_{i,\beta_i}$ (shown in the top row of Figure 3). For reference, we also list the orbital energy E, which is computed as $E = \boldsymbol{v}_{i,\beta_i}^2/2 + \Phi(\boldsymbol{x}_{i,\beta_i})$, where Φ is the Milky Way's gravitational potential (McMillan 2017). Unlike Roederer et al. (2018a), we do not use E in our clustering, because E is a function of the orbital action and therefore it provides duplicated information. The last column in Table 2 is the quantity `parallax_over_error` ($=\varpi/\sigma_\varpi$) taken from Gaia EDR3 (and not corrected for the zero-point offset of the parallax). We list this information here to make it easier to understand which member stars benefit from the greedy optimistic clustering. For example, a star with poor parallax measurements ($\varpi/\sigma_\varpi \lesssim 10$) may not be assigned to the right cluster with conventional clustering methods, while a star with good parallax measurements ($\varpi/\sigma_\varpi \gtrsim 10$) is likely assigned to the right cluster independent of the clustering methods. (See Appendix F where we analyze $N = 119$ r-II stars with $\varpi/\sigma_\varpi > 10$ by using standard GMM.)

Table 3 lists additional information on the member stars in each cluster. All of the quantities in this table are not used in the clustering analysis, but they are presented to offer an intuitive understanding of the dynamical properties of stars. The Galactocentric position and velocity listed in this table correspond to ($\boldsymbol{x}_{i,\beta_i}$, $\boldsymbol{v}_{i,\beta_i}$), respectively. By using the position–velocity pair, we integrate the orbit for 100 Gyr to obtain the pericentric radius ($r_{\rm peri}$), apocentric radius ($r_{\rm apo}$), maximum distance from the Galactic disk plane ($z_{\rm max}$), and orbital eccentricity $ecc = (r_{\rm apo} - r_{\rm peri})/(r_{\rm apo} + r_{\rm peri})$. Because the member stars of a given cluster have similar orbital actions, they also have similar values of ($r_{\rm peri}$, $r_{\rm apo}$, $z_{\rm max}$, ecc). In contrast, the member stars of a given cluster have very different ($\boldsymbol{x}_{i,\beta_i}$, $\boldsymbol{v}_{i,\beta_i}$). This result is consistent with a scenario wherein the progenitor system of a cluster accreted to the Milky Way long ago, and the stars stripped from the progenitor system are completely phase mixed today.

6.4. Consistency with Roederer et al. (2018a)

Because we extend the analysis in Roederer et al. (2018a), we briefly check the consistency between their results and ours. As summarized in Table 1, all the stars in groups A, D, E, G, and H in Roederer et al. (2018a) are found in clusters H22:DTC-3, 2, 15, 5, and 15, respectively. Also, the majority of the members in groups B (3 stars out of 4 stars), C (3 out of 4), and F (2 out of 3) are found in H22:DTC-9, 4, and 3, respectively. These results are reassuring in that Roederer et al. (2018a) and this work apply different clustering methods to data sets with different quality and still mostly agree with each other.

Intriguingly, groups A and F are included in a single cluster H22:DTC-3 in our analysis; and groups E and H (and another star from group F) are included in a single cluster H22:DTC-15. In our analysis, the clusters H22:DTC-3 and 15 are the biggest clusters, containing $N_{{\rm member},k} = 18$ stars each. Our result may reflect either of two possibilities. The first possibility is that our new clustering method is superior to conventional methods. (Namely, our method can find a cluster that is seen as multiple clusters with conventional methods due to the observational uncertainty.) The second possibility is that our method is too optimistic. (Namely, multiple clusters with slightly different orbital properties are mistakenly regarded as a single one due to the optimistic nature of our method.) Although we have not arrived at a decisive conclusion as to which of these possibilities is correct, it is worth mentioning that the cluster H22:DTC-3 is one of the six clusters in our analysis for which we have the highest confidence based on the tight distribution in [Fe/H] and [Eu/H] (see Section 7.2.1). According to our additional analysis using high-quality data alone (see Appendix F), 10 stars among 18 stars in H22:DTC-3 are more likely to be associated with each other than the remaining eight stars.

Also, the cluster H22:DTC-15 would have a tight distribution in [Fe/H] and [Eu/H] if we remove one metal-rich outlier star (see Appendix C.3).

7. Discussion

7.1. Chemical Homogeneity of the Clusters

Up to this point, we only use the orbital action of the r-II stars, and we do not use the chemical properties of these stars. (The chemical information is used to construct the sample, but the chemical information is not used for the clustering analysis.) Because our clustering analysis is based on a few assumptions,

[17] We use dynamically tagged *clusters* rather than dynamically tagged *groups*, in order to not to be confused with the merger groups.

[18] For some stars, the greedy optimistic estimate is located near the edge of the uncertainty set. We point out that this phenomenon is not problematic in our clustering analysis, as described in Appendix E.

Table 1
Properties of the Clusters

Cluster Name (H22:DTC-k)	$N_{\mathrm{member},k}$	(J_r, J_z, J_ϕ) kpc km s^{-1}	$(\sigma_{Jr}, \sigma_{Jz}, \sigma_{J\phi})$ kpc km s^{-1}	σ_k kpc km s^{-1}	$\langle$[Fe/H]$\rangle$ dex	$\sigma_{\mathrm{[Fe/H]}}$ ($q_{\mathrm{[Fe/H]}}$) dex (percentile)	$\langle$[Eu/H]$\rangle$ dex	$\sigma_{\mathrm{[Eu/H]}}$ ($q_{\mathrm{[Eu/H]}}$) dex (percentile)	Comment[(a)]
H22:DTC-1	9	(129, 265, 1209)	(107, 140, 112)	121	−2.78	0.22 (0.56)	−1.64	0.32 (5.06)	Tier 1: new
H22:DTC-2	9	(942, 52, 102)	(113, 49, 104)	93	−1.65	0.25 (1.08)	−0.62	0.22 (0.78)	Tier 1: $D^{3/3}$ (R18)
H22:DTC-3	18	(464, 118, −711)	(123, 113, 117)	118	−2.37	0.37 (1.86)	−1.45	0.35 (1.20)	Tier 1: $A^{4/4}$,$F^{2/3}$ (R18), DTG38 (Y20)
H22:DTC-4	12	(115, 195, −889)	(63, 56, 67)	63	−2.42	0.33 (2.76)	−1.48	0.33 (2.78)	Tier 1: $C^{3/4}$ (R18)
H22:DTC-5	5	(954, 354, 773)	(70, 114, 15)	78	−2.62	0.21 (4.92)	−1.60	0.20 (4.30)	Tier 1: $G^{2/2}$ (R18)
H22:DTC-6	2	(67, 67, −2504)	(35, 65, 7)	43	−2.55	0.05 (10.11)	−1.36	0.36 (63.38)	Tier 3: new
H22:DTC-7	2	(971, 206, −2749)	(57, 30, 86)	62	−2.83	0.05 (10.83)	−1.82	0.11 (21.37)	Tier 2: new
H22:DTC-8	2	(3519, 3390, 163)	(8, 71, 110)	76	−1.66	0.06 (11.65)	−0.39	0.23 (43.04)	Tier 3: new
H22:DTC-9	6	(112, 873, 829)	(60, 193, 79)	125	−2.87	0.31 (12.58)	−1.65	0.33 (13.92)	Tier 1: $B^{3/4}$ (R18), DTG10 (Y20)
H22:DTC-10	4	(878, 1190, 1208)	(51, 110, 39)	73	−2.27	0.26 (15.28)	−1.34	0.26 (16.82)	Tier 2: new
H22:DTC-11	2	(936, 388, 1757)	(101, 32, 0)	61	−1.39	0.08 (17.42)	−0.58	0.03 (7.01)	Tier 2: new
H22:DTC-12	2	(256, 1282, −1180)	(13, 54, 180)	108	−2.48	0.09 (18.15)	−1.40	0.07 (14.35)	Tier 2: new
H22:DTC-13	6	(450, 807, 47)	(77, 103, 106)	96	−2.51	0.35 (18.28)	−1.43	0.26 (6.44)	Tier 2: new
H22:DTC-14	2	(969, 254, −1940)	(47, 111, 167)	119	−2.90	0.11 (22.26)	−1.43	0.86 (97.43)	Tier 3: new
H22:DTC-15	18	(518, 153, −177)	(105, 109, 105)	106	−2.43	0.50 (30.62)	−1.51	0.49 (30.46)	Tier 4: $E^{3/3}$,$F^{1/3}$,$H^{2/2}$ (R18), DTG38 (Y20)
H22:DTC-16	13	(340, 214, 521)	(131, 120, 64)	109	−2.21	0.50 (34.18)	−1.25	0.54 (52.98)	$B^{1/4}$ (R18)
H22:DTC-17	4	(129, 1145, −419)	(153, 65, 88)	108	−1.94	0.42 (43.80)	−0.60	0.39 (38.32)	Tier 4: new
H22:DTC-18	3	(370, 243, −1889)	(32, 4, 38)	29	−2.64	0.41 (51.06)	−1.42	0.41 (51.54)	…
H22:DTC-19	7	(107, 292, −287)	(88, 130, 86)	103	−2.12	0.53 (54.58)	−1.11	0.56 (67.74)	…
H22:DTC-20	4	(1308, 342, −1017)	(18, 98, 49)	64	−2.20	0.49 (58.04)	−1.32	0.51 (63.82)	…
H22:DTC-21	2	(2163, 215, −1052)	(12, 11, 39)	24	−2.36	0.43 (70.65)	−1.17	0.01 (2.44)	Tier 3: new
H22:DTC-22	2	(1497, 1253, 363)	(11, 13, 38)	24	−2.78	0.55 (81.60)	−1.86	0.74 (93.86)	…
H22:DTC-23	3	(167, 595, −1688)	(9, 53, 95)	63	−2.48	0.66 (85.46)	−1.41	0.57 (78.02)	…
H22:DTC-24	14	(105, 80, −1344)	(97, 87, 116)	101	−2.04	0.68 (92.02)	−1.19	0.57 (64.82)	Tier 4: $C^{1/4}$ (R18)
H22:DTC-25	2	(5062, 2249, −367)	(10, 115, 233)	150	−1.90	0.72 (92.49)	−1.07	0.75 (93.99)	…
H22:DTC-26	4	(1668, 165, −210)	(99, 24, 146)	103	−1.85	0.83 (97.70)	−0.93	0.84 (97.96)	…
H22:DTC-27	1	(1485, 1831, 579)	(–, –, –)	⋯	−1.82	… (–)	−1.12	… (–)	…
H22:DTC-28	1	(727, 1284, −585)	(–, –, –)	⋯	−1.88	… (–)	−1.10	… (–)	…
H22:DTC-29	1	(6120, 342, −2857)	(–, –, –)	⋯	−3.71	… (–)	−2.71	… (–)	Most metal-poor
H22:DTC-30	1	(8014, 274, −3751)	(–, –, –)	⋯	−3.41	… (–)	−2.52	… (–)	Second-most metal-poor

Note. (a) R18 denotes Roederer et al. (2018a) and Y20 denotes Yuan et al. (2020). Group C in R18 contains four member stars, among which three stars are included in our cluster H22:DTC-4. This is why we put a comment "$C^{3/4}$ (R18)" for our cluster H22:DTC-4.

(This table is available in machine-readable form.)

Table 2
Basic Properties of the Member Stars of the Clusters

k	R18	Name	([Fe/H],[Eu/H], [Eu/Fe]) dex	Reference	(J_r, J_z, J_ϕ) kpc km s^{-1}	E 10^5 km^2 s^{-2}	ϖ/σ_ϖ
1		HE 1523-0901	(−2.95, −1.14, 1.81)	Frebel et al. (2007)	(148, 366, +1219)	−1.558	16.626
1		RAVE J203843.2-002333	(−2.91, −1.27, 1.64)	Placco et al. (2017)	(99, 269, +1400)	−1.559	11.179
1		2MASS J09544277+5246414	(−2.99, −1.71, 1.28)	Holmbeck et al. (2018)	(216, 462, +1319)	−1.482	26.830
1		2MASS J17225742-7123000	(−2.42, −1.35, 1.07)	Hansen et al. (2018)	(143, 396, +1212)	−1.553	18.841
1		2MASS J20050670-3057445	(−3.03, −2.09, 0.94)	Cain et al. (2018)	(378, 80, +1208)	−1.565	20.871
1		HE 1044-2509	(−2.89, −1.95, 0.94)	Barklem et al. (2005)	(87, 410, +1237)	−1.564	11.977
1		J14592981-3852558	(−2.40, −1.47, 0.93)	Holmbeck et al. (2020)	(10, 146, +993)	−1.790	13.810
1		BPS CS 22896-154	(−2.69, −1.83, 0.86)	François et al. (2007)	(10, 83, +1076)	−1.793	17.928
1		2MASS J01555066-6400155	(−2.71, −1.91, 0.80)	Ezzeddine et al. (2020)	(70, 171, +1218)	−1.662	17.600
2		SMSS J175046.30-425506.9	(−2.17, −0.42, 1.75)	Jacobson et al. (2015)	(966, 55, +117)	−1.606	2.798
2		HD 222925	(−1.47, −0.14, 1.33)	Roederer et al. (2018b)	(1052, 84, +273)	−1.520	189.056
2		RAVE J071142.5-343237	(−1.96, −0.66, 1.30)	Sakari et al. (2018a)	(774, 3, +228)	−1.709	43.802
2		2MASS J18024226-4404426	(−1.55, −0.50, 1.05)	Hansen et al. (2018)	(796, 150, +154)	−1.642	16.274
2		J11404944-1615396	(−1.67, −0.79, 0.88)	Holmbeck et al. (2020)	(925, 109, +57)	−1.620	16.332
2		J07352232-4425010	(−1.58, −0.79, 0.79)	Holmbeck et al. (2020)	(1041, 27, +46)	−1.604	184.629
2		HD 20	(−1.60, −0.87, 0.73)	Hanke et al. (2020)	(1115, 9, −99)	−1.572	92.637
2		2MASS J01530024-3417360	(−1.50, −0.79, 0.71)	Hansen et al. (2018)	(972, 5, +37)	−1.657	231.958
2		HD 3567	(−1.33, −0.63, 0.70)	Hansen et al. (2012)	(835, 24, +105)	−1.692	412.636
3		2MASS J00512646-1053170	(−2.38, −1.17, 1.21)	Ezzeddine et al. (2020)	(420, 219, −810)	−1.600	189.026
3		HE 0430-4901	(−2.72, −1.56, 1.16)	Barklem et al. (2005)	(427, 121, −719)	−1.669	27.471
3		2MASS J22562536-0719562	(−2.26, −1.16, 1.10)	Sakari et al. (2018a)	(371, 121, −636)	−1.726	11.873
3		SDSS J173025.57+414334.7	(−2.85, −1.77, 1.08)	Bandyopadhyay et al. (2020)	(706, 45, −788)	−1.557	39.280
3		HE 2224+0143	(−2.58, −1.53, 1.05)	Barklem et al. (2005)	(338, 51, −592)	−1.805	16.152
3		J03422816-6500355	(−2.16, −1.11, 1.05)	Holmbeck et al. (2020)	(365, 14, −688)	−1.778	98.567
3		BPS CS 22958-052	(−2.42, −1.42, 1.00)	Roederer et al. (2014a)	(435, 21, −895)	−1.660	68.063
3		SDSS J004305.27+194859.20	(−2.25, −1.27, 0.98)	Bandyopadhyay et al. (2020)	(534, 36, −652)	−1.679	35.415
3		BPS CS 22875-029	(−2.69, −1.77, 0.92)	Roederer et al. (2014a)	(389, 352, −655)	−1.618	11.905
3		HD 115444	(−2.96, −2.11, 0.85)	Westin et al. (2000)	(601, 25, −603)	−1.667	67.006
3		J01425445-0904162	(−1.73, −0.90, 0.83)	Holmbeck et al. (2020)	(372, 37, −891)	−1.684	47.161
3		G206-23	(−1.79, −0.98, 0.81)	Ishigaki et al. (2013)	(688, 361, −695)	−1.476	305.366
3		HD 221170	(−2.18, −1.38, 0.80)	Ivans et al. (2006)	(379, 16, −962)	−1.669	79.320
3		HE 0420+0123a	(−3.03, −2.24, 0.79)	Hollek et al. (2011)	(367, 232, −622)	−1.680	41.097
3		RAVE J015656.3-140211	(−2.08, −1.32, 0.76)	Sakari et al. (2018a)	(704, 203, −621)	−1.543	14.705
3		BPS CS 22877-015	(−2.00, −1.28, 0.72)	Roederer et al. (2014a)	(399, 12, −531)	−1.819	103.131
3		J12044314-2911051	(−2.35, −1.64, 0.71)	Holmbeck et al. (2020)	(489, 202, −829)	−1.574	31.947
3		2MASS J15271353-2336177	(−2.15, −1.45, 0.70)	Hansen et al. (2018)	(357, 28, −659)	−1.778	46.190
4		2MASS J21064294-6828266	(−2.76, −1.44, 1.32)	Hansen et al. (2018)	(62, 314, −901)	−1.716	40.082
4		J05383296-5904280	(−2.53, −1.25, 1.28)	Holmbeck et al. (2020)	(198, 257, −890)	−1.670	80.688
4		BPS CS 22945-017	(−2.73, −1.60, 1.13)	Roederer et al. (2014a)	(150, 200, −1029)	−1.673	35.846
4		2MASS J18174532-3353235	(−1.67, −0.68, 0.99)	Johnson et al. (2013)	(126, 146, −871)	−1.769	3.870
4		RAVE J133748.9-082617	(−2.62, −1.69, 0.93)	Sakari et al. (2018a)	(125, 281, −795)	−1.731	5.305
4		2MASS J15582962-1224344	(−2.54, −1.65, 0.89)	Hansen et al. (2018)	(18, 222, −951)	−1.763	22.353
4		2MASS J17163340-7009028	(−2.39, −1.50, 0.89)	Ezzeddine et al. (2020)	(23, 207, −919)	−1.780	10.026
4		BPS CS 30306-132	(−2.42, −1.57, 0.85)	Honda et al. (2004)	(244, 157, −926)	−1.678	21.118
4		J20435776-4408037	(−1.85, −1.07, 0.78)	Holmbeck et al. (2020)	(65, 138, −852)	−1.818	12.669
4		2MASS J21095804-0945400	(−2.73, 1.96, 0.77)	Hansen et al. (2018)	(95, 143, −864)	−1.792	9.632
4		2MASS J19215077-4452545	(−2.56, − 1.82, 0.74)	Hansen et al. (2018)	(106, 176, −887)	−1.758	4.410
4		2MASS J17435113-5359333	(−2.24, −1.51, 0.73)	Hansen et al. (2018)	(105, 144, −754)	−1.829	25.874
5		2MASS J02462013-1518419	(−2.71, −1.26, 1.45)	Hansen et al. (2018)	(1087, 281, +796)	−1.358	21.971
5		BPS CS 22953-003	(−2.84, −1.79, 1.05)	François et al. (2007)	(951, 388, +768)	−1.383	18.803
5		HE 2327-5642	(−2.78, −1.80, 0.98)	Mashonkina et al. (2010)	(877, 531, +749)	−1.380	12.640
5		SMSS J183647.89-274333.1	(−2.48, −1.66, 0.82)	Howes et al. (2015)	(927, 380, +773)	−1.390	3.254
5		HE 0300-0751	(−2.27, −1.50, 0.77)	Barklem et al. (2005)	(930, 190, +777)	−1.435	0.990
6		2MASS J05241392-0336543	(−2.50, −1.00, 1.50)	Ezzeddine et al. (2020)	(103, 133, −2497)	−1.352	4.395
6		2MASS J07150266-0154092	(−2.60, −1.72, 0.88)	Ezzeddine et al. (2020)	(31, 2, −2512)	−1.403	30.915
7		SMSS J062609.83-590503.2	(−2.77, −1.71, 1.06)	Jacobson et al. (2015)	(914, 176, −2835)	−1.133	13.632
7		HE 2244-1503	(−2.88, −1.93, 0.95)	Barklem et al. (2005)	(1029, 237, −2662)	−1.126	6.843
8		J07202253-3358518	(−1.60, −0.16, 1.44)	Holmbeck et al. (2020)	(3527, 3318, +52)	−0.813	69.734

Table 2
(Continued)

k	R18	Name	([Fe/H],[Eu/H], [Eu/Fe]) dex	Reference	(J_r, J_z, J_ϕ) kpc km s^{-1}	E 10^5 km^2 s^{-2}	ϖ/σ_ϖ
8		Gaia DR2 2233912206910720000	(−1.72, −0.61, 1.11)	Hawkins & Wyse (2018)	(3510, 3462, +274)	−0.796	25.346
9		SDSS J235718.91-005247.8	(−3.36, −1.44, 1.92)	Aoki et al. (2010)	(139, 755, +927)	−1.525	43.974
9		BPS CS 31082-001	(−2.90, − 1.27, 1.63),	Hill et al. (2002)	(85, 1019, +855)	−1.496	17.304
9		SDSS J092157.27+503404.7	(−2.65, − 1.42, 1.23),	Bandyopadhyay et al. (2020)	(118, 791, +834)	−1.549	27.046
9		SMSS J051008.62-372019.8	(−3.20, − 2.25, 0.95),	Jacobson et al. (2015)	(90, 695, +829)	−1.588	83.448
9		BPS CS 22888-047	(−2.54, − 1.68, 0.86),	Roederer et al. (2014a)	(21, 739, +862)	−1.595	4.769
9		SMSS J195931.70-643529.3	(−2.58, − 1.84, 0.74),	Jacobson et al. (2015)	(219, 1238, +665)	−1.444	8.568
10		HE 2301-4024	(−2.11, − 1.13, 0.98),	Barklem et al. (2005)	(794, 1019, +1181)	−1.249	2.984
10		BPS CS 29491-069	(−2.55, − 1.59, 0.96),	Hayek et al. (2009)	(889, 1314, +1276)	−1.180	22.426
10		2MASS J19324858-5908019	(−1.93, − 1.03, 0.90),	Hansen et al. (2018)	(895, 1252, +1184)	−1.196	4.210
10		HE 1131+0141	(−2.48, − 1.61, 0.87),	Barklem et al. (2005)	(934, 1175, +1188)	−1.199	2.078
11		G15-13	(−1.47, −0.62, 0.85)	Ishigaki et al. (2013)	(1038, 355, +1757)	−1.217	639.873
11		G115-58	(−1.30, −0.55, 0.75)	Ishigaki et al. (2013)	(835, 420, +1756)	−1.248	116.967
12		2MASS J22182082-3827554	(−2.57, −1.47, 1.10)	Ezzeddine et al. (2020)	(269, 1227, −1000)	−1.367	24.310
12		2MASS J03270229+0132322	(−2.39, −1.32, 1.07)	Ezzeddine et al. (2020)	(243, 1336, −1361)	−1.294	64.065
13		2MASS J14534137+0040467	(−3.09, −1.29, 1.80)	Ezzeddine et al. (2020)	(541, 791, −166)	−1.552	4.740
13		2MASS J13052137-1137220	(−2.07, −0.98, 1.09)	Ezzeddine et al. (2020)	(478, 719, +84)	−1.634	6.495
13		HE 1127-1143	(−2.73, −1.65, 1.08)	Barklem et al. (2005)	(363, 861, +110)	−1.642	1.829
13		SMSS J221448.33-453949.9	(−2.56, −1.62, 0.94)	Jacobson et al. (2015)	(344, 1012, +90)	−1.587	0.148
13		2MASS J12091322-1415313	(−2.11, −1.30, 0.81)	Sakari et al. (2018a)	(434, 727, +160)	−1.632	16.765
13		RAVE J192632.8-584657	(−2.49, −1.73, 0.76)	Rasmussen et al. (2020)	(538, 736, +5)	−1.614	5.545
14		2MASS J15213995-3538094	(−2.79, −0.56, 2.23)	Cain et al. (2020)	(922, 366, −2107)	−1.194	36.738
14		2MASS J01553180-4919420	(−3.01, −2.29, 0.72)	Ezzeddine et al. (2020)	(1016, 142, −1773)	−1.253	58.543
15		BPS CS 22892-052	(−3.10, −1.46, 1.64)	Sneden et al. (2003)	(679, 358, −335)	−1.576	6.801
15		2MASS J21091825-1310062	(−2.40, −1.15, 1.25)	Hansen et al. (2018)	(488, 136, −88)	−1.849	28.003
15		BPS CS 22945-058	(−2.71, −1.58, 1.13)	Roederer et al. (2014a)	(624, 72, −214)	−1.753	28.693
15		2MASS J14543792+0830379	(−2.31, −1.21, 1.10)	Ezzeddine et al. (2020)	(391, 176, −157)	−1.866	17.143
15		SMSS J181505.16-385514.9	(−3.29, −2.33, 0.96)	Howes et al. (2015)	(452, 53, −136)	−1.916	3.207
15		J00041581-5815524	(−2.32, −1.37, 0.95)	Holmbeck et al. (2020)	(529, 341, +74)	−1.729	14.929
15		2MASS J19014952-4844359	(−1.87, −0.94, 0.93)	Hansen et al. (2018)	(453, 43, −125)	−1.930	19.104
15		BD +17 3248	(−2.06, −1.15, 0.91)	Cowan et al. (2002)	(572, 45, −110)	−1.838	95.470
15		BPS CS 29529-054	(−2.75, −1.85, 0.90)	Roederer et al. (2014a)	(596, 59, −274)	−1.756	59.902
15		2MASS J00405260-5122491	(−2.11, −1.25, 0.86)	Hansen et al. (2018)	(582, 35, −166)	−1.817	423.879
15		G210-33	(−1.08, −0.31, 0.77)	Ishigaki et al. (2013)	(738, 200, −396)	−1.576	364.784
15		2MASS J19232518-5833410	(−2.08, −1.32, 0.76)	Hansen et al. (2018)	(558, 98, −186)	−1.788	29.542
15		J18050641-4907579	(−2.58, −1.85, 0.73)	Holmbeck et al. (2020)	(325, 48, −246)	−1.977	13.794
15		RAVE J000738.2-034551	(−2.09, −1.36, 0.73)	Sakari et al. (2018a)	(629, 95, −260)	−1.722	8.238
15		BPS BS 17569-049	(−2.88, −2.16, 0.72)	François et al. (2007)	(521, 345, −36)	−1.743	6.694
15		J23342332-2748003	(−2.35, −1.64, 0.71)	Holmbeck et al. (2020)	(481, 226, −151)	−1.775	13.352
15		2MASS J13494713-7423395	(−2.85, −2.15, 0.70)	Ezzeddine et al. (2020)	(363, 263, −146)	−1.845	28.769
15		SMSS J182601.24-332358.3	(−2.83, −2.13, 0.70)	Howes et al. (2016)	(496, 113, −218)	−1.806	7.387
16		HE 1219-0312	(−2.92, −1.54, 1.38)	Hayek et al. (2009)	(361, 292, +539)	−1.687	2.126
16		2MASS J20093393-3410273	(−1.99, −0.67, 1.32)	Hansen et al. (2018)	(258, 231, +641)	−1.735	8.035
16		2MASS J15383085-1804242	(−2.09, −0.82, 1.27)	Sakari et al. (2018b)	(321, 150, +454)	−1.806	66.989
16		J07103110-7121522	(−1.47, −0.42, 1.05)	Holmbeck et al. (2020)	(551, 17, +573)	−1.706	146.784
16		2MASS J15211026-0607566	(−2.00, −1.07, 0.93)	Sakari et al. (2018a)	(293, 270, +545)	−1.734	30.961
16		J20000364-3301351	(−1.89, −0.99, 0.90)	Holmbeck et al. (2020)	(189, 198, +445)	−1.880	14.214
16		RAVE J194550.6-392631	(−2.79, −1.89, 0.90)	Rasmussen et al. (2020)	(81, 116, +522)	−1.984	12.934
16		BPS BS 16543-097	(−2.48, −1.63, 0.85)	Allen et al. (2012)	(369, 93, +554)	−1.774	29.222
16		RAVE J093730.5-062655	(−1.86, −1.01, 0.85)	Sakari et al. (2019)	(565, 247, +608)	−1.586	18.012
16		BPS CS 22882-001	(−2.62, −1.81, 0.81)	Roederer et al. (2014a)	(487, 415, +462)	−1.605	3.864
16		RAVE J130524.5-393126	(−2.11, −1.35, 0.76)	Rasmussen et al. (2020)	(327, 72, +496)	−1.835	26.463
16		LP877-23	(−1.46, −0.71, 0.75)	Ishigaki et al. (2013)	(261, 438, +410)	−1.725	385.595
16		HE 1430+0053	(−3.03, −2.31, 0.72)	Barklem et al. (2005)	(356, 237, +530)	−1.719	16.215
17		Gaia DR2 6412626111276193920	(−2.04, −0.27, 1.77)	Ji et al. (2020)	(29, 1161, −393)	−1.598	0.658
17		2MASS J00101758-1735387	(−2.41, −1.06, 1.35)	Ezzeddine et al. (2020)	(0, 1245, −569)	−1.539	74.434

Table 2
(Continued)

k	R18	Name	([Fe/H],[Eu/H], [Eu/Fe]) dex	Reference	(J_r, J_z, J_ϕ) kpc km s^{-1}	E 10^5 km^2 s^{-2}	ϖ/σ_ϖ
17		2MASS J23362202-5607498	(−2.06, −0.92, 1.14)	Hansen et al. (2018)	(100, 1078, −369)	−1.601	10.327
17		LAMOST J112456.61+453531.1	(−1.27, −0.17, 1.10)	Xing et al. (2019)	(387, 1096, −344)	−1.494	5.019
18		2MASS J03073894-0502491	(−2.22, −0.95, 1.27)	Ezzeddine et al. (2020)	(376, 238, −1874)	−1.373	7.300
18		HE 0432-0923	(−3.19, −1.94, 1.25)	Barklem et al. (2005)	(328, 242, −1852)	−1.388	4.483
18		2MASS J02165716-7547064	(−2.50, −1.38, 1.12)	Hansen et al. (2018)	(407, 250, −1942)	−1.349	18.601
19		SMSS J183128.71-341018.4	(−1.83, −0.58, 1.25)	Howes et al. (2016)	(54, 216, −249)	−2.100	6.064
19		2MASS J19161821-5544454	(−2.35, −1.27, 1.08)	Hansen et al. (2018)	(101, 216, −345)	−1.988	10.641
19		SMSS J183225.29-334938.4	(−1.74, −0.66, 1.08)	Howes et al. (2016)	(183, 311, −262)	−1.898	1.034
19		SMSS J175738.37-454823.5	(−2.46, −1.44, 1.02)	Jacobson et al. (2015)	(38, 306, −198)	−2.079	5.578
19		2MASS J21224590-4641030	(−2.96, −2.06, 0.90)	Hansen et al. (2018)	(139, 579, −460)	−1.725	17.135
19		2MASS J18294359-4924253	(−1.22, −0.33, 0.89)	Ezzeddine et al. (2020)	(61, 151, −234)	−2.162	12.451
19		J20411424-4654315	(−2.30, −1.42, 0.88)	Holmbeck et al. (2020)	(302, 225, −204)	−1.880	11.797
20		SMSS J155430.57-263904.8	(−2.61, −1.47, 1.14)	Jacobson et al. (2015)	(1297, 444, −1027)	−1.245	6.169
20		2MASS J00524174-0902235	(−1.46, −0.52, 0.94)	Ezzeddine et al. (2020)	(1283, 379, −940)	−1.269	29.465
20		HE 0240-0807	(−2.68, −1.95, 0.73)	Barklem et al. (2005)	(1328, 367, −1020)	−1.260	0.323
20		RAVE J091858.9-231151	(−2.05, −1.34, 0.71)	Sakari et al. (2018a)	(1324, 179, −1080)	−1.273	15.284
21		2MASS J14325334-4125494	(−2.79, −1.18, 1.61)	Hansen et al. (2018)	(2151, 227, −1013)	−1.116	52.981
21		Gaia DR2 1508756353921427328	(−1.93, −1.16, 0.77)	Hawkins & Wyse (2018)	(2175, 204, −1091)	−1.114	23.097
22		2MASS J12170829+0415146	(−2.22, −1.12, 1.10)	Ezzeddine et al. (2020)	(1486, 1239, +401)	−1.188	0.577
22		BPS CS 30315-029	(−3.33, −2.61, 0.72)	Barklem et al. (2005)	(1509, 1267, +324)	−1.190	4.335
23		HE 1226-1149	(−2.91, −1.36, 1.55)	Cohen et al. (2013)	(156, 645, −1760)	−1.369	5.527
23		J22372037-4741375	(−2.97, −2.13, 0.84)	Holmbeck et al. (2020)	(180, 521, −1553)	−1.428	13.029
23		J10401894-4106124	(−1.55, − 0.73, 0.82)	Holmbeck et al. (2020)	(164, 619, −1751)	−1.374	42.487
24		BPS CS 29497-004	(−2.85, −1.18, 1.67)	Hill et al. (2017)	(365, 239, −1406)	−1.471	12.522
24		BPS CS 31078-018	(−2.84, −1.61, 1.23)	Lai et al. (2008)	(275, 25, −1215)	−1.634	44.957
24		J22190836-2333467	(−2.54, −1.67, 0.87)	Holmbeck et al. (2020)	(106, 108, −1167)	−1.690	22.914
24		BPS CS 22943-132	(−2.67, −1.81, 0.86)	Roederer et al. (2014a)	(62, 221, −1374)	−1.598	141.707
24		BPS CS 22886-012	(−2.61, −1.76, 0.85)	Roederer et al. (2014a)	(106, 25, −1165)	−1.738	19.888
24		J10191573-1924464	(−1.11, −0.36, 0.75)	Holmbeck et al. (2020)	(126, 42, −1368)	−1.646	23.505
24		J06195001-5312114	(−2.06, −1.33, 0.73)	Holmbeck et al. (2020)	(72, 258, −1299)	−1.602	149.166
24		J14354680-1124122	(−1.10, −0.38, 0.72)	Holmbeck et al. (2020)	(16, 10, −1556)	−1.656	76.502
24		RAVE J183623.2-642812	(−2.50, −1.78, 0.72)	Rasmussen et al. (2020)	(15, 41, −1294)	−1.730	27.378
24		HD 120559	(−1.31, − 0.60, 0.71)	Hansen et al. (2012)	(52, 15, −1493)	−1.656	136.429
24		2MASS J18295183-4503394	(−2.48, −1.78, 0.70)	Hansen et al. (2018)	(10, 20, −1358)	−1.722	46.753
24		BD-10 3742	(−1.96, −1.26, 0.70)	Hansen et al. (2020)	(81, 46, −1288)	−1.694	32.606
24		J06320130-2026538	(−1.56, −0.86, 0.70)	Holmbeck et al. (2020)	(137, 65, −1308)	−1.647	155.373
24		RAVE J115941.7-382043	(−0.94, −0.24, 0.70)	Rasmussen et al. (2020)	(46, 7, −1512)	−1.658	87.671
25		G166-37	(−1.18, −0.32, 0.86)	Ishigaki et al. (2013)	(5072, 2134, −601)	−0.735	357.603
25		HE 2252-4225	(−2.63, −1.82, 0.81)	Mashonkina et al. (2014)	(5051, 2365, −133)	−0.747	2.050
26		RAVE J040618.2-030525	(−1.34, −0.17, 1.17)	Rasmussen et al. (2020)	(1801, 130, −18)	−1.272	58.391
26		LAMOST J110901+075441	(−3.17, −2.23, 0.94)	Mardini et al. (2020)	(1727, 196, −366)	−1.289	9.180
26		Gaia DR2 3602288924850161792	(−1.89, −1.09, 0.80)	Valentini et al. (2019)	(1566, 158, −339)	−1.321	27.652
26		CD -45 3283	(−0.99, −0.21, 0.78)	Hansen et al. (2012)	(1577, 178, −119)	−1.321	153.969
27		Gaia DR2 4248140165233284352	(−1.82, −1.12, 0.70)	Hawkins & Wyse (2018)	(1485, 1831, +579)	−1.102	12.291
28		G14-39	(−1.88, −1.10, 0.78)	Ishigaki et al. (2013)	(727, 1284, −585)	−1.310	501.058
29		SMSS J024858.41-684306.4	(−3.71, −2.71, 1.00)	Jacobson et al. (2015)	(6120, 342, −2857)	−0.662	20.514
30		SMSS J063447.15-622355.0	(−3.41, −2.52, 0.89)	Jacobson et al. (2015)	(8014, 274, −3751)	−0.560	8.100

(This table is available in machine-readable form.)

Table 3
Kinematics of the Member Stars of the Clusters

k	Name	(x, y, z) kpc	(v_x, v_y, v_z) km s^{-1}	$(r_{\rm peri}, r_{\rm apo}, z_{\rm max})$ kpc	e
1	HE 1523-0901	(−6.03, −0.22, +1.70)	(−129.96, −206.98, −133.45)	(5.12, 10.74, 6.19)	0.35
1	RAVE J203843.2-002333	(−4.90, +3.34, −2.05)	(−49.37, −251.97, −99.46)	(5.71, 10.28, 4.99)	0.29
1	2MASS J09544277+5246414	(−9.88, +0.54, +2.03)	(−134.36, −126.27, −105.30)	(5.52, 12.92, 7.89)	0.40
1	2MASS J17225742-7123000	(−5.08, −2.49, −1.34)	(+136.70, −171.43, +197.75)	(5.23, 10.81, 6.46)	0.35
1	2MASS J20050670-3057445	(−5.50, +0.50, −1.45)	(−214.54, −200.21, −0.53)	(3.32, 12.03, 2.43)	0.57
1	HE 1044-2509	(−8.15, −3.15, +1.80)	(+130.57, −101.43, +118.74)	(5.71, 10.06, 6.12)	0.28
1	J14592981-3852558	(−4.28, −2.38, +1.46)	(+82.34, −186.23, +98.55)	(4.50, 5.86, 2.39)	0.13
1	BPS CS 22896-154	(−5.50, −0.95, −1.58)	(+41.00, −188.75, +35.32)	(4.59, 5.87, 1.71)	0.12
1	2MASS J01555066-6400155	(−7.20, −2.45, −3.32)	(+39.59, −155.61, +7.25)	(4.82, 8.32, 3.35)	0.27
2	SMSS J175046.30-425506.9	(−2.23, −1.21, −0.84)	(+346.38, +135.11, +98.60)	(0.24, 12.48, 5.30)	0.96
2	HD 222925	(−7.99, −0.18, −0.34)	(−242.31, −39.80, +67.35)	(0.55, 14.65, 5.34)	0.93
2	RAVE J071142.5-343237	(−8.97, −1.78, −0.36)	(−101.63, −45.73, −9.88)	(0.49, 10.25, 4.42)	0.91
2	2MASS J18024226-4404426	(−4.64, −0.72, −0.65)	(−277.88, −76.27, + 100.64)	(0.36, 11.28, 5.24)	0.94
2	J11404944-1615396	(−7.86, −1.91, +1.85)	(−185.77, −52.35, −15.18)	(0.29, 11.76, 5.27)	0.95
2	J07352232-4425010	(−8.28, −0.47, −0.08)	(+204.29, +5.85, +51.49)	(0.18, 12.53, 5.47)	0.97
2	HD 20	(−8.10, +0.04, −0.47)	(−229.00, +13.53, +6.35)	(0.22, 13.33, 5.55)	0.97
2	2MASS J01530024-3417360	(−8.21, −0.07, −0.27)	(+184.56, −2.96, +24.97)	(0.15, 11.34, 5.17)	0.97
2	HD 3567	(−8.19, +0.03, −0.09)	(+160.55, −13.61, −46.40)	(0.26, 10.61, 4.85)	0.95
3	2MASS J00512646-1053170	(−8.22, +0.06, −0.24)	(+156.24, +97.47, −109.61)	(2.54, 11.34, 5.39)	0.63
3	HE 0430-4901	(−8.62, −1.73, −1.63)	(−102.45, +62.92, −78.39)	(2.01, 10.07, 3.61)	0.67
3	2MASS J22562536-0719562	(−7.32, +1.73, −2.88)	(+106.56, +61.76, +41.20)	(1.75, 9.06, 3.24)	0.68
3	SDSS J173025.57+414334.7	(−7.41, +1.81, +1.26)	(−188.03, +152.28, +2.02)	(1.91, 13.08, 2.27)	0.75
3	HE 2224+0143	(−7.52, +1.56, −1.66)	(−0.67, +79.01, +6.80)	(1.75, 7.89, 2.67)	0.64
3	J03422816-6500355	(−8.04, −0.82, −0.77)	(+48.50, +90.61, +11.05)	(1.79, 8.42, 0.81)	0.65
3	BPS CS 22958-052	(−8.05, −0.59, −0.91)	(−151.18, +100.23, −29.59)	(2.31, 10.40, 1.21)	0.64
3	SDSS J004305.27+194859.20	(−8.66, +0.83, −0.88)	(+126.75, +63.23, +48.44)	(1.62, 10.31, 1.66)	0.73
3	BPS CS 22875-029	(−6.19, +0.07, −3.18)	(−117.12, +107.07, −160.86)	(2.52, 10.88, 7.17)	0.62
3	HD 115444	(−8.19, +0.15, +0.81)	(+161.39, +70.70, +14.86)	(1.41, 10.71, 1.19)	0.77
3	J01425445-0904162	(−8.72, +0.20, −1.42)	(+92.07, +100.09, +26.26)	(2.41, 9.76, 1.62)	0.60
3	G206-23	(−8.05, +0.24, +0.12)	(+219.91, +79.80, +135.48)	(2.29, 14.94, 10.11)	0.73
3	HD 221170	(−8.28, +0.47, −0.25)	(+135.27, +108.52, −34.37)	(2.54, 10.11, 0.94)	0.60
3	HE 0420+0123a	(−9.06, −0.20, −0.54)	(+54.96, +69.82, +104.20)	(2.05, 9.63, 5.17)	0.65
3	RAVE J015656.3-140211	(−9.40, +0.09, −3.34)	(−131.88, +67.37, −101.87)	(1.72, 13.28, 6.25)	0.77
3	BPS CS 22877-015	(−7.93, −0.28, +0.52)	(−12.52, +66.63, +23.92)	(1.33, 7.98, 0.69)	0.71
3	J12044314-2911051	(−7.63, −1.44, +1.01)	(−206.62, +69.56, −84.05)	(2.48, 12.09, 5.42)	0.66
3	2MASS J15271353-2336177	(−8.04, −0.04, +0.09)	(−59.40, +81.67, +52.71)	(1.73, 8.41, 1.08)	0.66
4	2MASS J21064294-6828266	(−6.88, −0.89, −1.18)	(−65.48, +122.55, +131.60)	(4.20, 7.41, 4.43)	0.28
4	J05383296-5904280	(−8.22, −0.94, −0.58)	(−75.68, +99.73, −121.73)	(3.32, 9.14, 4.80)	0.47
4	BPS CS 22945-017	(−7.62, −0.49, −0.89)	(−79.22, +130.01, −117.83)	(3.80, 8.82, 3.96)	0.40
4	2MASS J18174532-3353235	(+2.95, −0.19, −1.62)	(−21.94, −293.76, −44.82)	(3.13, 7.34, 2.93)	0.40
4	RAVE J133748.9-082617	(−5.69, −1.94, + 4.16)	(−103.27, +104.69, +13.55)	(3.27, 7.81, 4.47)	0.41
4	2MASS J15582962-1224344	(−5.82, −0.08, +1.38)	(+39.50, +164.13, +118.13)	(4.54, 6.24, 3.19)	0.16
4	2MASS J17163340-7009028	(−2.66, −4.31, −2.24)	(−117.59, +155.10, −65.05)	(4.25, 6.17, 3.07)	0.18
4	BPS CS 30306-132	(−6.17, +0.33, +2.52)	(−140.90, +157.82, +3.93)	(3.03, 9.26, 3.67)	0.51
4	J20435776-4408037	(−5.23, −0.18, −2.31)	(+63.54, +165.16, +6.40)	(3.33, 6.30, 2.54)	0.31
4	2MASS J21095804-0945400	(−5.56, +2.22, −2.40)	(+12.81, +150.41, −53.20)	(3.21, 6.86, 2.73)	0.36
4	2MASS J19215077-4452545	(−3.69, −0.54, −1.98)	(+47.63, +247.45, +84.07)	(3.37, 7.32, 3.25)	0.37
4	2MASS J17435113-5359333	(−6.17, −0.81, −0.46)	(−45.91, +116.40, −115.58)	(2.79, 6.46, 2.76)	0.40
5	2MASS J02462013-1518419	(−9.40, −0.32, −2.24)	(−213.35, −92.13, −141.23)	(2.13, 19.64, 12.19)	0.80
5	BPS CS 22953-003	(−6.94, −2.08, −3.48)	(+288.98, −24.11, +13.20)	(2.21, 18.57, 11.37)	0.79
5	HE 2327-5642	(−5.82, −1.74, −4.54)	(−99.19, −158.43, −230.10)	(2.76, 18.21, 13.67)	0.74
5	SMSS J183647.89-274333.1	(+3.05, +1.27, −1.83)	(−372.02, +98.61, −77.66)	(2.35, 18.07, 11.84)	0.77
5	HE 0300-0751	(−12.46, −0.53, −5.76)	(−108.23, −67.08, −72.96)	(2.13, 16.62, 7.51)	0.77
6	2MASS J05241392-0336543	(−14.36, −3.01, −2.62)	(−43.00, +164.91, −49.98)	(9.34, 15.03, 4.26)	0.23
6	2MASS J07150266-0154092	(−9.73, −1.19, +0.17)	(−6.45, +257.37, −14.71)	(9.58, 12.55, 0.40)	0.13
7	SMSS J062609.83-590503.2	(−8.32, −4.57, −2.23)	(−30.00, +324.42, +109.52)	(8.08, 28.85, 8.82)	0.56
7	HE 2244-1503	(−7.23, +1.12, −2.38)	(+45.63, +361.13, −99.01)	(7.62, 29.66, 10.95)	0.59

Table 3
(Continued)

k	Name	(x, y, z) kpc	(v_x, v_y, v_z) km s^{-1}	$(r_{\rm peri}, r_{\rm apo}, z_{\rm max})$ kpc	e
8	J07202253-3358518	(−8.62, −1.02, −0.16)	(+185.82, +15.88, +403.57)	(7.40, 64.49, 64.48)	0.79
8	Gaia DR2 2233912206910720000	(−8.13, +2.81, +0.70)	(−109.93, +4.20, −434.35)	(8.29, 66.88, 66.53)	0.78
9	SDSS J235718.91-005247.8	(−8.20, +0.24, −0.41)	(+105.97, −116.30, −189.87)	(5.50, 11.26, 9.09)	0.34
9	BPS CS 31082-001	(−8.61, +0.13, −1.76)	(+110.91, −101.01, −185.07)	(6.64, 11.31, 9.90)	0.26
9	SDSS J092157.27+503404.7	(−10.01, +0.41, +1.85)	(−55.97, −81.04, −145.81)	(5.34, 10.62, 8.82)	0.33
9	SMSS J051008.62-372019.8	(−8.59, −0.75, −0.59)	(−36.78, −99.74, −176.05)	(5.15, 9.63, 7.78)	0.30
9	BPS CS 22888-047	(−6.28, +0.29, −5.08)	(−61.20, −134.63, +129.04)	(6.19, 8.57, 7.01)	0.16
9	SMSS J195931.70-643529.3	(−0.04, −4.38, −5.66)	(+152.99, +93.75, −213.62)	(5.97, 13.70, 12.71)	0.39
10	HE 2301-4024	(−6.69, −0.11, −3.09)	(+55.72, −175.75, +293.15)	(5.88, 22.78, 18.92)	0.59
10	BPS CS 29491-069	(−7.08, +0.27, −1.87)	(−170.60, −173.70, + 279.92)	(6.93, 26.35, 22.64)	0.58
10	2MASS J19324858-5908019	(+1.76, −4.04, −5.75)	(+217.28, +174.23, −220.70)	(6.40, 25.64, 22.08)	0.60
10	HE 1131+0141	(−8.68, −4.87, +7.97)	(−154.75, −223.75, +17.18)	(6.01, 25.66, 21.71)	0.62
11	G15-13	(−8.10, +0.01, +0.12)	(+226.63, −217.34, +160.86)	(4.96, 25.35, 13.39)	0.67
11	G115-58	(−8.50, +0.04, +0.33)	(−197.67, −205.76, +176.38)	(5.52, 23.12, 12.95)	0.61
12	2MASS J22182082-3827554	(−6.90, +0.08, −1.89)	(+44.31, +144.55, −282.10)	(7.07, 16.07, 14.18)	0.39
12	2MASS J03270229+0132322	(−8.96, −0.02, −0.70)	(+23.87, +152.04, −270.56)	(8.98, 18.19, 15.54)	0.34
13	2MASS J14534137+0040467	(−2.04, −0.43, +7.48)	(−45.94, +71.82, +198.34)	(1.67, 12.68, 12.18)	0.77
13	2MASS J13052137-1137220	(−5.97, −2.78, +4.42)	(+62.41, +14.92, −171.30)	(1.51, 10.53, 10.36)	0.75
13	HE 1127-1143	(−7.96, −3.57, +3.74)	(+82.40, +23.00, +96.74)	(2.11, 10.09, 9.86)	0.65
13	SMSS J221448.33-453949.9	(−0.12, −1.20, −11.18)	(+75.39, +3.36, −12.43)	(2.67, 11.26, 11.19)	0.62
13	2MASS J12091322-1415313	(−7.72, −1.43, +1.65)	(+154.02, +7.74, +122.51)	(1.82, 10.49, 10.12)	0.70
13	RAVE J192632.8-584657	(−0.21, −3.19, −4.43)	(−14.20, −248.25, −77.29)	(1.35, 11.06, 11.05)	0.78
14	2MASS J15213995-3538094	(−6.72, −0.70, +0.54)	(+73.75, +321.10, +196.14)	(6.29, 25.91, 12.88)	0.61
14	2MASS J01553180-4919420	(−8.08, −0.67, −1.40)	(−238.57, +199.70, −125.90)	(4.72, 23.41, 7.69)	0.66
15	BPS CS 22892-052	(−6.26, +1.67, −3.34)	(−133.45, +89.29, −170.99)	(1.16, 12.36, 9.08)	0.83
15	2MASS J21091825-1310062	(−6.97, +0.89, −1.09)	(+58.32, +5.24, −76.82)	(0.24, 7.27, 4.25)	0.94
15	BPS CS 22945-058	(−7.51, −0.74, −1.16)	(−139.12, +14.97, + 37.04)	(0.45, 9.37, 4.23)	0.91
15	2MASS J14543792+0830379	(−6.18, +0.22, +2.94)	(−9.22, +25.82, +53.16)	(0.49, 7.07, 3.70)	0.87
15	SMSS J181505.16-385514.9	(−3.62, −0.46, −0.80)	(+214.17, +64.74, +94.03)	(0.59, 6.76, 2.93)	0.84
15	J00041581-5815524	(−6.66, −1.54, −3.41)	(−66.28, −26.43, −122.16)	(0.35, 8.94, 7.40)	0.93
15	2MASS J19014952-4844359	(−5.90, −0.48, −0.90)	(+95.70, +28.98, −32.62)	(0.30, 6.82, 3.42)	0.92
15	BD +17 3248	(−7.64, +0.45, +0.36)	(−40.91, +16.89, +61.18)	(0.27, 8.09, 4.13)	0.94
15	BPS CS 29529-054	(−8.11, −0.74, −0.68)	(+91.76, +42.19, +65.32)	(0.78, 9.17, 3.69)	0.84
15	2MASS J00405260-5122491	(−8.14, −0.05, −0.11)	(−19.76, +20.39, −55.05)	(0.36, 8.40, 3.88)	0.92
15	G210-33	(−8.14, +0.21, +0.01)	(+196.53, +43.46, +106.94)	(1.07, 12.54, 6.40)	0.84
15	2MASS J19232518-5833410	(−6.84, −0.53, −0.71)	(+126.08, +37.06, +93.25)	(0.41, 8.86, 4.16)	0.91
15	J18050641-4907579	(−4.15, −1.15, −0.96)	(+143.73, +98.98, −14.45)	(0.61, 6.08, 2.74)	0.82
15	RAVE J000738.2-034551	(−8.31, +1.08, −2.26)	(+90.25, +19.59, +56.90)	(0.91, 9.72, 3.37)	0.83
15	BPS BS 17569-049	(−5.96, +4.58, −4.13)	(−8.29, +12.49, +71.41)	(0.44, 8.66, 7.55)	0.90
15	J23342332-2748003	(−6.94, +0.61, −4.47)	(+9.13, +21.01, +31.61)	(0.41, 8.43, 4.79)	0.91
15	2MASS J13494713-7423395	(−6.42, −2.34, −0.60)	(−1.62, +22.31, −122.32)	(0.62, 6.89, 5.37)	0.83
15	SMSS J182601.24-332358.3	(−1.66, +0.03, −1.10)	(−325.19, +137.71, +13.95)	(0.68, 8.35, 3.46)	0.85
16	HE 1219-0312	(−7.22, −2.85, + 4.94)	(+83.95, −41.47, +13.54)	(1.89, 9.52, 5.67)	0.67
16	2MASS J20093393-3410273	(−3.63, +0.58, −2.64)	(+143.10, −199.81, +73.18)	(2.26, 8.37, 4.57)	0.57
16	2MASS J15383085-1804242	(−7.32, −0.16, +0.51)	(+58.30, −60.74, +95.84)	(1.39, 7.58, 3.76)	0.69
16	J07103110-7121522	(−8.05, −0.57, −0.24)	(−137.75, −80.92, +35.94)	(1.35, 9.96, 0.91)	0.76
16	2MASS J15211026-0607566	(−6.75, −0.10, +1.26)	(+99.28, −79.37, −137.91)	(1.96, 8.49, 5.07)	0.62
16	J20000364-3301351	(−4.98, +0.45, −1.69)	(−82.62, −81.94, −124.63)	(1.57, 6.26, 3.41)	0.60
16	RAVE J194550.6-392631	(−4.40, +0.01, −1.89)	(+12.50, −118.77, +37.76)	(1.83, 4.97, 2.01)	0.46
16	BPS BS 16543-097	(−7.78, +0.00, +2.38)	(−48.32, −71.31, −9.36)	(1.59, 8.51, 2.88)	0.69
16	RAVE J093730.5-062655	(−9.13, −1.74, +1.28)	(−136.26, −92.64, −75.55)	(1.92, 11.97, 6.48)	0.72
16	BPS CS 22882-001	(−7.27, −0.04, −6.36)	(−117.54, −64.38, −36.21)	(1.82, 11.28, 8.55)	0.72
16	RAVE J130524.5-393126	(−7.04, −1.57, +0.86)	(+59.37, −57.29, +61.05)	(1.35, 7.62, 2.91)	0.70
16	LP877-23	(−8.12, +0.05, −0.12)	(−27.43, −50.37, +138.34)	(1.99, 8.41, 6.71)	0.62

Table 3
(Continued)

k	Name	(x, y, z) kpc	(v_x, v_y, v_z) km s^{-1}	$(r_{\rm peri}, r_{\rm apo}, z_{\rm max})$ kpc	e
16	HE 1430+0053	(−6.58, −0.28, +2.26)	(−153.01, −87.23, −50.61)	(1.81, 8.89, 5.14)	0.66
17	Gaia DR2 6412626111276193920	(−1.62, − 2.87, −8.05)	(−155.15, −32.15, +49.07)	(5.80, 8.73, 8.39)	0.20
17	2MASS J00101758-1735387	(−8.14, +0.17, −0.70)	(+12.09, +69.73, −230.17)	(7.93, 8.65, 8.16)	0.04
17	2MASS J23362202-5607498	(−5.33, −2.17, −5.72)	(+22.98, +78.74, −170.80)	(4.69, 9.51, 9.11)	0.34
17	LAMOST J112456.61+453531.1	(−11.13, +1.06, +6.69)	(+30.82, +27.96, +111.51)	(3.69, 13.41, 12.87)	0.57
18	2MASS J03073894-0502491	(−12.57, −0.37, −5.37)	(+105.40, +152.25, +15.28)	(6.19, 16.66, 6.76)	0.46
18	HE 0432-0923	(−12.04, −1.82, −2.92)	(+70.18, +164.56, +97.15)	(6.34, 15.89, 6.72)	0.43
18	2MASS J02165716-7547064	(−6.73, −2.94, −2.75)	(+36.32, +304.34, −32.85)	(6.41, 17.54, 7.29)	0.46
19	SMSS J183128.71-341018.4	(−1.14, + 0.01, −1.36)	(+62.04, +218.16, −129.47)	(1.26, 3.59, 2.60)	0.48
19	2MASS J19161821-5544454	(−2.92, −1.78, −2.63)	(+26.46, +134.66, +4.58)	(1.50, 4.73, 3.11)	0.52
19	SMSS J183225.29-334938.4	(+2.41, +0.08, −2.06)	(−108.78, −112.82, +196.95)	(1.00, 6.12, 4.31)	0.72
19	SMSS J175738.37-454823.5	(+1.07, − 2.22, −1.75)	(−123.36, +69.85, −116.03)	(1.52, 3.54, 3.04)	0.40
19	2MASS J21224590-4641030	(−5.51, −0.33, −2.66)	(+29.80, +85.30, +185.37)	(2.95, 7.83, 6.66)	0.45
19	2MASS J18294359-4924253	(−2.12, −1.56, −1.88)	(−14.13, +100.32, −22.33)	(1.03, 3.27, 2.06)	0.52
19	J20411424-4654315	(−4.15, −0.49, −3.13)	(−141.10, +32.51, −45.25)	(0.71, 6.48, 4.33)	0.80
20	SMSS J155430.57-263904.8	(−2.07, −1.52, +2.38)	(−221.60, +334.62, −153.38)	(3.00, 24.61, 15.62)	0.78
20	2MASS J00524174-0902235	(−8.46, +0.42, −1.54)	(+256.12, +98.35, +171.26)	(2.74, 23.42, 14.99)	0.79
20	HE 0240-0807	(−16.06, −0.29, −12.29)	(+88.00, +65.08, +80.21)	(2.89, 23.85, 14.66)	0.78
20	RAVE J091858.9-231151	(−8.98, −2.49, +0.88)	(−285.97, +40.97, +114.24)	(2.68, 23.40, 8.65)	0.79
21	2MASS J14325334-4125494	(−7.38, −0.61, +0.34)	(−361.21, +107.37, −108.94)	(2.21, 33.16, 17.77)	0.88
21	Gaia DR2 1508756353921427328	(−8.21, +1.51, +3.53)	(−255.26, +179.86, +171.52)	(2.58, 33.16, 15.27)	0.86
22	2MASS J12170829+0415146	(−6.70, −7.10, +16.10)	(+8.28, −51.10, +189.72)	(3.64, 27.59, 26.53)	0.77
22	BPS CS 30315-029	(−5.30, +1.66, −10.75)	(+185.80, −119.50, +174.85)	(3.45, 27.59, 26.80)	0.78
23	HE 1226-1149	(−6.94, −2.72, +3.63)	(−7.05, +251.00, +145.04)	(8.19, 15.17, 9.97)	0.30
23	J22372037-4741375	(−5.59, −0.66, −4.06)	(−106.23, +265.37, +72.09)	(6.64, 14.00, 8.79)	0.36
23	J10401894-4106124	(−8.01, −1.24, +0.36)	(−62.18, +209.15, −211.66)	(8.05, 15.03, 9.77)	0.30
24	BPS CS 29497-004	(−7.94, +0.22, −3.49)	(−121.16, +180.59, −111.32)	(4.70, 13.91, 6.20)	0.49
24	BPS CS 31078-018	(−9.14, +0.15, −0.92)	(−83.65, +134.38, −32.65)	(3.50, 10.23, 1.31)	0.49
24	J22190836-2333467	(−7.09, +0.64, −1.82)	(+77.42, +157.78, +67.98)	(4.20, 8.27, 2.59)	0.33
24	BPS CS 22943-132	(−7.81, −0.02, −0.23)	(−64.51, +175.80, −129.83)	(5.67, 9.22, 4.10)	0.24
24	BPS CS 22886-012	(−7.64, +0.68, −0.96)	(+9.58, +151.83, +15.09)	(3.87, 7.73, 1.03)	0.33
24	J10191573-1924464	(−8.61, −2.58, +1.57)	(−41.93, +146.38, −6.45)	(4.51, 9.13, 1.58)	0.34
24	J06195001-5312114	(−8.26, −0.54, −0.25)	(+52.52, +160.86, −127.12)	(5.43, 9.27, 4.51)	0.26
24	J14354680-1124122	(−7.65, −0.20, +0.56)	(−9.07, +203.15, −11.19)	(6.04, 7.68, 0.60)	0.12
24	RAVE J183623.2-642812	(−6.57, −0.90, −0.75)	(−30.97, +192.79, −51.91)	(5.19, 6.71, 1.22)	0.13
24	HD 120559	(−8.16, −0.02, +0.02)	(−25.27, +183.04, −41.38)	(5.34, 8.29, 0.78)	0.22
24	2MASS J18295183-4503394	(−6.47, −0.31, −0.45)	(−34.22, +208.20, +40.95)	(5.46, 6.69, 0.81)	0.10
24	BD-10 3742	(−7.30, −0.67, +1.31)	(−78.18, +169.41, −13.45)	(4.51, 8.04, 1.52)	0.28
24	J06320130-2026538	(−8.50, −0.37, −0.10)	(−71.43, +150.84, +71.83)	(4.32, 9.18, 2.09)	0.36
24	RAVE J115941.7-382043	(−7.88, −0.75, +0.37)	(+16.92, +193.64, +17.56)	(5.44, 8.19, 0.50)	0.20
25	G166-37	(−8.11, +0.04, +0.20)	(+320.25, +72.45, +335.65)	(5.41, 79.72, 77.55)	0.87
25	HE 2252-4225	(+0.34, −1.05, −16.09)	(−95.53, −98.54, +349.18)	(4.94, 77.38, 77.25)	0.88
26	RAVE J040618.2-030525	(−8.97, −0.20, −0.61)	(−303.31, −4.82, −96.21)	(0.10, 24.05, 16.43)	0.99
26	LAMOST J110901+075441	(−9.42, −2.86, +5.22)	(+201.51, +100.16, −141.65)	(1.13, 23.07, 12.71)	0.91
26	Gaia DR2 3602288924850161792	(−8.10, −0.84, +1.39)	(−312.86, +9.36, −27.11)	(0.76, 21.62, 14.10)	0.93
26	CD -45 3283	(−8.20, −0.10, −0.00)	(−304.26, +10.89, −97.82)	(0.30, 21.67, 17.24)	0.97
27	Gaia DR2 4248140165233284352	(−4.99, +3.17, −1.00)	(−53.60, −82.15, +408.19)	(5.89, 32.46, 31.42)	0.69
28	G14-39	(−8.14, −0.04, +0.11)	(−203.13, +70.86, +243.07)	(4.74, 20.27, 19.06)	0.62
29	SMSS J024858.41-684306.4	(−7.45, −2.19, −2.29)	(+107.90, + 415.32, +215.11)	(6.28, 96.52, 42.29)	0.88
30	SMSS J063447.15-622355.0	(−7.93, − 6.95, −3.33)	(−39.11, +439.02, +157.36)	(7.94, 129.46, 45.67)	0.88

(This table is available in machine-readable form.)

we intentionally reserve the chemical information so that we can check the validity of our clustering result.

The sibling stars born in the same dwarf galaxy are expected to have similar chemical abundances, such as [Fe/H] or [Eu/H]. Indeed, the seven stars in Reticulum II with enhanced [Eu/Fe] abundance show a dispersion in [Fe/H] of $\sigma_{\rm [Fe/H]} = 0.35$ (Ji et al. 2016). If within a given cluster we found a dispersion that satisfies $\sigma_{\rm [Fe/H]} \leqslant 0.35$, there is a reasonably high probability that the cluster is genuine.[19,20] Among the 26 clusters with $N_{{\rm member},k} \geqslant 2$, 13 clusters satisfy $\sigma_{\rm [Fe/H]} \leqslant 0.35$, having metallicity dispersion equivalent to or smaller than that of Reticulum II. This result indicates that many of the field *r*-II stars may have originated from disrupted dwarf galaxies.

Following the procedure in Roederer et al. (2018a), we evaluated the statistical significance of the chemical homogeneity of each cluster as follows. First, for each cluster H22:DTC-*k* with $N_{{\rm member},k} \geqslant 2$, we compute the dispersions in [Fe/H] and [Eu/H], namely, $\sigma_{\rm [Fe/H]}$ and $\sigma_{\rm [Eu/H]}$, respectively. We then randomly draw $N_{{\rm member},k}$ stars from the 161 sample stars and compute a sample standard deviation in [Fe/H] and [Eu/H]. We repeat this process 5000 times to derive the probability distribution of the randomly drawn dispersions, $\sigma^{\rm random}_{\rm [Fe/H]}$ and $\sigma^{\rm random}_{\rm [Eu/H]}$. Finally, we compute the percentile rank of $\sigma_{\rm [Fe/H]}$ and $\sigma_{\rm [Eu/H]}$, which we denote $q_{\rm [Fe/H]}$ and $q_{\rm [Eu/H]}$.[21]

In Table 1, the clusters are shown in ascending order of $q_{\rm [Fe/H]}$. Among the 26 clusters with $N_{{\rm member},k} \geqslant 2$, 14 clusters have $q_{\rm [Fe/H]}$ below a threshold of $q_{\rm [Fe/H]} < 25\%$. (These 14 clusters have $\sigma_{\rm [Fe/H]} \leqslant 0.35$ except for the cluster H22:DTC-3 for which $\sigma_{\rm [Fe/H]} = 0.37$.) Therefore, about half of the clusters have a tight distribution in [Fe/H]. A similar trend is also seen for $\sigma_{\rm [Eu/H]}$.

To investigate the significance of the tight distribution in [Fe/H] for our *r*-II clusters, we performed an additional analysis by using a carefully constructed sample of $N = 161$ non-*r*-II stars from the literature. We find that our *r*-II clusters have a tighter distribution in [Fe/H] than the clusters of non-*r*-II stars found in this additional analysis (see Appendix H for the details).

Our result indicates that, in agreement with Roederer et al. (2018a) and Gudin et al. (2021), *r*-enhanced stars with similar orbits tend to have similar chemistry. This result is consistent with a scenario wherein *r*-II stars were born in *r*-enhanced dwarf galaxies, similar to the UFD Reticulum II, that were later tidally disrupted when they merged with the Milky Way.

[19] There is no guarantee that a genuine cluster has a tight [Fe/H] distribution (or other chemical abundance distribution). However, if a dynamically identified cluster happens to have a tight distribution in [Fe/H], we are more confident in our clustering result. This is the motivation to use chemical abundance information to *validate* our results. Even if a given cluster identified in our analysis has a broad distribution in [Fe/H], it does not necessarily mean that the cluster is illusory, rather, it signals that we are *less confident* about that cluster.

[20] Simulated Eu-rich dwarf galaxies also have similar chemical properties. According to Figure 15(d) of Hirai et al. (2022), low-mass dwarf galaxies named Halo 11, 12, 13, 14, and 16 in their simulation have two or more *r*-II stars. These systems, respectively, exhibit $\sigma_{\rm [Fe/H]} = 0.19$, 0.38, 0.55, 0.39, and 0.15 and $\sigma_{\rm [Eu/Fe]} = 0.19$, 0.09, 0.53, 0.26, and 0.18.

[21] In principle, we could perform the same analysis by using [Eu/Fe] and derive $\sigma_{\rm [Eu/Fe]}$ and $q_{\rm [Eu/Fe]}$. However, it turns out that these quantities are not meaningful. This is because the distribution of [Eu/Fe] in our sample is highly skewed and a large fraction of our sample stars has [Eu/Fe] very close to the lower limit (0.7). Due to this skewed distribution, randomly chosen stars have a high probability of having small dispersion in [Eu/Fe]. For example, a randomly chosen pair of stars have a 75% probability of having $\sigma_{\rm [Eu/Fe]} < 0.2$.

7.2. Individual Clusters

Among 30 clusters, 26 clusters have $N_{{\rm member},k} \geqslant 2$ and four clusters have $N_{{\rm member},k} = 1$. Based on the distribution of the chemical abundances in each cluster, we categorize 18 clusters that have $N_{{\rm member},k} \geqslant 2$ and show a tight chemical abundance distribution into Tiers 1, 2, 3, and 4. This classification reflects our confidence, such that we have the highest confidence in Tier 1 clusters. In addition, there are four clusters with one member star ($N_{{\rm member},k} = 1$). We do not further discuss the remaining eight clusters, which have $N_{{\rm member},k} \geqslant 2$ and broad distributions in [Fe/H] and [Eu/H].

7.2.1. Tier 1: Six Best Clusters

Among the 26 clusters with $N_{{\rm member},k} \geqslant 2$, six clusters H22:DTC-1, 2, 3, 4, 5, and 9 have tight distributions in both [Fe/H] and [Eu/H]. Specifically, both $q_{\rm [Fe/H]}$ and $q_{\rm [Eu/H]}$ are below 15%. (Both $q_{\rm [Fe/H]}$ and $q_{\rm [Eu/H]}$ are below ∼5% for five clusters, H22:DTC-1, 2, 3, 4, and 5.) Thus, the probability that all of these six clusters reflect a chance alignment of [Fe/H] values is extremely low. We label these clusters as Tier 1 clusters. Based on the chemical properties, we are most confident with our clustering results for Tier 1 clusters.

Figure 4 shows the distribution of $\boldsymbol{J}$, [Fe/H], and [Eu/H] for Tier 1 clusters. We see that the member stars are distributed roughly within 200 kpc km s^{-1} from the cluster centroid in the $\boldsymbol{J}$ space. We visually confirm the tight distribution of [Fe/H] and [Eu/H], which characterizes Tier 1 clusters.

To obtain additional insights into the progenitor systems of Tier 1 clusters, Figure 5 shows the distribution of [Fe/H] and [α/Fe] of their member stars. The values of [Mg/Fe] and [Ca/Fe] are curated from high-resolution spectroscopic measurements in the literature. Although some member stars do not have reliable measurements and are not shown, we can grasp the overall trend of the abundance of α-elements from Figure 5. Importantly, all Tier 1 clusters show a reasonably tight distribution in the [Fe/H]–[Mg/Fe] and [Fe/H]–[Ca/Fe] planes. The fact that Tier 1 clusters have tight distributions not only in (Fe, Eu) but also in (Mg, Ca) abundances is evidence in support of these clusters being remnants of dwarf galaxies that merged with the Milky Way. Furthermore, we see a hint of a decreasing trend of [α/Fe] as a function of [Fe/H] for clusters H22:DTC-1 and 4, which is reminiscent of the trends seen in classical dwarf galaxies, such as Sculptor and Ursa Minor (e.g., Tolstoy et al. 2009; Kirby et al. 2011), and UFDs, such as Hercules and Reticulum II (Vargas et al. 2013; Ji et al. 2022). If this trend is real, it may provide a clue that the progenitor systems of these clusters experienced a quiescent star formation activity.

The distribution of position $\boldsymbol{x}$ and velocity $\boldsymbol{v}$ of the member stars provides additional insights into the progenitor systems of Tier 1 clusters. As can be seen in the top row in Figure 6, the member stars in each Tier 1 cluster show a wide spatial distribution. This spatial distribution suggests that the member stars have different orbital phases, although they have similar orbits. The bottom row in Figure 6 further supports this view. We see that, for clusters H22:DTC-1, 2, 3, and 4, there are almost equal numbers of stars with $v_R > 0$ (approaching apocenter), $v_R < 0$ (approaching pericenter), $v_z > 0$ (moving upward), and $v_z < 0$ (moving downward). For clusters H22:DTC-5 and 9, there are almost equal numbers of stars with $v_R > 0$ and $v_R < 0$, while stars with $v_z < 0$ dominate. (The

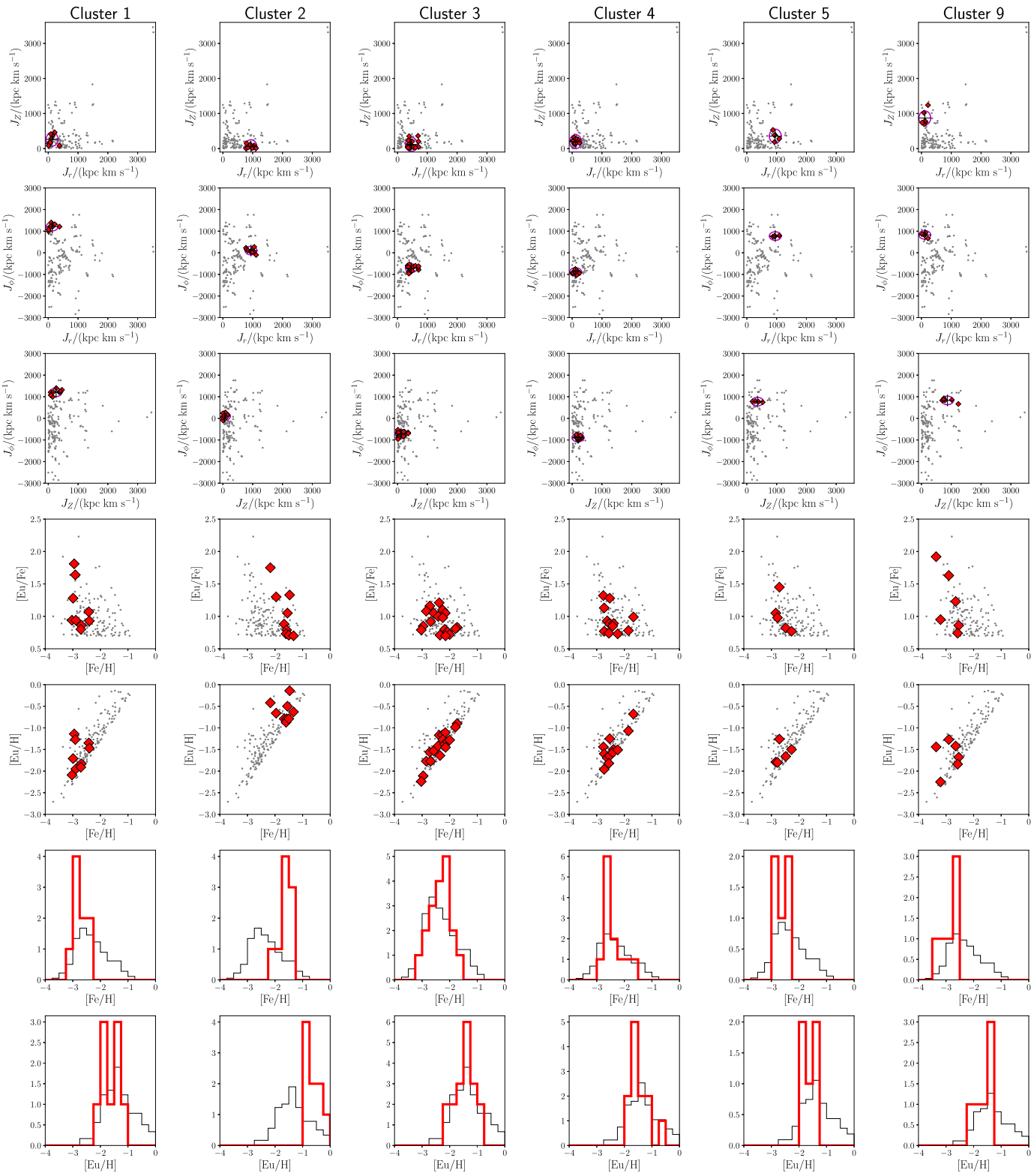

Figure 4. The properties of stars in Tier 1 clusters, for which we have the highest confidence. From the left to right column, we show clusters H22:DTC-1, 2, 3, 4, 5, and 9. In each panel, the red diamonds correspond to the member stars, while small gray dots correspond to the other stars. (The first three rows): the distribution of the orbital action. The black cross denotes the location of the centroid ($\langle J_r \rangle$, $\langle J_z \rangle$, and $\langle J_\phi \rangle$). The magenta circle with a radius of 200 kpc km s^{-1} is shown to guide the eye. (Fourth and fifth rows): the distribution of stars in the chemical abundance space. We note that the chemical abundance information is not used in the clustering analysis, and is used for validation. (Sixth and seventh rows) the distribution of [Fe/H] and [Eu/H] in the cluster are shown by the red histogram. The black histogram shows the distribution of [Fe/H] and [Eu/H] for the entire *r*-II sample, which is normalized so that the areas under the black and red histograms are the same.

member stars in each cluster have similar values of v_ϕ because they have similar values of $J_\phi = Rv_\phi$.) This result means that most Tier 1 clusters are apparently completely phase mixed, suggesting that the disruption of the progenitor systems happened long ago. Therefore, Tier 1 clusters are likely the remnants of completely disrupted dwarf galaxies that merged

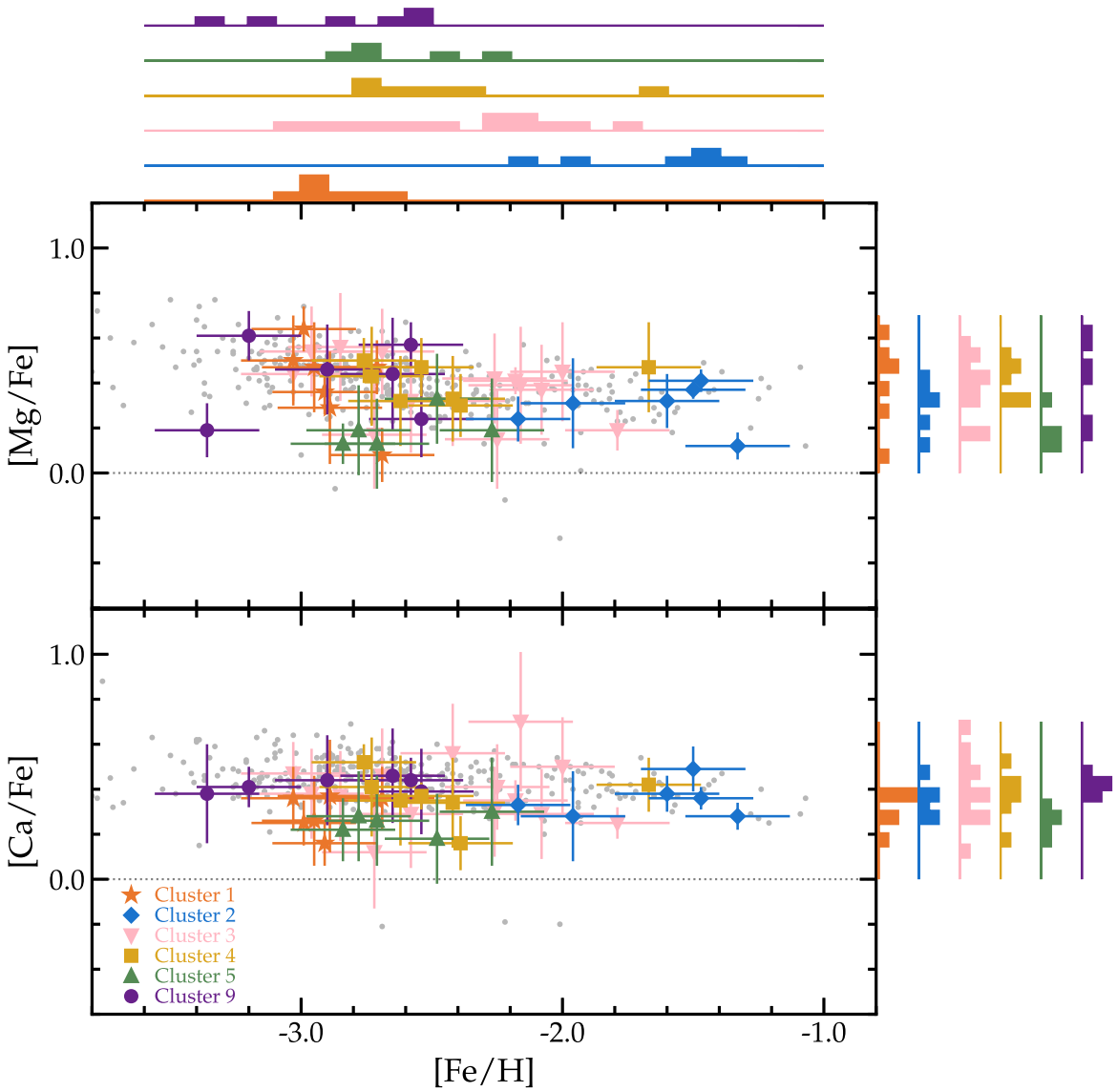

Figure 5. The distributions of stars in the [Fe/H]–[Mg/Fe] space (top) and [Fe/H]–[Ca/Fe] space (bottom) for Tier 1 clusters (H22:DTC-1, 2, 3, 4, 5, and 9). These distributions are reminiscent of those of dwarf galaxies orbiting around the Milky Way. Histograms of [Fe/H], [Mg/Fe], and [Ca/Fe] are shown on the top or right of each panel. The abundance ratios for individual stars in the clusters identified in this work are adopted from Westin et al. (2000), Hill et al. (2002), Cayrel et al. (2004), Honda et al. (2004), Barklem et al. (2005), Ivans et al. (2006), François et al. (2007), Frebel et al. (2007), Aoki et al. (2010), Mashonkina et al. (2010), Hollek et al. (2011), Hansen et al. (2012), Ishigaki et al. (2012, 2013), Johnson et al. (2013), Roederer et al. (2014b, 2018a), Howes et al. (2015), Jacobson et al. (2015), Navarrete et al. (2015), Placco et al. (2017), Cain et al. (2018), Hansen et al. (2018), Holmbeck et al. (2018), Sakari et al. (2018a), Bandyopadhyay et al. (2020), Ezzeddine et al. (2020), Hanke et al. (2020), Rasmussen et al. (2020), and Zepeda et al. (2022). The small gray points mark field stars from Roederer et al. (2014b). The dotted lines mark the solar ratios.

with the ancient Milky Way. Of course, it is premature to conclude decisively that they really are disrupted dwarf galaxies, and we discuss the prospects of confirming these *r*-II clusters in Section 7.5.

In the following, we summarize other basic properties of Tier 1 clusters:

Tier 1 cluster H22:DTC-1. This cluster is a newly discovered cluster characterized by retrograde, round orbits with $\langle J_\phi \rangle = 1209\,\mathrm{kpc\,km\,s^{-1}}$. This cluster is metal-poor, with $\langle$[Fe/H]$\rangle = -2.78$. This cluster is rather large ($N_{\mathrm{member},k} = 9$), but its metallicity dispersion is only $\sigma_{\mathrm{[Fe/H]}} = 0.22$. In terms of $q_{\mathrm{[Fe/H]}}$, this cluster has the tightest distribution of [Fe/H] among the 30 clusters. The clusters H22:DTC-1 and 9 have a similar orbit and chemistry, which will be discussed in Section 7.4. Intriguingly, two member stars of the cluster H22:DTC-1 (2MASS J09544277+5246414 and BPS CS 22896-154) were also analyzed by Roederer et al. (2018a); however, they are regarded as *r*-II stars that are not associated with any kinematic groups in Roederer et al. (2018a).

Tier 1 cluster H22:DTC-2. This cluster is characterized by highly eccentric orbits with $r_{\mathrm{peri}} < 1\,\mathrm{kpc}$ and $r_{\mathrm{apo}} > 10\,\mathrm{kpc}$. This cluster is a metal-rich cluster, with $\langle$[Fe/H]$\rangle = -1.65$. In terms of $q_{\mathrm{[Eu/H]}}$, this cluster has the tightest distribution in Eu abundance. This cluster corresponds to group D in Roederer et al. (2018a), containing all three stars in group D. One of the member stars, HD 222925, is the most well-studied *r*-II star in terms of its chemistry (Roederer et al. 2022).

Tier 1 cluster H22:DTC-3. This cluster is characterized by prograde, eccentric orbits with $\langle J_\phi \rangle = -711\,\mathrm{kpc\,km\,s^{-1}}$. This cluster is one of the largest clusters in our analysis, with

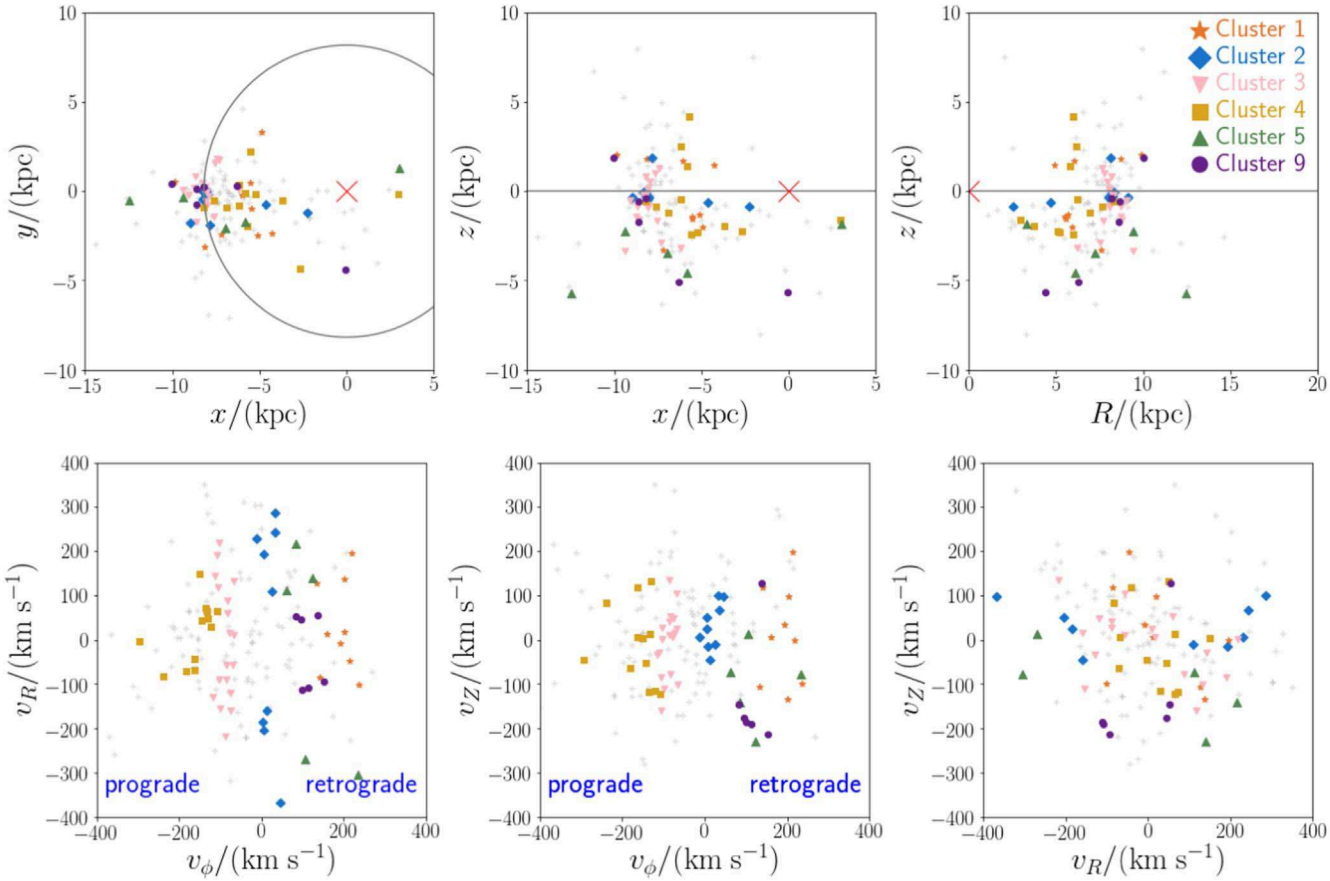

Figure 6. Position and velocity of the member stars of Tier 1 clusters (H22:DTC-1, 2, 3, 4, 5, and 9; colored symbols) and other *r*-II stars (light-gray cross). In the top panels, we use the Galactocentric Cartesian coordinate (x, y, z), such that the Sun is located at $(x, y, z) = (-8.178, 0, 0)$ kpc. As a reference, we show the solar circle (gray circle in the top left panel) and the location of the Galactic center (red × in the top panels). In the bottom panels, we use the velocity in the Galactocentric cylindrical coordinate (v_R, v_ϕ, v_z), such that prograde stars have $v_\phi < 0$.

$N_{\mathrm{member},k} = 18$. The face value of the dispersion in [Fe/H] is relatively large, $\sigma_{[\mathrm{Fe/H}]} = 0.37$, but its low percentile $q_{[\mathrm{Fe/H}]} = 1.86\%$ suggests that this cluster has a tight distribution in [Fe/H] (given its large $N_{\mathrm{member},k}$). This cluster includes four out of four stars from group A and two out of three stars from group F in Roederer et al. (2018a). This cluster also includes an *r*-II star (2MASS J22562536-0719562) that is associated with the DTG38 in Yuan et al. (2020).[22]

Tier 1 cluster H22:DTC-4. This cluster is a dynamically cold cluster with an internal action dispersion of $\sigma_k = 63\,\mathrm{kpc\,km\,s^{-1}}$. The member stars show prograde, mildly eccentric orbits with $\langle J_\phi \rangle = -889\,\mathrm{kpc\,km\,s^{-1}}$, which corresponds to a guiding center radius of $R \sim 4$ kpc. The very metal-poor nature of this group, $\langle [\mathrm{Fe/H}] \rangle = -2.42$, is in contrast to the majority of the disk stars at $R \sim 4$ kpc. This cluster corresponds to group C in Roederer et al. (2018a), containing three out of four stars in group C. Our method finds nine additional members of this group.

Tier 1 cluster H22:DTC-5. This cluster is characterized by retrograde, eccentric orbits with $\langle J_\phi \rangle = 773\,\mathrm{kpc\,km\,s^{-1}}$. This cluster has the smallest $\sigma_{[\mathrm{Fe/H}]}$ and $\sigma_{[\mathrm{Eu/H}]}$ among the Tier 1 clusters. This cluster corresponds to group G in Roederer et al. (2018a), containing two out of two stars in group G. Our method finds three additional member stars of this group. Two of the new members (SMSS J183647.89-274333.1 and HE 0300-0751) have a poor measurement of the parallax ($\varpi/\sigma_\varpi < 4$; see Table 2), which highlights the advantage of using our clustering method.

Tier 1 cluster H22:DTC-9. This cluster is characterized by retrograde, round orbits with $\langle J_\phi \rangle = 829\,\mathrm{kpc\,km\,s^{-1}}$. This cluster is one of the lowest metallicity clusters, with $\langle [\mathrm{Fe/H}] \rangle = -2.87$. It corresponds to group B in Roederer et al. (2016), containing three out of four stars in group B. This cluster also corresponds to a DTG, DTG10, in Yuan et al. (2020).[23]

7.2.2. 12 Other Clusters: Tiers 2, 3, and 4

Apart from Tier 1 clusters, we choose 12 clusters with reasonably small $q_{[\mathrm{Fe/H}]}$ and/or $q_{[\mathrm{Eu/H}]}$ and categorize them as Tier 2, 3, and 4 clusters (see comment in Table 1). All the clusters in Tiers 2 and 3 are newly discovered. The details are described in Appendix C.

[22] The DTG38 in Yuan et al. (2020) contains not only 2MASS J22562536−0719562 but also another *r*-II star 2MASS J00405260-5122491, which is included in the cluster H22:DTC-15. Although Yuan et al. (2020) claim these two *r*-II stars are associated with a single group (DTG38), our analysis associates them with two clusters (clusters H22:DTC-3 and 15) with similar orbital properties.

[23] The DTG10 in Yuan et al. (2020) includes two *r*-II stars (BPS CS 31082-001 and SDSS J235718.91−005247.8), both of which are included in group B in Roederer et al. (2018a).

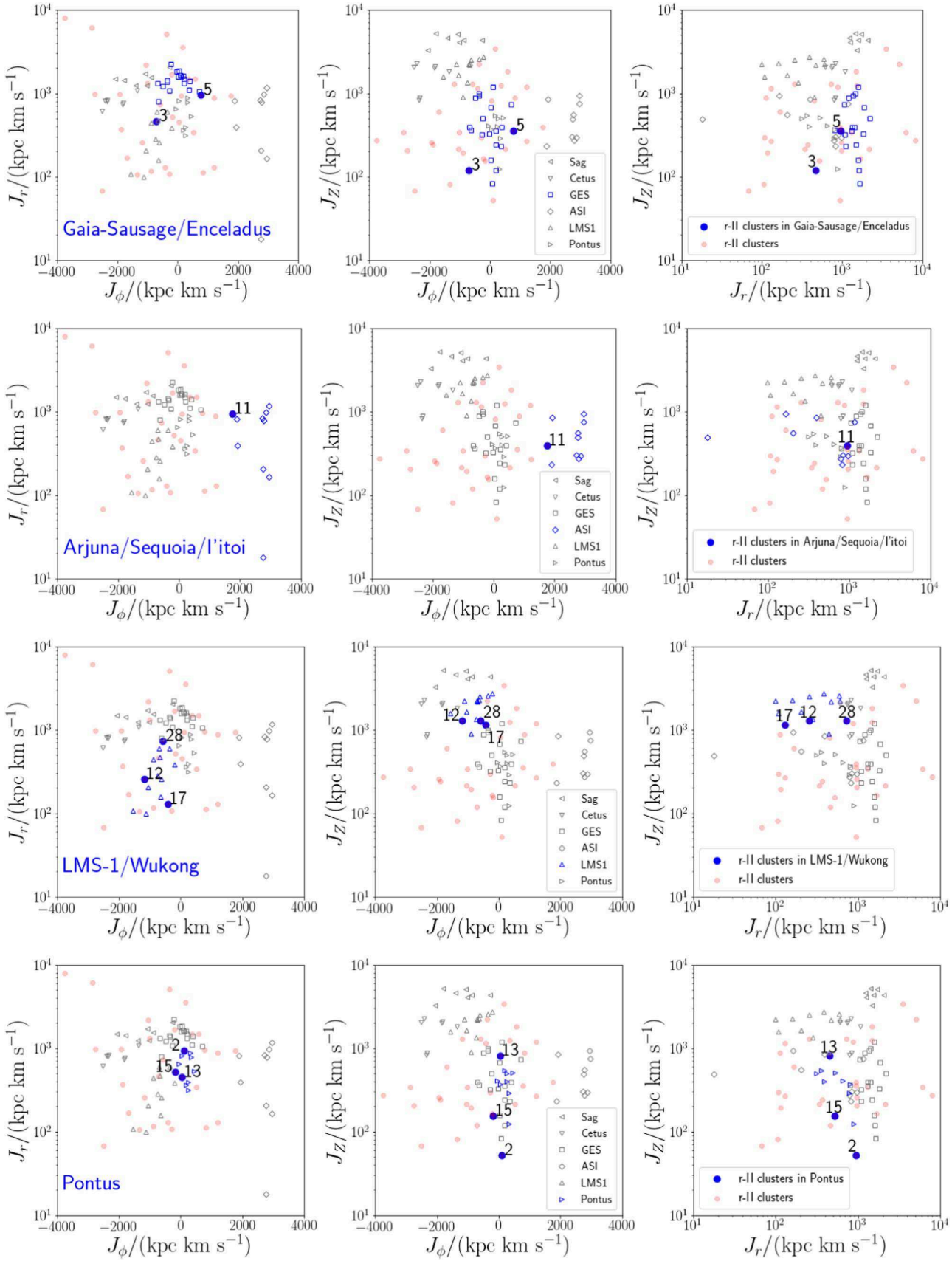

Figure 7. Associations of our clusters and the known big merger groups in Malhan et al. (2022). In all panels, the filled symbols represent the *r*-II clusters in our analysis, and the open symbols represent the stellar streams and globular clusters in the merger groups. In each row, we highlight one of the merger groups with blue symbols. The rest of the merger groups are shown by gray symbols. The clusters associated with the highlighted merger group are shown by blue-filled circles. (The number corresponds to *k* of the *r*-II cluster H22:DTC-*k*.) The rest of the clusters are shown by light-red filled circles. We do not find clusters associated with the merger groups Sagittarius and Cetus.

7.2.3. One Member Clusters

Four clusters only have one member star (H22:DTC-27, 28, 29, and 30). The star in the cluster H22:DTC-29 (SMSS J024858.41-684306.4) has $[Fe/H] = -3.71$, while the star in the cluster H22:DTC-30 (SMSS J063447.15-622355.0) has $[Fe/H] = -3.41$. These two stars are the two most metal-poor stars in our catalog.

Although our clustering analysis assigns these extremely metal-poor *r*-II stars to separate single member clusters, they have similar orbital properties. For example, as can be seen in Table 3, both stars have prograde orbits with high eccentricity ($ecc \simeq 0.88$) and have similar pericentric and apocentric radii ($r_{\rm peri} \simeq 8$ kpc and $r_{\rm apo} > 90$ kpc). These similarities indicate that their origins might be related to each other, but we do not further discuss their connection in this paper.

In our analysis, the extremely metal-poor stars SMSS J024858.41-684306.4 and SMSS J063447.15-622355.0 (which are the only members of clusters H22:DTC-29 and 30, respectively) do not have sibling stars in our catalog. This result can be understood from chemical and dynamical points of view. If each of these stars was formed in a dwarf galaxy, the total stellar mass of its progenitor dwarf galaxy may have been small, according to the mass–metallicity relationship of the dwarf galaxies (Kirby et al. 2013; Naidu et al. 2022). Therefore, it is reasonable that these extremely metal-poor stars have a rather small number of sibling stars ($\lesssim 10^3$ stars) in the Galactic halo. Also, the fact that these two stars have highly eccentric orbits (with $r_{\rm apo} > 90$ kpc) means that most of their sibling stars are in the outer part of the Galactic halo. Because our catalog is restricted to bright *r*-II stars, and most of the *r*-II stars in our catalog are within 10 kpc from the Sun, the apparent lack of sibling stars may be understood as the spatial selection bias of the sample stars (see Hattori & Yoshii 2011).

7.3. Connection to the Past Merger Events

Malhan et al. (2022) analyzed the kinematics of the dynamical tracers in the Milky Way (i.e., stellar streams, globular clusters, and dwarf galaxies) and found that these tracers show a clumpy distribution in the orbital action and energy space (see also a similar analysis by Bonaca et al. 2021). They identified six groups of dynamical tracers, namely, (i) the Gaia-Sausage/Enceladus merger group; (ii) the Arjuna/Sequoia/I'itoi merger group; (iii) the LMS-1/Wukong merger group; (iv) the Pontus merger group; (v) the Cetus merger group; and (vi) the Sagittarius merger group. They claimed that these groups correspond to the past merger events in the Milky Way.

To investigate if any of our clusters are associated with these merger groups, we check the distribution of the actions of the clusters and the merger groups in Malhan et al. (2022). First, we adopt the literature values of the point estimate of the orbital actions for the stellar streams from Malhan et al. (2022) and for the globular clusters from Vasiliev & Baumgardt (2021) (see the bottom row in Figure 3). We note that they computed the orbital actions with slightly different assumptions on the position and velocity of the Sun, but this difference has a minor effect on the values of actions (with a typical difference of $\sim$100 kpc km s^{-1}). We neglect this minor effect because our conclusion is not affected. Second, we compute the Euclidian distance from our *r*-II clusters to the stellar streams and globular clusters in the action space. Third, for each *r*-II cluster, we find the nearest neighbor stellar stream and globular cluster. If the distance to the nearest neighbor object (stream or globular cluster) satisfies $||\boldsymbol{J}_{r\rm IIcluster} - \boldsymbol{J}_{\rm nearest}|| < 600$ kpc km s^{-1}, and if the nearest neighbor object is a member of a certain merger group (among the abovementioned six merger groups (i)–(vi)), we interpret that the *r*-II cluster is also associated with the same merger group.

As a result, we find eight *r*-II clusters that are associated with four merger groups (as summarized below), and there are no *r*-II clusters that are associated with the Cetus and Sagittarius merger groups.

(i) Gaia-Sausage/Enceladus Merger Group

Two *r*-II clusters, H22:DTC-3 and 5, are dynamically associated with the Gaia-Sausage/Enceladus merger group (see the top row in Figure 7). The mean metallicity of these *r*-II clusters is $\langle [Fe/H] \rangle = -2.37$ and -2.62, respectively. These *r*-II clusters are more metal-poor than the majority of the stellar streams and globular clusters associated with the Gaia-Sausage/Enceladus merger group ($-2.4 \leqslant [Fe/H] \leqslant -1.1$) (Malhan et al. 2022).

1. For the *r*-II cluster H22:DTC-3, the nearest neighbor object is the NGC 7089 stream ($[Fe/H] = -1.46 \pm 0.06$; Horta et al. 2020), which is a member of the Gaia-Sausage/Enceladus merger group. As can be seen in Figure 4, this *r*-II cluster shows a wide distribution in [Fe/H] (covering $-3.03 \leqslant [Fe/H] \leqslant -1.73$), which is roughly consistent with the lower-metallicity part of the Gaia-Sausage/Enceladus merger group.
2. For the *r*-II cluster H22:DTC-5, the nearest neighbor objects are the C-7 stream (metallicity is unknown) and NGC 2298 ($[Fe/H] = -1.76 \pm 0.05$; Baeza et al. 2022), both of which are the members of this merger group. Given that this *r*-II cluster has $\langle [Fe/H] \rangle = -2.62$, it may be the most metal-poor member of this merger group.

(ii) Arjuna/Sequoia/I'itoi merger group

One *r*-II cluster, H22:DTC-11, is dynamically associated with the Arjuna/Sequoia/I'itoi merger group (see the second row in Figure 7). The mean metallicity of this *r*-II cluster is $\langle [Fe/H] \rangle = -1.39$. This metallicity is slightly higher than the metallicities of the stellar streams and globular clusters associated with the Arjuna/Sequoia/I'itoi merger group ($-2.24 \leqslant [Fe/H] \leqslant -1.56$) (Malhan et al. 2022).

1. The nearest neighbor to the *r*-II cluster H22:DTC-11 is the Phlegethon stream ($[Fe/H] = -1.96 \pm 0.05$; Martin et al. 2022), which is a member of this merger group (Malhan et al. 2022). Given that this *r*-II cluster has a mean metallicity $\langle [Fe/H] \rangle = -1.39$, it may be the most metal-rich member of this merger group.

(iii) LMS-1/Wukong merger group

Three *r*-II clusters, H22:DTC-12, 17, and 28, are dynamically associated with the LMS-1/Wukong merger group (see the third row in Figure 7). The mean metallicities of these *r*-II clusters are $\langle [Fe/H] \rangle = -2.48$, -1.94, and -1.88, respectively. These metallicities are consistent with the metallicities of the stellar streams and globular clusters associated with the LMS-1/Wukong merger group ($-3.38 \leqslant [Fe/H] \leqslant -1.35$) (Malhan et al. 2022).

1. For the *r*-II cluster H22:DTC-12, the nearest neighbor object is Pal 5 ($[Fe/H] = -1.35 \pm 0.06$; Ishigaki et al. 2016),

which is a member of this merger group (Malhan et al. 2022).
2. The *r*-II cluster H22:DTC-17 is also associated with this merger group, but our reasoning mainly comes from external knowledge that this cluster includes an *r*-II star (Hansen et al. 2021) associated with the Indus stream ($[\mathrm{Fe/H}] = -1.96 \pm 0.33$; Li et al. 2022b) and that the Indus stream is a member of the LMS-1/Wukong group.
3. For the *r*-II cluster H22:DTC-28, which is a one member cluster, the nearest neighbor objects are Pal 5 and NGC 5272 (M3; $[\mathrm{Fe/H}] = -1.45 \pm 0.03$; Sneden et al. 2004), both of which are members of this merger group.

(iv) Pontus merger group

Three *r*-II clusters, H22:DTC-2, 13, and 15, are dynamically associated with the Pontus merger group (see the bottom row in Figure 7). The mean metallicities of these *r*-II clusters are $\langle[\mathrm{Fe/H}]\rangle = -1.65$, -2.51, and -2.43, respectively. It is intriguing that two of these *r*-II clusters are more metal-poor than the stellar streams and globular clusters associated with the Pontus merger group ($-2.3 \leqslant [\mathrm{Fe/H}] \leqslant -1.3$) (Malhan et al. 2022).

1. For the *r*-II cluster H22:DTC-2, the nearest neighbor object is the anomalous globular cluster NGC 5286 ($[\mathrm{Fe/H}] = -1.72 \pm 0.11$; Marino et al. 2015), which is a member of the Pontus merger group (Malhan et al. 2022).
2. For the *r*-II cluster H22:DTC-13, the nearest neighbor objects are NGC 6341 (M92; $[\mathrm{Fe/H}] = -2.34 \pm 0.04$; Sneden et al. 2000) and NGC 7099 (M30; $[\mathrm{Fe/H}] = -2.34 \pm 0.07$; Carretta et al. 2009), both of which are members of this merger group.
3. For the *r*-II cluster H22:DTC-15, the nearest neighbor objects are M92 and NGC 4833 ($[\mathrm{Fe/H}] = -2.19 \pm 0.02$; Roederer & Thompson 2015), both of which are members of this merger group.

7.4. A Very Metal-poor Merger Group Candidate

Two Tier 1 clusters, H22:DT-1 and 9, are very metal-poor with $\langle[\mathrm{Fe/H}]\rangle \simeq -2.8$. As seen in Section 7.2.1, these clusters have tight distributions in chemical abundances, making them reliable candidates for disrupted dwarf galaxies. Interestingly, these two clusters have very similar dynamical and chemical properties.

The orbital actions of these *r*-II clusters are characterized by

$$(J_r, J_z, J_\phi) = \begin{cases} (129 \pm 107, 265 \pm 140, 1209 \pm 112) & (\mathrm{H22{:}\ DTC-1}) \\ (112 \pm 60, 873 \pm 193, 829 \pm 79) & (\mathrm{H22{:}\ DTC-9}). \end{cases} \quad (25)$$

The distance between these *r*-II clusters in the $\boldsymbol{J}$ space is only 717 kpc km s^{-1}, which is much smaller than the typical distance between two points randomly drawn in the action space. For example, if we randomly draw two *r*-II clusters from the 30 clusters in Table 1, we only have a 4.4% chance of getting a distance smaller than 717 kpc km s^{-1}. Therefore, it is likely that these clusters are dynamically associated with each other. Intriguingly, as can be seen in the third row in Figure 3, these two *r*-II clusters are away from all of the big merger groups in Malhan et al. (2022), such as the Gaia-Sausage/Enceladus merger group or Pontus merger group (see also Section 7.3).

The chemistry of these clusters is characterized by

$$([\mathrm{Fe/H}], [\mathrm{Eu/H}]) = \begin{cases} (-2.78 \pm 0.22, -1.64 \pm 0.32) & (\mathrm{H22{:}\ DTC-1}) \\ (-2.87 \pm 0.31, -1.65 \pm 0.33) & (\mathrm{H22{:}\ DTC-9}). \end{cases} \quad (26)$$

The similarity of the chemical properties indicates that these clusters may have experienced a similar star formation history.

Based on the chemo-dynamical similarity and the fact that they are separated from other merger groups, we postulate that these *r*-II clusters may be the remnants of two very metal-poor dwarf galaxies that merged with the Milky Way together, corresponding to yet another merger event.

In the following, we estimate the stellar mass of the progenitor dwarf galaxies of the *r*-II clusters H22:DTC-1 and 9, which we refer to as M_*(H22:DTC-1) and M_* (H22:DTC-9), respectively. According to the mass-mean metallicity relationship of the disrupted dwarf galaxies (Naidu et al. 2022; see also Kirby et al. 2013),

$$\langle[\mathrm{Fe/H}]\rangle = (-2.11^{+0.11}_{-0.12}) + (0.36^{+0.12}_{-0.04}) \log_{10}\left(\frac{M_*}{10^6 M_\odot}\right), \quad (27)$$

disrupted dwarf galaxies with $\langle[\mathrm{Fe/H}]\rangle \simeq -2.8$ typically have a stellar mass of $M_* \sim 10^4\ M_\odot$. Thus, given the mean metallicity in Equation (26), we have M_* (H22:DTC-1) $\sim$ M_*(H22:DTC-9) $\sim 10^4\ M_\odot$.

Our estimate of M_* is supported by the distribution of stars in the color–magnitude diagram for each *r*-II cluster. Based on the Padova stellar evolution model (Bressan et al. 2012; v3.6), a stellar population with an initial total mass of $10^4\ M_\odot$ and metallicity of $[\mathrm{Fe/H}] = -2.8$ is expected to have, on average, 4.4 stars with $M_G < 0$ (brighter than the majority of the horizontal branch stars) at the age of 10 Gyr. The expected number (4.4) is, at face value, consistent with the observation: we have seven and three stars with $M_G < 0$ in *r*-II clusters H22:DTC-1 and 9, respectively. Of course, we admit that this argument needs to be treated with care because we do not know the completeness of the member stars with $M_G < 0$ and the contamination in our *r*-II clusters. However, the distribution of stars in the color–magnitude diagram is at least consistent with the view that the progenitor dwarf galaxies of our *r*-II clusters H22:DTC-1 and 9 had $M_* \sim 10^4\ M_\odot$ before they were disrupted.

7.5. Prospects for Confirming Our r-II Clusters

The aim of this paper is to find candidates for *r*-II clusters that are likely remnants of disrupted dwarf galaxies. Due to the optimistic nature of our clustering method, at this moment it is premature to conclusively determine whether any of these *r*-II clusters are real. Here, we discuss two prospects to confirm or refute the reality of these *r*-II clusters.

Because dwarf galaxies have their own chemical enrichment history, dwarf galaxies show different trends in ([Fe/H], [X/Fe]) space (Tolstoy et al. 2009). By obtaining spectroscopic measurements of various elemental abundances, we may be able to find real *r*-II clusters that are remnants of dwarf galaxies.

An issue of our greedy optimistic clustering method is that stars with poor parallax (or distance) measurements can contaminate real clusters. This kind of contamination effect

can be reduced by improving the distance estimates of the *r*-II stars, by using parallax from future data releases of Gaia or by using better photometric distances.

7.6. Caveats in our Analysis

7.6.1. Assumptions on the Gravitational Potential

In this paper, we performed a clustering analysis of *r*-II stars in the orbital action space. In computing the orbital action $\boldsymbol{J}(\boldsymbol{x}, \boldsymbol{v})$ from the observed position–velocity data $(\boldsymbol{x}, \boldsymbol{v})$, we assumed a gravitational potential model of the Milky Way $\Phi(\boldsymbol{x})$ and the solar position and velocity with respect to the Galactic Center. Therefore, our clustering analysis is necessarily affected by any bias on these assumptions. For example, seven stars travel beyond $r > 30$ kpc (see $r_{\rm apo}$ in Table 3), where the perturbation from the Large Magellanic Cloud may be important (Besla et al. 2010; Erkal et al. 2019, 2021; Garavito-Camargo et al. 2019; Koposov et al. 2019; Conroy et al. 2021; Petersen & Peñarrubia 2021; Shipp et al. 2021). Also, some groups of stars that pass near the bulge region with prograde motion might be affected by the rotating potential of the Galactic bar (Hattori et al. 2016; Price-Whelan et al. 2016). Although these complexities are not included in our study, we believe that they do not seriously affect our results, especially the result on Tier 1 clusters because we validated our results with chemical abundance information that is independent of the dynamical analysis in this paper.

7.6.2. Assumptions on the Distribution of the Orbital Action of r-II Stars

We assume that the distribution of the *r*-II stars in the $\boldsymbol{J}$ space is described by a mixture of isotropic Gaussian distributions with identical dispersion σ_J^2, as expressed in Equation (10). This is a natural assumption if all the *r*-II stars in our catalog originate from small dwarf galaxies such as UFDs, but in reality, it is uncertain whether this assumption is valid. For example, if some fraction of *r*-II stars originates from a disrupted large dwarf galaxy (such as Gaia-Sausage/Enceladus), we may expect diffuse and smooth background of *r*-II stars not associated with small clumps. Indeed, there are some indications that large dwarf galaxies do include *r*-enhanced stars (Matsuno et al. 2021 for Gaia-Sausage/Enceladus; Reichert et al. 2021 for Fornax dwarf galaxy; see also Xing et al. 2019, who discuss the origin of an *r*-II star that exhibits low [Mg/Fe]). Because the fraction of *r*-II stars in large dwarf galaxies is expected to be low (Hirai et al. 2022), we believe it is justifiable to apply our method to *r*-II stars. However, since we did not analyze the effect of diffuse and smooth background of *r*-II stars in our mock data analysis (Okuno & Hattori 2022), it is unclear how such a background population may affect our results (Brauer et al. 2022). This issue may be the subject of future studies.

7.6.3. Very Metal-poor r-II Stars in Our Sample

Our analysis is motivated by the discovery of an Eu-rich UFD, Reticulum II. Given that known members of surviving UFDs typically have $[\mathrm{Fe/H}] < -2$, it may be interesting to see how our results are affected if we preselect very metal-poor *r*-II stars with $[\mathrm{Fe/H}] < -2$ before performing the clustering analysis. We did an additional analysis in this direction, as described in Appendix G. We found that the clustering results are similar to our fiducial result. With this simple [Fe/H] selection, one may fail to discover some interesting clusters, such as H22:DTC-2 (which corresponds to group B in Roederer et al. 2018a), whose mean metallicity is $\langle[\mathrm{Fe/H}]\rangle = -1.65$. Thus, we assert that using the entire sample of *r*-II stars available is more informative than using only very metal-poor *r*-II stars.

8. Conclusion

In this paper, we extended the work in Roederer et al. (2018a) and performed a clustering analysis of $N = 161$ *r*-II stars ($[\mathrm{Eu/Fe}] \geqslant 0.7$ and $[\mathrm{Ba/Fe}] < 0$) in the orbital action ($\boldsymbol{J}$) space. Our data set is the largest catalog of *r*-II stars, which includes *r*-II stars discovered before the end of 2020 (see Tables 2 and 3). For all the sample stars, we have astrometric data from Gaia EDR3, and therefore our catalog supersedes the catalog in Roederer et al. (2018a) in which Gaia DR2 data were used. To our updated catalog, we applied a newly developed *greedy optimistic clustering method* (Okuno & Hattori 2022), which allows us to analyze not only stars with good observational data but also stars with poor data. As a result, we were able to analyze all the *r*-II stars in our catalog, without discarding stars with large observational uncertainty.

This paper is summarized as follows:

1. By using the GMMM equipped with the greedy optimistic clustering algorithm, we performed the clustering analysis in the orbital action space. The orbital action distribution of $N = 161$ *r*-II stars can be described by $K = 30$ clusters with intrinsic internal dispersion of $\sigma_J = 100$ kpc km s^{-1} (see Table 1 and Figure 3).
2. Groups A–H discovered in Roederer et al. (2018a) are recovered in our analysis (see Table 1). Specifically, groups B, C, D, and G are identified as separate clusters in our analysis. Groups A and F are identified as a single (big) cluster in our analysis. Groups E and H (and a star in group F) are identified as a single (big) cluster in our analysis (see Section 6.4). For all groups in Roederer et al. (2018a), we found additional member stars (see Table 2).
3. Among the 26 clusters with $N_{\mathrm{member},k} \geqslant 2$ member stars, 13 clusters have metallicity dispersion of $\sigma_{[\mathrm{Fe/H}]} < 0.35$, which is equivalent to or smaller than the dispersion in the *r*-enhanced UFD, Reticulum II. This result indicates that many of the field *r*-II stars may have originated from disrupted dwarf galaxies (see Section 7.1).
4. We validated our clustering result by using the chemical abundance data, which we did not use in the clustering analysis. Based on the tightness of the distribution of [Fe/H] and [Eu/H], we categorized our clusters into five categories: Tier 1 clusters (for which we have the highest confidence), Tiers 2, 3, and 4 clusters (with decreasing confidence), and single member clusters (see Sections 7.1 and 7.2).
5. We found six *r*-II clusters (H22:DTC-1, 2, 3, 4, 5, and 9; Tier 1 clusters) with tight distributions in [Fe/H], [Eu/H], [Mg/Fe], and [Ca/Fe] (see Figures 4 and 5). Because the chemical information is not used in the clustering analysis, the chemical homogeneity of these clusters suggests that these six clusters are likely to be genuine

clusters. Given that the member stars of Tier 1 clusters are apparently completely phase mixed (see Figure 6), we interpret Tier 1 clusters as the remnants of completely disrupted dwarf galaxies that merged with the ancient Milky Way (see Section 7.2.1). However, more data are needed to confirm this scenario (see Section 7.5).

6. The cluster H22:DTC-1 is a newly discovered cluster with $N_{\mathrm{member},k} = 9$ member stars. This cluster has the tightest distribution in [Fe/H] in terms of the quantities $q_{\mathrm{[Fe/H]}}$ introduced in Section 7.1. Two of the member stars are among the 35 *r*-II stars analyzed in Roederer et al. (2018a) and regarded by that study as *r*-II stars not associated with any groups. The fact that these two stars (as well as the other seven member stars) are successfully considered as a single cluster highlights the advantage of using the greedy optimistic clustering method (see Section 7.2.1).
7. Apart from a Tier 1 cluster H22:DTC-1, we identified many new *r*-II clusters that had not been identified in previous studies. All nine clusters in Tiers 2 and 3 are newly discovered (see Appendix C).
8. We found four *r*-II clusters (H22:DTC-27, 28, 29, and 30) with a single member star. Two of these clusters, H22:DTC-29 and 30, are the most metal-poor *r*-II clusters characterized by a highly eccentric orbit with $ecc \simeq 0.88$ and $r_{\mathrm{apo}} > 90$ kpc (see Section 7.2.3).
9. In the hierarchical galaxy formation paradigm, some small stellar systems, such as dwarf galaxies or globular clusters, merge together as a group. In accordance with this scenario, it has been claimed that some stellar streams, globular clusters, and dwarf galaxies in the Milky Way are clustered in phase space (Bonaca et al. 2021; Malhan et al. 2022). Recently, Malhan et al. (2022) reported that there are six big merger groups. We checked the 30 *r*-II clusters obtained in this study and found that eight *r*-II clusters are associated with four of the merger groups: Gaia-Sausage/Enceladus, Arjuna/Sequoia/I'itoi, LMS-1/Wukong, and Pontus (see Section 7.3 and Figure 7).
10. Two Tier 1 clusters H22:DTC-1 and 9 are very metal-poor ([Fe/H] $\simeq -2.8$), which indicates that their progenitor systems were low-mass UFD-like systems with a stellar mass of $M_* \sim 10^4\ M_\odot$ according to the mass–metallicity relationship (Kirby et al. 2013; Naidu et al. 2022). Intriguingly, these two clusters have similar chemistry and orbits. They may be the remnants of two *r*-enhanced dwarf galaxies that merged with the Milky Way as a group. If these clusters are associated, they may constitute a new merger group that is separate from the previously known merger groups found in Bonaca et al. (2021) and Malhan et al. (2022) (see Section 7.4).

K.H. thanks Hideitsu Hino for the useful suggestions on the split-and-merge EM algorithm, and Yukito Iba for comments on the mock data analyses. K.H. thanks Kazuhei Kikuchi for encouraging this project. K.H. is supported by JSPS KAKENHI grant Nos. JP21K13965 and JP21H00053. A.O. is supported by JSPS KAKENHI grant No. JP21K17718 and JST CREST No. JPMJCR21N3. I.U.R. is supported by the U.S. National Science Foundation under grant Nos. PHY 14-30152 (Physics Frontier Center/JINA-CEE), AST 1815403/1815767, and AST 2205847, as well as the NASA Astrophysics Data Analysis Program under grant No. 80NSSC21K0627. This work has made use of data from the European Space Agency (ESA) mission Gaia (https://www.cosmos.esa.int/gaia), processed by the Gaia Data Processing and Analysis Consortium (DPAC, https://www.cosmos.esa.int/web/gaia/dpac/consortium). Funding for the DPAC has been provided by national institutions, in particular, the institutions participating in the Gaia Multilateral Agreement.

Facility: Gaia.

Software: AGAMA (Vasiliev 2019), matplotlib (Hunter 2007), NumPy (van der Walt et al. 2011), SciPy (Jones et al. 2001).

Appendix A
A Demonstration of the Greedy Optimistic Clustering

To perform a clustering analysis for a noisy data set, we introduce the greedy optimistic clustering method (Okuno & Hattori 2022). In the greedy optimistic clustering, we simultaneously estimate both (i) the centroids of the clusters and (ii) the *true* orbital action $\boldsymbol{J}_i^{\mathrm{true}}$. By contrast, in the conventional clustering methods, we are mainly interested in estimating the centroids of the clusters by using the point estimate of the orbital action $\widehat{\boldsymbol{J}}_i$. Here, we explain how these clustering methods work differently. As a demonstration, we focus on the clustering of three *r*-II stars under the assumption that these stars are members of a single cluster. Figure 8 shows the distribution of $\boldsymbol{J}$ for stars A, B, and C. Stars A, B, and C respectively have $\varpi/\sigma_\varpi = 16.63$, 11.18, and 26.83; and $\Delta J/(\mathrm{kpc\ km\ s^{-1}}) = 126$, 353, and 138. The names of these stars are given in the caption of Figure 8. These stars are taken from the cluster H22:DTC-1, which we found in our main analysis of this paper. Apart from this fact, the content of this appendix is independent of the main analysis of this paper.

A.1. Conventional Clustering Methods

In the left-hand panels of Figure 8, the point estimate $\widehat{\boldsymbol{J}}_i$ ($i \in \{A, B, C\}$) of each star (big black symbol) is derived from the point estimate of the observables. Under the assumption that stars A, B, and C are associated with one cluster, conventional clustering methods find the centroid in the *middle* of these three point estimates. (The definition of the *middle* depends on the clustering method.)

The small gray symbols in the left-hand panels of Figure 8 represent the uncertainty set of $\boldsymbol{J}$ for these stars. We see that the distribution of the uncertainty set for each star is highly elongated, despite the relatively small parallax uncertainty ($\varpi/\sigma_\varpi > 10$). The elongated shape arises from the fact that the parallax uncertainty dominates the uncertainty in $\boldsymbol{J}$, as explained in Section 3. For example, if we adopt a small value of ϖ for star B, both J_r and J_z become large, and vice versa.

As we can see from the uncertainty set, the point estimate is just one of many possibilities. Even when the parallax uncertainty is small, the point estimate may be very different from the true orbital action. Because conventional clustering methods use the point estimate $\widehat{\boldsymbol{J}}_i$, conventional clustering methods may fail to work when the observational uncertainty is not negligible.

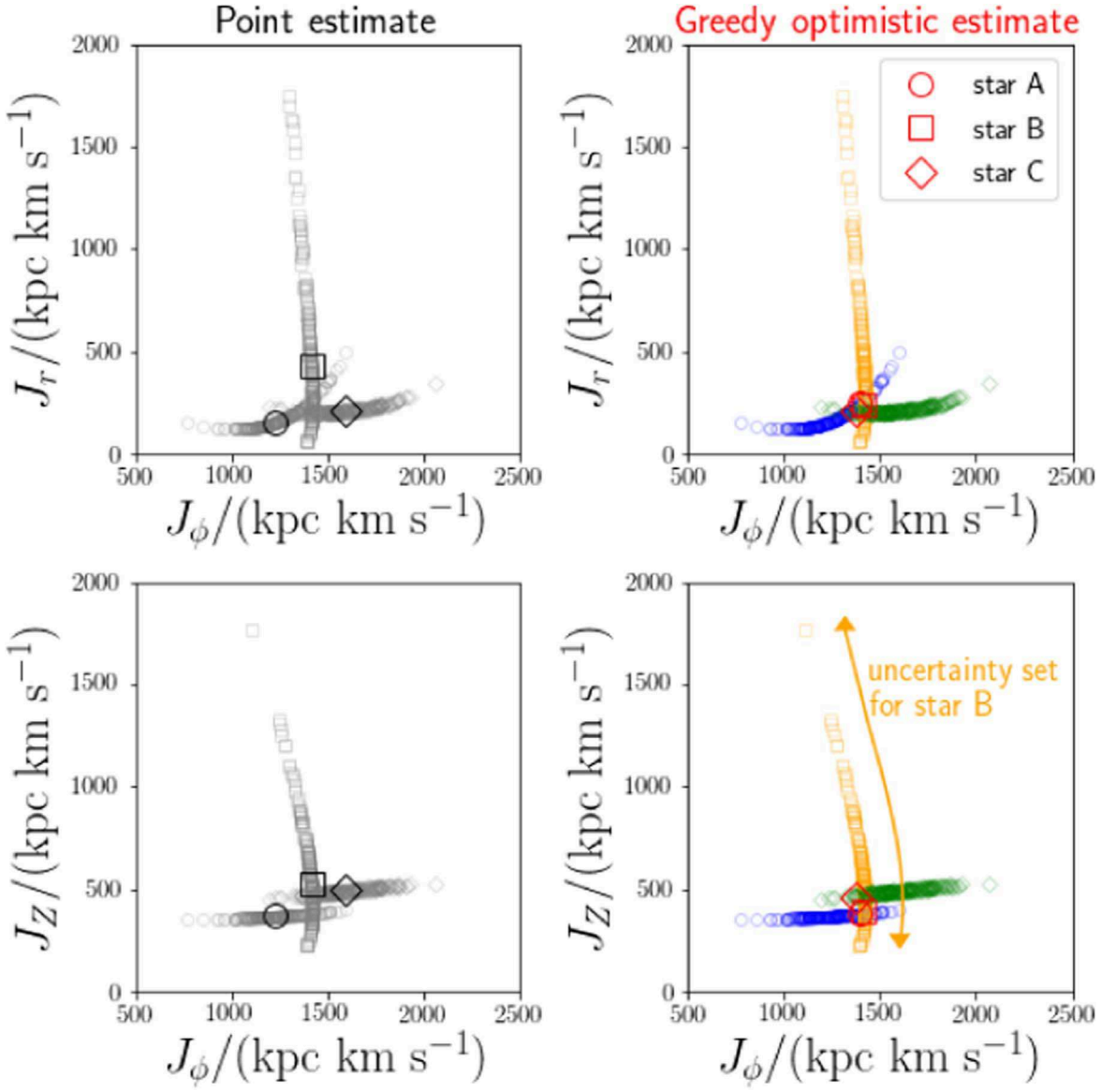

Figure 8. The distribution of the orbital action for stars A (HE 1523-0901), B (RAVE J203843.2-002333), and C (2MASS J09544277+5246414), which are taken from the cluster H22:DTC-1 in our main analysis. (Left panels): the big black symbols are the point estimate $\widehat{\boldsymbol{J}}_i$ ($i \in \{A, B, C\}$). The small gray symbols represent the uncertainty set for each star, which are shown for reference. (Right panels): the big red symbols represent the greedy optimistic estimate $\boldsymbol{J}_{i,\beta_i}$. The small colored symbols represent the uncertainty set for each star. The uncertainty set for star B is marked to illustrate its banana-shaped distribution. We see that the distribution of $(\boldsymbol{J}_{A,\beta_A}, \boldsymbol{J}_{B,\beta_B}, \boldsymbol{J}_{C,\beta_C})$ is more condensed than that of $(\widehat{\boldsymbol{J}}_A, \widehat{\boldsymbol{J}}_B, \widehat{\boldsymbol{J}}_C)$.

A.2. Greedy Optimistic Clustering Method

With the greedy optimistic clustering method, we estimate the *true* orbital action $\boldsymbol{J}_i^{\mathrm{true}}$ under some assumptions and then perform a clustering analysis. Because the estimation of $\boldsymbol{J}_i^{\mathrm{true}}$ is essential in this clustering method, we demonstrate how we estimate $\boldsymbol{J}_i^{\mathrm{true}}$ by using the example case in Figure 8.

In the right-hand panels of Figure 8, the uncertainty sets of $\boldsymbol{J}$ are shown with small colored symbols. In the greedy optimistic clustering, we assume that the true orbital action $\boldsymbol{J}_i^{\mathrm{true}}$ of star i is very close to one of the M instances (realizations) $\{\boldsymbol{J}_{i,j}\}$ in the uncertainty set of that star. In other words, we assume that one of the M^3 combinations of $\{(\boldsymbol{J}_{A,j_A}, \boldsymbol{J}_{B,j_B}, \boldsymbol{J}_{C,j_C})\}$ is very close to the true orbital actions of these stars $(\boldsymbol{J}_A^{\mathrm{true}}, \boldsymbol{J}_B^{\mathrm{true}}, \boldsymbol{J}_C^{\mathrm{true}})$. In addition, we *optimistically* assume that the true orbital actions $(\boldsymbol{J}_A^{\mathrm{true}}, \boldsymbol{J}_B^{\mathrm{true}}, \boldsymbol{J}_C^{\mathrm{true}})$ are highly clustered in the $\boldsymbol{J}$ space. Under these assumptions, we perform a *greedy* search for the best combination. As a demonstration, among M^3 combinations of $\{(\boldsymbol{J}_{A,j_A}, \boldsymbol{J}_{B,j_B}, \boldsymbol{J}_{C,j_C})\}$, we find the best combination $(\boldsymbol{J}_{A,\beta_A}, \boldsymbol{J}_{B,\beta_B}, \boldsymbol{J}_{C,\beta_C})$ that achieves the minimum internal dispersion in $\boldsymbol{J}$ with a brute-force approach. The orbital action estimated through this procedure is the *greedy optimistic estimate* of the orbital action. The greedy optimistic estimates are shown by the big red symbols in the right-hand panels of Figure 8. By comparing $\boldsymbol{J}_{i,\beta_i}$ (right-hand panels) with $\widehat{\boldsymbol{J}}_i$ (left-hand panels), we can visually confirm that the greedy optimistic estimates are more condensed. Indeed, the dispersion of $\{\boldsymbol{J}_{i,\beta_i}\}$ is only $41\,\mathrm{kpc\,km\,s^{-1}}$, while the dispersion of $\{\widehat{\boldsymbol{J}}_i\}$ is as large as $203\,\mathrm{kpc\,km\,s^{-1}}$.

The most important assumption in the greedy optimistic clustering method is the assumption that the true orbital actions are highly clustered in $\boldsymbol{J}$ space. Because there is no guarantee

that this optimistic assumption is valid, it is important to validate our clustering results with an independent set of data. This is why, in the main analysis of this paper, we check the chemical information for each cluster.

Appendix B
A Comment on the Computational Cost of the GOEM Algorithm

In this paper, we use the GOEM algorithm to find the best solution for the greedy optimistic GMM. Here, we comment on the computational cost of this algorithm.

If we had an infinite amount of computing resources, we could use the following steps to find the best solution. (1) We would try M^N combinations of $\{\beta_i\}$. (2) We would apply the conventional GMM to each of the M^N configurations of the data points. For each configuration, we would find the best parameters (i.e., the centroids and weights) that maximize the object function in Equation (14). (3) We would find the best configurations and parameters that maximize the object function in Equation (14). Obviously, such a brute-force strategy is computationally expensive because we would need to perform GMM fitting for $M^N \sim 10^{322}$ times for our case with $(M, N) = (101, 161)$. (In Appendix A, we use a brute-force strategy because it is easier to understand.) Fortunately, in the mock data analysis in Okuno & Hattori (2022), we typically need ∼20 iterations of the GO, E, and M steps to reach a good solution. This computational cost is obviously much smaller than a brute-force approach.

Appendix C
Clusters in Tiers 2, 3, and 4

In the main body of this paper, we showed the distribution of orbital action and chemical abundances of Tier 1 clusters, for which we have the highest confidence in our results. Here, we show the distribution of stars for other clusters that are worth mentioning.

C.1. Tier 2: Five Interesting Clusters

Apart from Tier 1 clusters, there are five clusters that satisfy both $q_{\rm [Fe/H]} < 25\%$ and $q_{\rm [Eu/H]} < 25\%$. We label these clusters as Tier 2 clusters, which include clusters with H22:DTC-7, 10, 11, 12, and 13. All of these clusters are newly discovered. Figure 9 shows that both [Fe/H] and [Eu/H] have moderately tight distributions (see Figure 9).

Tier 2 cluster H22:DTC-7. This cluster is one of the lowest metallicity and highly prograde clusters with $\langle {\rm [Fe/H]} \rangle = -2.83$ and $\langle {\rm [Eu/H]} \rangle = -1.82$. It contains only $N_{{\rm member},k} = 2$ member stars, but their [Fe/H] and [Eu/H] are very close to each other.

Tier 2 cluster H22:DTC-10. This cluster has $N_{{\rm member},k} = 4$. Apart from the most metal-poor member, BPS CS 29491-069, the other three stars have a poor parallax measurement with $\varpi/\sigma_\varpi < 5$ (see Table 2). This is a clear example that our optimistic clustering can find a candidate group even if the observational error is large.

Tier 2 cluster H22:DTC-11. This cluster has $N_{{\rm member},k} = 2$. Its mean metallicity is the highest among the 30 clusters, with $\langle {\rm [Fe/H]} \rangle = -1.39$.

Tier 2 cluster H22:DTC-12. This cluster has $N_{{\rm member},k} = 2$ with a shell-like orbit characterized by small J_r and large J_z.

Tier 2 cluster H22:DTC-13. This cluster has $N_{{\rm member},k} = 6$. It has the smallest $||\langle J_\phi \rangle|| = 47$ kpc km s^{-1}, which corresponds to highly radial orbits.

C.2. Tier 3: Four Promising Clusters

Apart from Tier 1 and 2 clusters, there are four clusters that satisfy either $q_{\rm [Fe/H]} < 25\%$ or $q_{\rm [Eu/H]} < 25\%$. We label these clusters as Tier 3 clusters, which include clusters with H22:DTC-6, 8, 14, and 21. All of the Tier 3 clusters are newly found and have $N_{{\rm member},k} = 2$ member stars. The distribution of stars in the action and chemistry space is shown in Figure 10.

Tier 3 cluster H22:DTC-6. This group is characterized by a prograde, nearly circular orbit with $\langle J_\phi \rangle = -2504$ kpc km s^{-1}, corresponding to a guiding center radius of $R \sim 10$ kpc.

Tier 3 cluster H22:DTC-8. This group is characterized by a highly radial orbit with $||\langle J_\phi \rangle|| = 163$ kpc km s^{-1}.

Tier 3 cluster H22:DTC-14. One of the member stars of this cluster is 2MASS J15213995-3538094, which has the most enhanced value of [Eu/Fe] = +2.23 in our catalog (Cain et al. 2020).

Tier 3 cluster H22:DTC-21. This cluster is characterized by a relatively large dispersion in [Fe/H], $\sigma_{\rm [Fe/H]} = 0.43$ but has a very small dispersion in [Eu/H], $\sigma_{\rm [Eu/H]} = 0.01$.

C.3. Tier 4: Three Potentially Promising Clusters

There are three additional clusters (H22:DTC-15, 17, and 24) that are worth attention. We label them as Tier 4. The distribution of stars in the action and chemistry space is shown in Figure 11.

Tier 4 cluster H22:DTC-15. This group has $N_{{\rm member},k} = 18$ member stars. Its relatively large dispersion in [Fe/H] is mostly due to a single outlier, G210-33, which has [Fe/H] = −1.08. If we manually exclude this star, the standard deviations in [Fe/H] and [Eu/H] are 0.40 and 0.41, respectively. The corresponding percentile values are $q_{\rm [Fe/H]} = 4.88$ and $q_{\rm [Eu/H]} = 7.90$, respectively. Therefore, without one outlier star, this cluster could be classified as a Tier 1 cluster. Even after removing G210-33, this cluster contains all the stars in groups E and H and a star in group F in Roederer et al. (2018a).

Tier 4 cluster H22:DTC-17. This is a cluster of size $N_{{\rm member},k} = 4$. This cluster includes Gaia DR2 6412626 111276193920 (also known as Indus_13), which is a member of the Indus stream (Hansen et al. 2021). The remaining three *r*-II stars in this group have very different orbital phases, suggesting that they are unlikely to be members of the Indus stream. These *r*-II stars might have originated from different dwarf galaxies that accreted to the Milky Way together.

Tier 4 cluster H22:DTC-24. This group has $N_{{\rm member},k} = 14$ member stars. As can be seen in Figure 11 (right column), these 14 stars show an L-shaped distribution in the [Fe/H]–[Eu/Fe] diagram. The seven stars above [Fe/H] = −2.1 have [Eu/Fe] ≃ 0.7, which is the lower boundary of our sample selection. If we manually select stars below [Fe/H] = −2.1, the standard deviations in [Fe/H] and [Eu/H] are 0.14 and 0.20, respectively. The corresponding percentile values are $q_{\rm [Fe/H]} = 0.16$ and $q_{\rm [Eu/H]} = 1.18$, respectively. Therefore, with this (arbitrary) manual selection of seven stars, this cluster could be classified as a Tier 1 cluster.

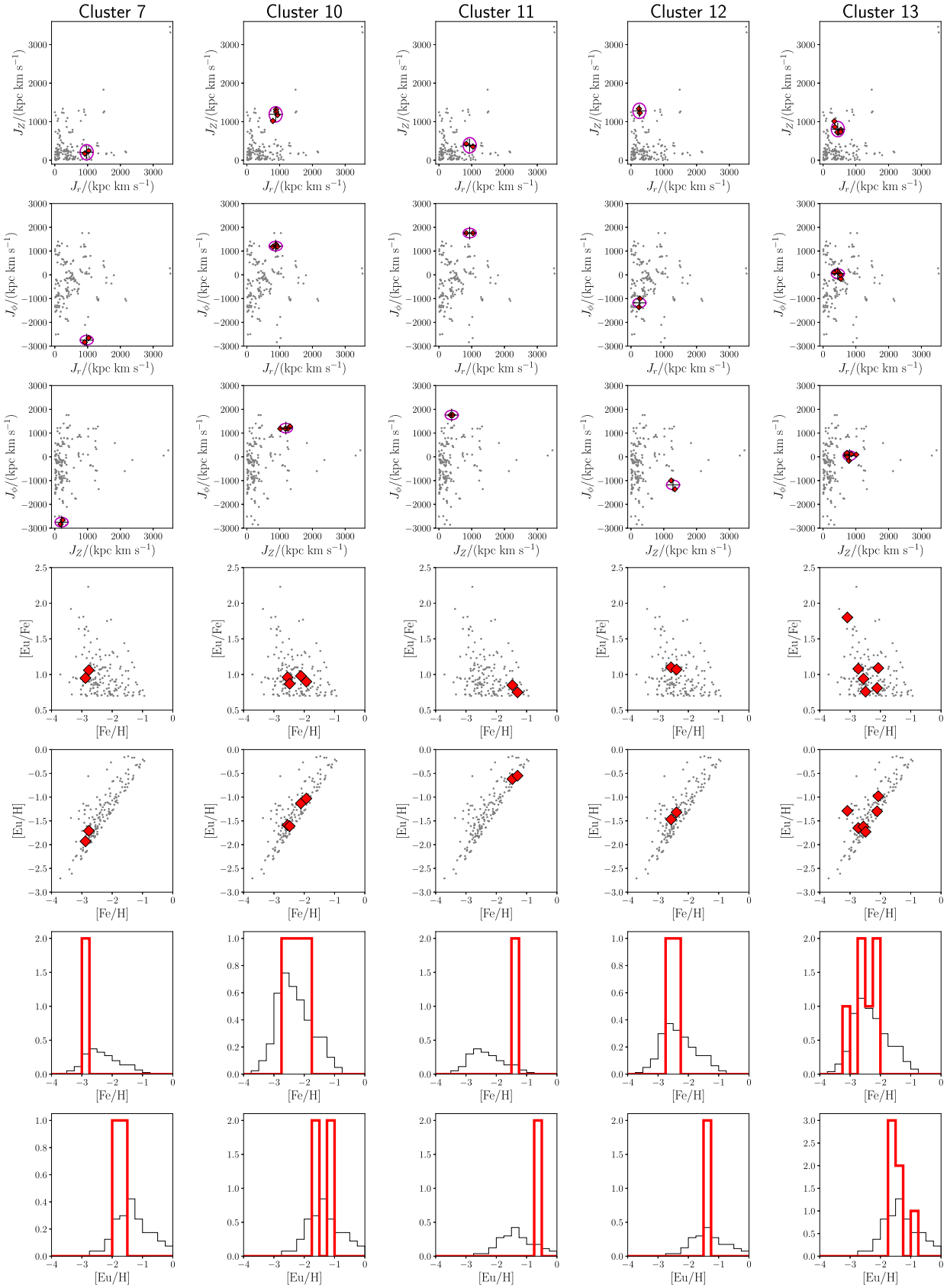

Figure 9. The same as Figure 4, but for Tier 2 clusters (H22:DTC-7, 10, 11, 12, and 13).

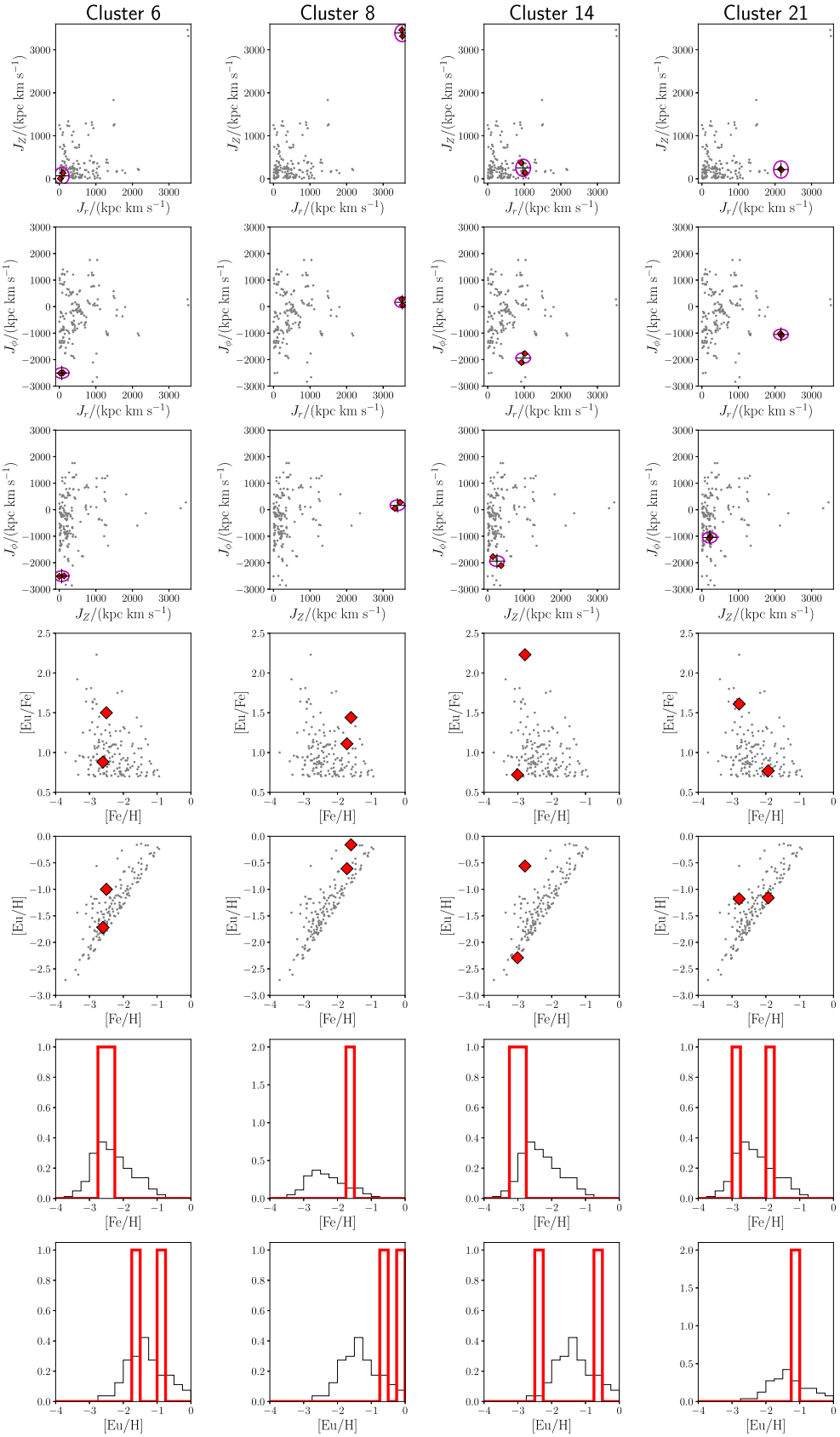

Figure 10. The same as Figure 4, but for Tier 3 clusters (H22:DTC-6, 8, 14, and 21).

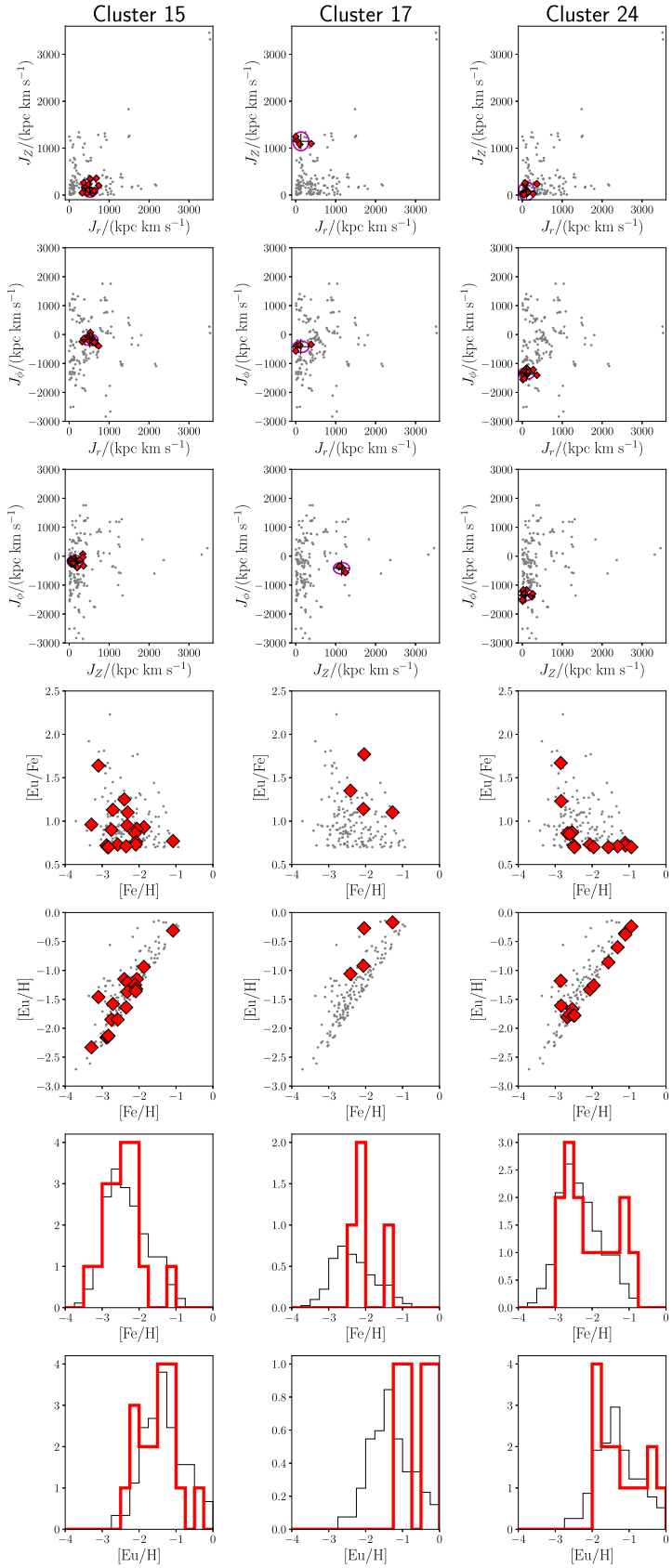

Figure 11. The same as Figure 4, but for Tier 4 clusters (H22:DTC-15, 17, and 24).

Appendix D
Member Stars of All the Clusters

Table 2 lists the member stars of all the $K = 30$ clusters and the basic chemical and dynamical properties of the member stars. Table 3 lists additional kinematical and orbital information on the *r*-II stars. See Section 6.3 for the description of these tables.

Appendix E
A Comment on the "Edge Effect" of the Greedy Optimistic Solution

An alert reader may notice that in the top row in Figure 3, the greedy optimistic estimates of some stars are located near the edge of their uncertainty sets. To confirm the validity of our result, we conduct an additional test on our fiducial solution. In this test, we use $K = 30$ centroids $\langle \boldsymbol{J} \rangle_k$ ($k = 1, \cdots, K$) obtained from the fiducial analysis and the as-observed orbital action of $N = 161$ stars $\boldsymbol{J}_i \equiv \boldsymbol{J}_{i,50}$ ($i = 1, \cdots, N$). For each star i, we find the nearest centroid k' such that $||\boldsymbol{J}_i - \langle \boldsymbol{J} \rangle_{k'}||$ is minimized. For each star i, we compare k' and the value of k in our fiducial analysis. As a result, we find that (i) 137 stars among 161 stars (85%) satisfy $k' = k$; and that (ii) 53 stars among 59 stars in Tier 1 clusters (90%) satisfy $k' = k$. These results indicate that, in most cases, the choice of the instance of the uncertainty set is not critical in assigning the cluster. As demonstrated in Appendix A, our algorithm tries to shrink the cluster in the action space, and depending on the configuration of the uncertainty set and the centroid, the edge of the uncertainty set is chosen in our method.

Appendix F
Clustering Analysis Using Standard GMM and High-quality Data

The originality of this paper is that we use a new clustering algorithm, namely, the greedy optimistic GMM, in finding candidates for clusters in the $\boldsymbol{J}$ space. Although our approach has an advantage in that stars with low-quality kinematic data can be used, it has a disadvantage in that stars with low-quality data might contaminate clusters. In this regard, the resultant clusters in our fiducial analysis might be contaminated by stars that are not supposed to be true member stars. In the main text of this paper, we carefully analyze the chemical information of the member stars to conclude that Tier 1 clusters are more plausible candidates for disrupted dwarf galaxies than other *r*-II clusters.

To further examine the validity of our fiducial result, here we perform an additional clustering analysis using $N = 119$ *r*-II stars with high-quality astrometric data defined by `parallax_over_error` > 10. In this analysis, we fix $\sigma_J = 100\,\mathrm{kpc\,km\,s^{-1}}$ and $K = 30$ as in our fiducial analysis. Also, we use the standard GMM instead of the greedy optimistic GMM.

In the fiducial result, we have $K = 30$ clusters consisting of $N = 161$ stars. Among these 30 clusters, we have (i) 11 clusters in which all the member stars have high-quality kinematic data (`parallax_over_error` > 10); (ii) two clusters in which all the member stars have low-quality kinematic data (`parallax_over_error` < 10); and (iii) 17 clusters that include both stars with high-quality data and stars with low-quality data. From the fiducial result, we discard the two clusters in item (ii). Also, we discard member stars with `parallax_over_error` < 10 from the 17 clusters in item (iii). As a result, we end up with $K = 28$ clusters consisting of $N = 119$ stars with `parallax_over_error` > 10.

To investigate the similarity between the two sets of clusters mentioned above, namely, the 30 clusters described in the second paragraph (i.e., an additional clustering result using stars with high-quality data) and 28 clusters described in the third paragraph (i.e., a subset of the fiducial analysis), we compute four similarity indices. We find that the purity is 0.883, The normalized mutual information is 0.888, the Rand index is 0.968, and the F-measure is 0.846. These indices are close to unity, which means that these two sets of clusters are similar to each other.

We also investigate how the member stars of Tier 1 clusters in the fiducial result are classified in our additional analysis. As a result, most member stars in each Tier 1 cluster are successfully identified as a single cluster. This result indicates that, as long as we use high-quality data only, Tier 1 clusters can be identifiable independent of the adopted clustering method (i.e., the standard GMM or greedy optimistic GMM), supporting the plausibility of Tier 1 clusters. The details of individual Tier 1 clusters are summarized below.

(H22:DTC-1). Among the nine member stars, all the stars satisfy `parallax_over_error` >10. Among them, seven stars (except for J14592981-3852558 and BPS CS 22896-154) are found in the same cluster. This cluster (which is a subset of H22:DTC-1) is chemically homogeneous, with $\sigma_{[\mathrm{Fe/H}]} = 0.20$ and $\sigma_{[\mathrm{Eu/H}]} = 0.35$. These quantities correspond to $q_{[\mathrm{Fe/H}]} = 0.9$ and $q_{[\mathrm{Eu/H}]} = 16.8$, respectively.

(H22:DTC-2). Among the nine member stars, eight stars satisfy `parallax_over_error` > 10 (except for SMSS J175046.30-425506.9, which happens to be the only very metal-poor member star). These eight stars are found in the same cluster. This cluster (which is a subset of H22:DTC-2 and a superset of group D in Roederer et al. 2018a) is chemically homogeneous, with $\sigma_{[\mathrm{Fe/H}]} = 0.17$ and $\sigma_{[\mathrm{Eu/H}]} = 0.22$. These quantities correspond to $q_{[\mathrm{Fe/H}]} = 0.2$ and $q_{[\mathrm{Eu/H}]} = 1.1$, respectively.

(H22:DTC-3). Among the 18 member stars, all stars satisfy `parallax_over_error` >10. These stars are separated into three clusters. The biggest cluster contains 10 member stars (2MASS J00512646-1053170, HE 0430-4901, 2MASS J22562536-0719562, J03422816-6500355, BPS CS 22958-052, SDSS J004305.27+194859.20, J01425445-0904162, HD 221170, J12044314-2911051, and 2MASS J15271353-2336177). This cluster (which is a subset of H22:DTC-3) is chemically homogeneous, with $\sigma_{[\mathrm{Fe/H}]} = 0.24$ and $\sigma_{[\mathrm{Eu/H}]} = 0.21$. These quantities correspond to $q_{[\mathrm{Fe/H}]} = 1.1$ and $q_{[\mathrm{Eu/H}]} = 1.4$, respectively.

(H22:DTC-4). Among the 12 member stars, eight stars satisfy `parallax_over_error` > 10. These eight stars are found in the same cluster. This cluster (which is a subset of H22:DTC-4) is chemically homogeneous, with $\sigma_{[\mathrm{Fe/H}]} = 0.27$ and $\sigma_{[\mathrm{Eu/H}]} = 0.18$. These quantities correspond to $q_{[\mathrm{Fe/H}]} = 2.5$ and $q_{[\mathrm{Eu/H}]} = 0.5$, respectively.

(H22:DTC-5). Among the five member stars, three stars satisfy `parallax_over_error` > 10. Among these three stars, two stars (2MASS J02462013-1518419 and BPS CS 22953-003) are found in a single cluster. This cluster (which is a subset of H22:DTC-5) has $\sigma_{[\mathrm{Fe/H}]} = 0.065$ and $\sigma_{[\mathrm{Eu/H}]} = 0.27$. These quantities correspond to $q_{[\mathrm{Fe/H}]} = 13.4$ and $q_{[\mathrm{Eu/H}]} = 51.6$, respectively.

(H22:DTC-9). Among the six member stars, four stars satisfy `parallax_over_error` > 10. Among these four stars, three stars (SDSS J235718.91-005247.8, BPS CS 31082-001, and SMSS J051008.62-372019.8) are found in a single cluster. This cluster (which is a subset of H22:DTC-9) has $\sigma_{[\mathrm{Fe/H}]} = 0.19$, and $\sigma_{[\mathrm{Eu/H}]} = 0.43$. These quantities correspond to $q_{[\mathrm{Fe/H}]} = 15.7$ and $q_{[\mathrm{Eu/H}]} = 59.8$, respectively.

Appendix G
Clustering Analysis Using Stars with [Fe/H] < -2

In our *r*-II star catalog, we have $N = 118$ very metal-poor stars with [Fe/H] < -2, similar to most stars in UFDs known to date (including Reticulum II). Motivated by the observed chemical properties of UFDs, we perform an additional clustering analysis using these $N = 118$ *r*-II stars. We fix $\lambda = 0$ and $\sigma_J = 100\,\mathrm{kpc\,km\,s^{-1}}$ as in our fiducial analysis and set $K = 25$.

In the fiducial result, we have $K = 30$ clusters consisting of $N = 161$ stars. Among these 30 clusters, we have (i) four clusters in which all the member stars are metal-rich ([Fe/H] $\geqslant -2$), (ii) 12 clusters in which all the member stars are very metal-poor ([Fe/H] < -2), and (iii) 14 clusters which include both very metal-poor stars and metal-rich stars. From the fiducial result, we discard four metal-rich clusters in item (i). Also, we discard metal-rich member stars from 14 clusters in item (iii). As a result, we end up with $K = 26$ clusters consisting of $N = 118$ very metal-poor stars.

To investigate the similarity between the two sets of clusters mentioned above, namely, the 25 clusters described in the first paragraph (i.e., an additional clustering result using very metal-poor stars only) and the 26 clusters described in the second paragraph (i.e., a subset of the fiducial analysis), we compute four similarity indices. We find that the purity is 0.839, the normalized mutual information is 0.868, the Rand index is 0.966, and the F-measure is 0.815. These indices are close to unity, which means that these two sets of clusters are similar to each other.

We also investigate how the member stars of Tier 1 clusters in the fiducial result (except for H22:DTC-2 because only one out of its nine member stars is very metal-poor) are classified in our additional analysis. H22:DTC-1 is divided into two separate clusters. All the very metal-poor member stars in H22:DTC-3 are found in a single cluster. H22:DTC-4 is divided into two separate clusters. All the very metal-poor member stars in H22:DTC-5 are found in a single cluster. Five out of six member stars in H22:DTC-9 are found in a single cluster. These results indicate that the preselection of the sample by [Fe/H] does not drastically affect the clustering results of Tier 1 clusters, while some Tier 1 clusters (H22:DTC-3 and H22:DTC-9) are less sensitive to the preselection than others.

Appendix H
Analysis of Non-*r*-II Stars

In the fiducial analysis, we find that many dynamically identified *r*-II clusters have relatively tight distribution in [Fe/H]. Here, we investigate whether or not our result is statistically significant by performing the same analysis for non-*r*-II stars.

For this test, we carefully construct a sample of $N = 161$ non-*r*-II stars such that its [Fe/H] histogram (with a bin size of 0.25 dex) is almost identical to that of our *r*-II sample. For this sample, [Fe/H] is determined from high-resolution spectroscopy, either from Subaru observation (Li et al. 2022a) or Gaia-ESO survey DR5.0 (Gilmore et al. 2012; https://www.gaia-eso.eu/data-products/public-data-releases).

We analyze this sample in the same manner as our fiducial analysis with $K = 30$. We note that we do not have [Eu/H] or [Eu/Fe] measurements for most of our non-*r*-II stars partly because Eu abundance is difficult to measure for most non-*r*-II stars. Thus, we compare the tightness in the [Fe/H] distribution for clusters of *r*-II stars and those of non-*r*-II stars. As a result, we find that

1. The non-*r*-II sample has three clusters with $\sigma_{[\mathrm{Fe/H}]} < 0.35$, while our *r*-II sample has 14 clusters;
2. The non-*r*-II sample has 0 clusters with $q_{[\mathrm{Fe/H}]} < 5$, while our *r*-II sample has five clusters; and
3. The non-*r*-II sample has four clusters with $q_{[\mathrm{Fe/H}]} < 15$, while our *r*-II sample has nine clusters.

We see that our *r*-II clusters have tighter [Fe/H] distributions than the corresponding clusters of non-*r*-II stars. In other words, *r*-II stars with similar orbits tend to have smaller [Fe/H] dispersion than normal stars with similar orbits do, supporting the main result in this paper.

ORCID iDs

Kohei Hattori https://orcid.org/0000-0001-6924-8862
Akifumi Okuno https://orcid.org/0000-0001-9621-8853
Ian U. Roederer https://orcid.org/0000-0001-5107-8930

References

Allen, D. M., Ryan, S. G., Rossi, S., Beers, T. C., & Tsangarides, S. A. 2012, A&A, 548, A34
Aoki, W., Beers, T. C., Honda, S., & Carollo, D. 2010, ApJL, 723, L201
Baeza, I., Fernández-Trincado, J. G., Villanova, S., et al. 2022, A&A, 662, A47
Bandyopadhyay, A., Sivarani, T., & Beers, T. C. 2020, ApJ, 899, 22
Barklem, P. S., Christlieb, N., Beers, T. C., et al. 2005, A&A, 439, 129
Beers, T. C., & Christlieb, N. 2005, ARA&A, 43, 531
Belokurov, V., Zucker, D. B., Evans, N. W., et al. 2006, ApJL, 642, L137
Besla, G., Kallivayalil, N., Hernquist, L., et al. 2010, ApJL, 721, L97
Bishop, C. M. 2006, Pattern Recognition and Machine Learning (Berlin: Springer)
Blumenthal, G. R., Faber, S. M., Primack, J. R., & Rees, M. J. 1984, Natur, 311, 517
Bonaca, A., Naidu, R. P., Conroy, C., et al. 2021, ApJL, 909, L26
Bovy, J., Hogg, D. W., & Roweis, S. T. 2011, AnApS, 5, 1657
Brauer, K., Andales, H. D., Ji, A. P., et al. 2022, ApJ, 937, 14
Bressan, A., Marigo, P., Girardi, L., et al. 2012, MNRAS, 427, 127
Buder, S., Lind, K., Ness, M. K., et al. 2022, MNRAS, 510, 2407
Bullock, J. S., & Johnston, K. V. 2005, ApJ, 635, 931
Cain, M., Frebel, A., Gull, M., et al. 2018, ApJ, 864, 43
Cain, M., Frebel, A., Ji, A. P., et al. 2020, ApJ, 898, 40
Carretta, E., Bragaglia, A., Gratton, R., D'Orazi, V., & Lucatello, S. 2009, A&A, 508, 695
Cayrel, R., Depagne, E., Spite, M., et al. 2004, A&A, 416, 1117
Cohen, J. G., Christlieb, N., Thompson, I., et al. 2013, ApJ, 778, 56
Conroy, C., Naidu, R. P., Garavito-Camargo, N., et al. 2021, Natur, 592, 534
Cowan, J. J., Sneden, C., Burles, S., et al. 2002, ApJ, 572, 861
Dempster, A. P., Laird, N. M., & Rubin, D. B. 1977, J. R. Stat. Soc. B, 39, 1
Erkal, D., Belokurov, V., Laporte, C. F. P., et al. 2019, MNRAS, 487, 2685
Erkal, D., Deason, A. J., Belokurov, V., et al. 2021, MNRAS, 506, 2677
Ezzeddine, R., Rasmussen, K., Frebel, A., et al. 2020, ApJ, 898, 150
François, P., Depagne, E., Hill, V., et al. 2007, A&A, 476, 935
Frebel, A., Christlieb, N., Norris, J. E., et al. 2007, ApJL, 660, L117
Gaia Collaboration, Brown, A. G. A., Vallenari, A., et al. 2018, A&A, 616, A1
Gaia Collaboration, Brown, A. G. A., Vallenari, A., et al. 2021, A&A, 649, A1
Gaia Collaboration, Prusti, T., de Bruijne, J. H. J., et al. 2016, A&A, 595, A1
Garavito-Camargo, N., Besla, G., Laporte, C. F. P., et al. 2019, ApJ, 884, 51
Gilmore, G., Randich, S., Asplund, M., et al. 2012, Msngr, 147, 25

Gómez, F. A., Helmi, A., Brown, A. G. A., & Li, Y.-S. 2010, MNRAS, 408, 935
Gudin, D., Shank, D., Beers, T. C., et al. 2021, ApJ, 908, 79
Hanke, M., Hansen, C. J., Ludwig, H.-G., et al. 2020, A&A, 635, A104
Hansen, C. J., Koch, A., Mashonkina, L., et al. 2020, A&A, 643, A49
Hansen, C. J., Primas, F., Hartman, H., et al. 2012, A&A, 545, A31
Hansen, T. T., Holmbeck, E. M., Beers, T. C., et al. 2018, ApJ, 858, 92
Hansen, T. T., Ji, A. P., Da Costa, G. S., et al. 2021, ApJ, 915, 103
Hattori, K., Erkal, D., & Sanders, J. L. 2016, MNRAS, 460, 497
Hattori, K., Valluri, M., & Vasiliev, E. 2021, MNRAS, 508, 5468
Hattori, K., & Yoshii, Y. 2011, MNRAS, 418, 2481
Hawkins, K., & Wyse, R. F. G. 2018, MNRAS, 481, 1028
Hayek, W., Wiesendahl, U., Christlieb, N., et al. 2009, A&A, 504, 511
Helmi, A., White, S. D. M., de Zeeuw, P. T., & Zhao, H. 1999, Natur, 402, 53
Hill, V., Christlieb, N., Beers, T. C., et al. 2017, A&A, 607, A91
Hill, V., Plez, B., Cayrel, R., et al. 2002, A&A, 387, 560
Hirai, Y., Beers, T. C., Chiba, M., et al. 2022, MNRAS, 517, 4856
Hollek, J. K., Frebel, A., Roederer, I. U., et al. 2011, ApJ, 742, 54
Holmbeck, E. M., Beers, T. C., Roederer, I. U., et al. 2018, ApJL, 859, L24
Holmbeck, E. M., Hansen, T. T., Beers, T. C., et al. 2020, ApJS, 249, 30
Honda, S., Aoki, W., Kajino, T., et al. 2004, ApJ, 607, 474
Horta, D., Schiavon, R. P., Mackereth, J. T., et al. 2020, MNRAS, 493, 3363
Hotokezaka, K., Piran, T., & Paul, M. 2015, NatPh, 11, 1042
Howes, L. M., Asplund, M., Keller, S. C., et al. 2016, MNRAS, 460, 884
Howes, L. M., Casey, A. R., Asplund, M., et al. 2015, Natur, 527, 484
Hunter, J. D. 2007, CSE, 9, 90
Ibata, R., Malhan, K., Martin, N., et al. 2021, ApJ, 914, 123
Ishigaki, M. N., Aoki, W., & Chiba, M. 2013, ApJ, 771, 67
Ishigaki, M. N., Chiba, M., & Aoki, W. 2012, ApJ, 753, 64
Ishigaki, M. N., Hwang, N., Chiba, M., & Aoki, W. 2016, ApJ, 823, 157
Ivans, I. I., Simmerer, J., Sneden, C., et al. 2006, ApJ, 645, 613
Jacobson, H. R., Keller, S., Frebel, A., et al. 2015, ApJ, 807, 171
Ji, A. P., Frebel, A., Chiti, A., & Simon, J. D. 2016, Natur, 531, 610
Ji, A. P., Li, T. S., Hansen, T. T., et al. 2020, AJ, 160, 181
Ji, A. P., Simon, J. D., Roederer, I. U., et al. 2022, arXiv:2207.03499
Johnson, C. I., McWilliam, A., & Rich, R. M. 2013, ApJL, 775, L27
Jones, E., Oliphant, T., Peterson, P., et al. 2001, SciPy: Open Source Scientific Tools for Python, http://www.scipy.org/
Kirby, E. N., Cohen, J. G., Guhathakurta, P., et al. 2013, ApJ, 779, 102
Kirby, E. N., Cohen, J. G., Smith, G. H., et al. 2011, ApJ, 727, 79
Koposov, S. E., Belokurov, V., Li, T. S., et al. 2019, MNRAS, 485, 4726
Koposov, S. E., Casey, A. R., Belokurov, V., et al. 2015, ApJ, 811, 62
Koppelman, H. H., Helmi, A., Massari, D., Price-Whelan, A. M., & Starkenburg, T. K. 2019, A&A, 631, L9
Lai, D. K., Bolte, M., Johnson, J. A., et al. 2008, ApJ, 681, 1524
Li, H., Aoki, W., Matsuno, T., et al. 2022a, ApJ, 931, 147
Li, H., Du, C., Liu, S., Donlon, T., & Newberg, H. J. 2019, ApJ, 874, 74
Li, T. S., Ji, A. P., Pace, A. B., et al. 2022b, ApJ, 928, 30
Lindegren, L., Bastian, U., Biermann, M., et al. 2021, A&A, 649, A4
Lövdal, S. S., Ruiz-Lara, T., Koppelman, H. H., et al. 2022, A&A, 665, A57
Malhan, K., Ibata, R. A., & Martin, N. F. 2018, MNRAS, 481, 3442
Malhan, K., Ibata, R. A., Sharma, S., et al. 2022, ApJ, 926, 107
Mardini, M. K., Placco, V. M., Meiron, Y., et al. 2020, ApJ, 903, 88
Marino, A. F., Milone, A. P., Karakas, A. I., et al. 2015, MNRAS, 450, 815
Martin, N. F., Ibata, R. A., Starkenburg, E., et al. 2022, arXiv:2201.01310
Mashonkina, L., Christlieb, N., Barklem, P. S., et al. 2010, A&A, 516, A46
Mashonkina, L., Christlieb, N., & Eriksson, K. 2014, A&A, 569, A43
Mateu, C. 2023, MNRAS, 520, 5225
Matsuno, T., Aoki, W., & Suda, T. 2019, ApJL, 874, L35
Matsuno, T., Hirai, Y., Tarumi, Y., et al. 2021, A&A, 650, A110
McMillan, P. J. 2017, MNRAS, 465, 76
Minor, Q. E., Pace, A. B., Marshall, J. L., & Strigari, L. E. 2019, MNRAS, 487, 2961
Myeong, G. C., Evans, N. W., Belokurov, V., Sanders, J. L., & Koposov, S. E. 2018, ApJL, 856, L26
Myeong, G. C., Vasiliev, E., Iorio, G., Evans, N. W., & Belokurov, V. 2019, MNRAS, 488, 1235
Naidu, R. P., Conroy, C., Bonaca, A., et al. 2022, arXiv:2204.09057
Navarrete, C., Chanamé, J., Ramírez, I., et al. 2015, ApJ, 808, 103
Neal, R. M., & Hinton, G. E. 1998, in Learning in Graphical Models, ed. M. I. Jordan (Berlin: Springer), 355
Okuno, A., & Hattori, K. 2022, arXiv:2204.08205
Petersen, M. S., & Peñarrubia, J. 2021, NatAs, 5, 251
Placco, V. M., Holmbeck, E. M., Frebel, A., et al. 2017, ApJ, 844, 18
Price-Whelan, A. M., Johnston, K. V., Valluri, M., et al. 2016, MNRAS, 455, 1079
Rasmussen, K. C., Zepeda, J., Beers, T. C., et al. 2020, ApJ, 905, 20
Reichert, M., Hansen, C. J., & Arcones, A. 2021, ApJ, 912, 157
Roederer, I. U., Cowan, J. J., Preston, G. W., et al. 2014a, MNRAS, 445, 2970
Roederer, I. U., Preston, G. W., Thompson, I. B., et al. 2014b, AJ, 147, 136
Roederer, I. U., Hattori, K., & Valluri, M. 2018a, AJ, 156, 179
Roederer, I. U., Sakari, C. M., Placco, V. M., et al. 2018b, ApJ, 865, 129
Roederer, I. U., Lawler, J. E., Den Hartog, E. A., et al. 2022, ApJS, 260, 27
Roederer, I. U., Mateo, M., Bailey, J. I. I., et al. 2016, AJ, 151, 82
Roederer, I. U., & Thompson, I. B. 2015, MNRAS, 449, 3889
Sakari, C. M., Placco, V. M., Farrell, E. M., et al. 2018a, ApJ, 868, 110
Sakari, C. M., Placco, V. M., Hansen, T., et al. 2018b, ApJL, 854, L20
Sakari, C. M., Roederer, I. U., Placco, V. M., et al. 2019, ApJ, 874, 148
Shank, D., Beers, T. C., Placco, V. M., et al. 2022, ApJ, 926, 26
Shipp, N., Drlica-Wagner, A., Balbinot, E., et al. 2018, ApJ, 862, 114
Shipp, N., Erkal, D., Drlica-Wagner, A., et al. 2021, ApJ, 923, 149
Sneden, C., Cowan, J. J., Lawler, J. E., et al. 2003, ApJ, 591, 936
Sneden, C., Kraft, R. P., Guhathakurta, P., Peterson, R. C., & Fulbright, J. P. 2004, AJ, 127, 2162
Sneden, C., Pilachowski, C. A., & Kraft, R. P. 2000, AJ, 120, 1351
Tolstoy, E., Hill, V., & Tosi, M. 2009, ARA&A, 47, 371
Tsujimoto, T., & Shigeyama, T. 2014a, A&A, 565, L5
Tsujimoto, T., & Shigeyama, T. 2014b, ApJL, 795, L18
Ueda, N., Nakano, R., Ghahramani, Z., & Hinton, G. E. 1998, in Advances in Neural Information Processing Systems, Vol. 11, ed. M. Kearns, S. Solla, & D. Cohn (Cambridge, MA: MIT Press)
Valentini, M., Chiappini, C., Bossini, D., et al. 2019, A&A, 627, A173
van der Walt, S., Colbert, S. C., & Varoquaux, G. 2011, CSE, 13, 22
Vargas, L. C., Geha, M., Kirby, E. N., & Simon, J. D. 2013, ApJ, 767, 134
Vasiliev, E. 2019, MNRAS, 482, 1525
Vasiliev, E., & Baumgardt, H. 2021, MNRAS, 505, 5978
Walker, M. G., Mateo, M., Olszewski, E. W., et al. 2015, ApJ, 808, 108
Wanajo, S., Hirai, Y., & Prantzos, N. 2021, MNRAS, 505, 5862
Westin, J., Sneden, C., Gustafsson, B., & Cowan, J. J. 2000, ApJ, 530, 783
White, S. D. M., & Rees, M. J. 1978, MNRAS, 183, 341
Wu, Y., Valluri, M., Panithanpaisal, N., et al. 2022, MNRAS, 509, 5882
Xing, Q.-F., Zhao, G., Aoki, W., et al. 2019, NatAs, 3, 631
Yuan, Z., Myeong, G. C., Beers, T. C., et al. 2020, ApJ, 891, 39
Zepeda, J., Rasmussen, K. C., Beers, T. C., et al. 2022, ApJ, 927, 13